Label Free Spectromicroscopy on Drug and Drug Loaded Nanocarriers in Skin

Inaugural-Dissertation
to obtain the academic degree
Doctor rerum naturalium (Dr. rer. nat.)

submitted to the Department of Biology,
Chemistry, Pharmacy
of Freie Universität Berlin

by

Kenji Yamamoto

2021

This doctoral thesis was carried out within the research group of Prof. Dr. Eckart Rühl from October 2013 until September 2021 at the Freie Universität Berlin, Department of Biology, Chemistry and Pharmacy. The work was supported by the Collaborate Research Center 1112 Nanocarriers: Architecture, Transport, and Topical Application of Drugs for Therapeutic Use.

1st Reviewer: Prof. Dr. Eckart Rühl _____

2nd Reviewer: Prof. Dr. Helmut Baumgärtel _____

Date of defense: 07.12.2021

Acknowledgements:

First, I like to express my gratitude to Prof. Dr. Eckart Rühl for giving me the opportunity to join his research group and to conduct my doctoral studies. I am very grateful for his excellent scientific guidance and his continuous support during my doctoral study. I highly value his outstanding expertise; he was willing to share.

I am very thankful to Prof. Dr. Helmut Baumgärtel who agreed on taking over the role as the 2nd Reviewer. I am very grateful for his willingness to share his exceptional experience and knowledge.

Special thanks I also like to express to Dr. André Klossek and Dr. Roman Flesch for all the support and mentorship during my doctoral studies. I am grateful for all the expertise they have shared with me.

I would like to thank all present and former members of the AG Rühl for creating an enjoyable working atmosphere. It was a pleasure being part of this scientific group. I like to mention Dr. Jonas Schenk, Dr. Piotr Patoka, Georg Ulrich, Valerie Mondes, Felix Gerke, Beate Kieling, Dr. Ina Halfpa, Dr. Janis Berkemeyer, Dr. Ruth Hirschberg, Marianne Muth, Öznur Delikaya and Anke Schindler. Thank you for all the interesting discussions we had, also apart from science.

I like to thank Marian Starke for his support during programming of the LabView software.

I am grateful to all who joined on beamtimes, during my doctoral thesis, at the UVSOR, BESSY, and the SLS electron storage ring facilities. Especially, I like to thank Prof. Dr. Nobuhiro Kosugi, Prof. Dr. Takuji Ohigashi, Dr. Fiorenza Rancan, Dr. Markus Weigand, and Michael Bechtel for all the enjoyable beamtimes, discussions, and dinners we had.

As part of the Collaborative Research Center 1112, I like to thank all former members. Special thanks I like to express to Hannah Pischon, Moritz Radbruch, Dr. Robert Schulz, Dr. Michael Unbehauen, and Dr. Karolina Walker. I very much enjoyed working with them as part of the CRC 1112.

I like to thank my family for supporting me during my doctoral studies. Especially, I like to thank my wife, Jasmin Yamamoto, for her continuous support during my doctoral thesis. Without her support I would have likely given up finishing this thesis. I like to thank her and my daughters Ayumi Zoe Yamamoto, Hitomi Lena Yamamoto, and Kazumi Hanna Yamamoto for encouraging me to go on even if that meant spending our free time for work.

I like to thank my mother Barbara Yamamoto-Lüneborg, her husband Bernhard Lüneborg, and my father Tsuneo Yamamoto as well as my parents-in-law Sabine and Rolf Greiser. Also, I like to express my thanks to my sister Mariko Yamamoto and my sister-in-law Katharina Greiser.

Table of Content

List of Publications

This cumulative thesis will give a brief overview on scientific work conducted on the topic "Label Free Spectromicroscopy on Drug and Drug Loaded Nanocarriers in Skin" on behalf of the Collaborative Research Center 1112. Detailed results have been published and are accessible as follows:

Yamamoto, K., Flesch, R., Ohigashi, T., Hedtrich, S., Klossek, A., Patoka, P., Ulrich, G., Ahlberg, S., Rancan, F., Vogt, A., Blume-Peytavi, U., Schrade, P., Bachmann, S., Schäfer-Korting, M., Kosugi, N. & Rühl, E. Selective Probing of the Penetration of Dexamethasone into Human Skin by Soft X-ray Spectromicroscopy. *Anal. Chem.* **87,** 6173–6179 (2015)

Yamamoto, K., Klossek, A., Flesch, R., Ohigashi, T., Fleige, E., Rancan, F., Frombach, J., Vogt, A., Blume-Peytavi, U., Schrade, P., Bachmann, S., Haag, R., Hedtrich, S., Schäfer-Korting, M., Kosugi, N. & Rühl, E. Core-multishell nanocarriers: Transport and release of dexamethasone probed by soft X-ray spectromicroscopy. *J. Controlled Release* **242,** 64–70 (2016)

Yamamoto, K., Klossek, A., Flesch, R., Rancan, F., Weigand, M., Bykova, I., Bechtel, M., Ahlberg, S., Vogt, A., Blume-Peytavi, U., Schrade, P., Bachmann, S., Hedtrich, S., Schäfer-Korting, M. & Rühl, E. Influence of the skin barrier on the penetration of topically-applied dexamethasone probed by soft X-ray spectromicroscopy. *Eur. J. Pharm. Biopharm.* **118,** 30–37 (2017)

Yamamoto, K., Klossek, A., Fuchs, K., Watts, B., Raabe, J., Flesch, R., Rancan, F., Pischon, H., Radbruch, M., Gruber, A. D., Mundhenk, L., Vogt, A., Blume-Peytavi, U., Schrade, P., Bachmann, S., Gurny, R. & Rühl, E. Soft X-ray microscopy for probing of topical tacrolimus delivery via micelles. *Eur. J. Pharm. Biopharm.* **139,** 68–75 (2019)

Results obtained during this thesis have also contributed to the following work:

Giulbudagian, M., Rancan, F., Klossek, A., Yamamoto, K., Jurisch, J., Neto, V. C., Schrade, P., Bachmann, S., Rühl, E., Blume-Peytavi, U., Vogt, A. & Calderón, M. Correlation between the chemical composition of thermoresponsive nanogels and their interaction with the skin barrier. *J. Controlled Release* **243,** 323–332 (2016)

Schulz, R., Yamamoto, K., Klossek, A., Flesch, R., Hönzke, S., Rancan, F., Vogt, A., Blume-Peytavi, U., Hedtrich, S., Schäfer-Korting, M., Rühl, E. & Netz, R. R. Data-based modeling of drug penetration relates human skin barrier function to the interplay of diffusivity and free-energy profiles. *Proc. Natl. Acad. Sci.* **114,** 3631–3636 (2017)

Wanjiku, B., Yamamoto, K., Klossek, A., Schumacher, F., Pischon, H., Mundhenk, L., Rancan, F., Judd, M. M., Ahmed, M., Zoschke, C., Kleuser, B., Rühl, E. & Schäfer-Korting, M. Qualifying X-ray and Stimulated Raman Spectromicroscopy for Mapping Cutaneous Drug Penetration. *Anal. Chem.* **91,** 7208–7214 (2019)

Schulz, R., Yamamoto, K., Klossek, A., Rancan, F., Vogt, A., Schütte, C., Rühl, E. & Netz, R. R. Modeling of Drug Diffusion Based on Concentration Profiles in Healthy and Damaged Human Skin. *Biophys. J.* **117,** 998–1008 (2019)

1. Introduction

People suffering from inflammatory skin diseases are increasing within the last decades among the population of the developed world.[1,2] Often underestimated, inflammatory skin diseases, like atopic dermatitis and psoriasis, lead not only to physiological but also to psychological burden.[3,4] Modern medicine developed potent drugs and therapies for the treatment of those diseases.[5,6] However, an efficient drug transport towards the site of action, going hand in hand with lowering the risk of adverse effects, still is challenging.

Topical treatment of inflammatory skin diseases can benefit from nanoscopic drug delivery systems in many ways. The penetration of weak penetrating drugs can be enhanced, drug release over time can benefit from drug reservoirs within the skin, and triggered drug release can be used to confine the drug exposed region to the site of action.[7,8] A variety of nanoscopic drug carriers have been developed for this purpose. Examples given are core multishell nanocarriers, micelles, microemulsions, nanogels, or nanocrystals.[9]

However, topical treatments by using nanocarriers can also have adverse effects. Cytotoxicity and genotoxicity may occur; especially for nanocarriers penetrating into viable parts of the skin.[10] Thus, toxicity tests but also the penetration characteristics of nanocarriers must be investigated.

The Collaborative Research Center 1112 – Nanocarriers "Architecture, Transport, and Topical Application of Drugs for Therapeutic Use" was formed to improve the scientific foundations for topical treatment of inflammatory skin diseases by the use of nanoscopic drug delivery systems. Thereby, different fields of research, namely chemistry, dermatology, pharmaceutical technology, pharmacology, physical chemistry, physics, and veterinary medicine were combined. This work, as a contribution from physical chemistry, is focused on label free spectromicroscopy on the penetration of drugs and nanocarriers in skin. The aim of this work is to deepen the understanding of nanocarriers and drug penetration characteristics in skin.

Nanocarrier penetration into human skin and the subsequent release of their cargo was already reported by fluorescence microscopy.[11,12] However, the influence of labels onto the nanocarrier penetration is not fully known yet. While the size of the fluorescent label compared to the nanocarrier size implies only small differences in skin penetration compared to unlabeled nanocarriers, it can be substantially different for labeled low molecular weight drugs. Thus, the use of label-free methods in spectromicroscopy could reveal new insights

into the penetration of drugs and nanocarriers in skin, X-ray microscopy and stimulated Raman microscopy fulfill those needs.[13,14] In addition to its chemical selectivity, X-ray microscopy benefits from its high spatial resolution.[15] Spatial resolutions down to 10 nm and even below were reported.[16,17] Also, X-ray microscopy has the advantage that the amount of drugs within the area of investigation can be calculated according to Beer's law. However, X-ray microscopy relies on a tunable X-ray source, such as a synchrotron radiation facility. Therefore, experimental time is limited. In contrast, stimulated Raman microscopy has the advantage of being available at any time once a stimulated Raman microscope has been set up. While lacking in spatial resolution, compared to X-ray microscopy, a stimulated Raman microscope is capable of scanning larger sample regions within a reasonable amount of time.

As part of this work a unique stimulated Raman microscope has been developed, which combines stimulated Raman microscopy with life science techniques. The reported setup utilizes stimulated Raman microscopy together with fluorescence microscopy, bright field microscopy, phase contrast microscopy and hyper-spectral imaging to increase the insights into the sample of interest.

Results of both label-free techniques are used and combined to analyze the penetration characteristics and the penetration mechanism of drugs and nanoscopic drug delivery systems.

2. Theoretical Background

The work covered in this thesis was conducted in collaboration with different fields of scientific research. Therefore, the theoretical background covers topics related to pharmacy, medicine, veterinary medicine, chemistry, physics, and physical chemistry. This Chapter will focus briefly on most important topics related to this work, namely skin, inflammatory skin diseases, drugs, nanocarriers, and label-free spectromicroscopy methods.

2.1 Human Skin

Skin is crucial for the survival of human beings. It prevents from uptake of pathogens, it regulates the body temperature, protects from unregulated water loss, and it shields the body from UV radiation.[18,19] The human skin is the largest sensory organ and it fulfills an important role within the human metabolism, the production of vitamin D.[20] However, there are various inflammatory skin diseases which can affect the functionality of the human skin e.g. atopic dermatitis or psoriasis. While modern medicine has found potent drugs for the topical treatment of inflammatory skin diseases, an efficient drug transport to the site of action still is challenging. Here, the protective function of the skin, hindering the drug penetration, is clearly a disadvantage. Therefore, high amounts of drugs for topical treatment or even systemic treatments are used causing significant adverse effects.[21] The intake of substances by the skin was never vital for human beings, in fact shielding from pathogens is. Therefore, the skin is equipped with multiple defense mechanisms against pathogens but also active defenses like immune cells.[22,23]

The human skin consists of multiple skin layers. One can distinguish between three main skin layers: the epidermis, the dermis, and the subcutis. The epidermis again can be separated into the stratum corneum, the stratum granulosum, the stratum spinosum, and the stratum basale, see Figure 2.1.1. In Figure 2.1.1 a skin cross section from optical microscopy of human skin is shown. Different skin layers and keratinocytes are indicated. In this Chapter, the function of the skin as a barrier will be discussed.

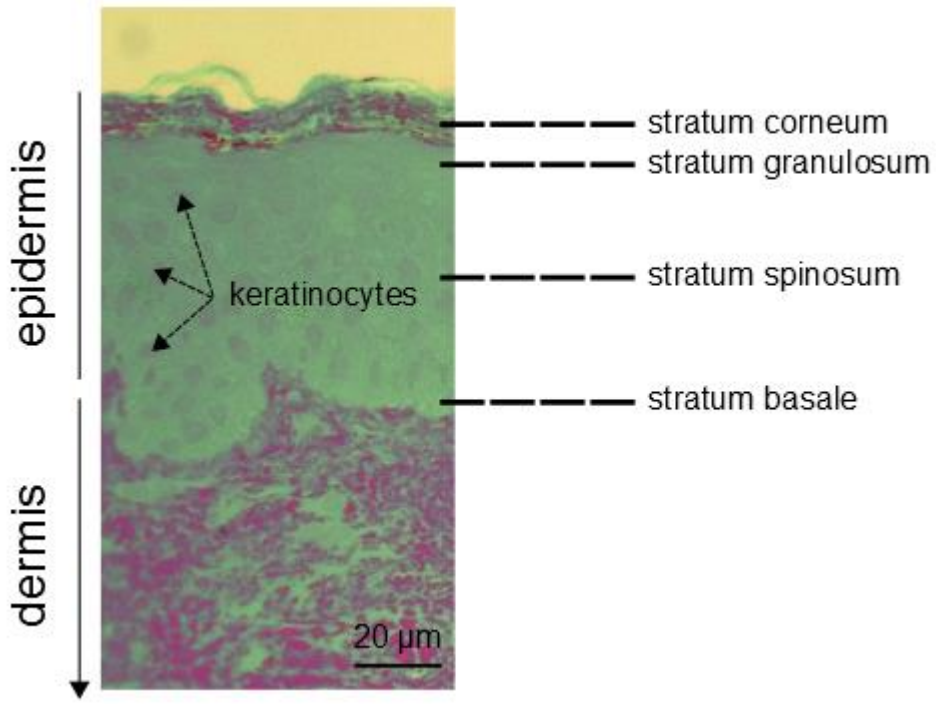

Fig. 2.1.1: Optical micrograph of human skin cross section. The dermis and the epidermis with its sub-layers, the stratum corneum, the stratum granulosum, the stratum spinosum, and the stratum basale are indicated. Examples for keratinocyte nuclei are highlighted by black arrows.

Within the following Section the term "viable epidermis" will be used for the viable part of the epidermis excluding the stratum corneum. Only when it is necessary the specific sub-layers will be pointed out.

Keratinocytes are the major constituent of the epidermis and can be found all over the epidermis in different conditions.[22] Keratinocytes, with their origin in epidermal stem cells at the basal layer, undergo a differentiation process during their proliferation to the stratum corneum, forming the individual layers of the epidermis. Metabolically active keratinocytes can be found within the stratum spinosum. During their differentiation process they synthesize different keratins, glutamine, and lysine-rich proteins which are stored within the inner surface of the cell's plasma membrane. During this process also lipids are subsequently released to the intercellular space of the stratum granulosum and the stratum corneum. When reaching the stratum granulosum keratinocytes stop producing keratin. Instead, they synthesize protein like filaggrin and enzymes which are involved in packing and cross linking of the keratin filaments. During this process also the metabolic activity of the keratinocytes drops down. Undergoing their last differentiation step keratinocytes will lose

their nuclei becoming corneocytes forming the stratum corneum together with the extracellular lipid matrix.[24] By continuous keratinocyte production and differentiation the epidermis is replacing itself in a 48 day cycle.[25] This is necessary since the epidermis forms the topmost layer of the skin, which is continuously removed by abrasion.

The stratum corneum, the topmost sub-layer of the epidermis, is usually explained by using a bricks and mortar model where the corneocytes are described by bricks and the lipid layer is visualized as mortar, see Figure 2.1.2.[26,27]

The stratum corneum is the main barrier of our skin and prevents the body from unwanted uptake of pathogens and water loss.[28,29] This is due to multiple layers of hydrophilic and lipophilic sections. In the bricks and mortar model the lipid matrix represents the lipophilic part of the stratum corneum with hydrophobic characteristics. Corneocytes, however, tend to be accessible by water. The average thickness of the human stratum corneum was calculated to 8.7 µm to 12.9 µm with an average cell layer number of 15.6 to 22.8 layers.[22] A single layer of the stratum corneum consists of $1.6 \cdot 10^6$ corneocytes/cm².[30]

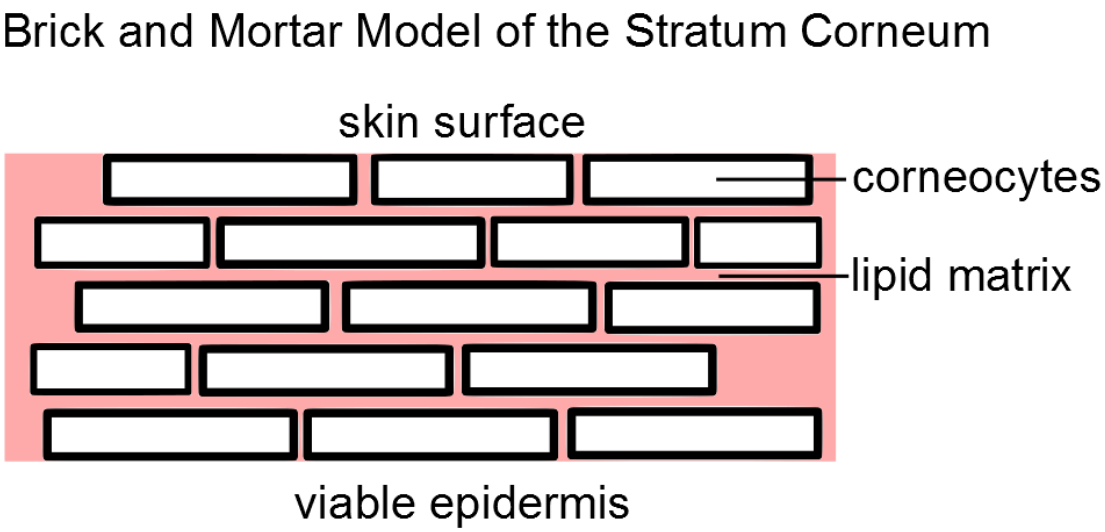

Fig. 2.1.2: Bricks and mortar model of the stratum corneum. Corneocytes (bricks) and the lipid matrix (mortar) are indicated.

The thickness of the viable epidermis strongly depends on the body site. The common thickness of the viable epidermis ranges often from 40 µm to 50 µm. However, on the wrists and back of the hands it increases to roughly 80 µm and further increases to around 400 µm for the front of the fingers.[22]

Compared to the viable epidermis the stratum corneum is relatively thin. Still the stratum corneum represents the skin's main barrier. This is of great disadvantage for the treatment of inflammatory skin diseases. Also, differences in water content can be observed for different skin layers and sub-layers. In general, the water content in skin is increasing with increasing depth slowing the penetration of hydrophobic drugs.[31] While smaller molecules can pass the stratum corneum, even if slowed down, the penetration efficiency decreases with increasing molecular weight. The upper limit for the molecular weight regarding effective skin penetration is well described by the 500 Dalton rule.[32] The 500 Dalton rule states that compounds with a molecular weight above 500 Da will not penetrate efficiently the physicochemical barrier of the skin. As a result, potent drugs such as tacrolimus, with a molecular weight of 822.046 Da, will not reach the site of action if topically applied to human skin. Alternative drug penetration routes, to overcome the stratum corneum, have been under detailed investigation; e.g. drug penetration through hair follicles.[33] Hair follicles reach into the dermis, pierce through the epidermis, and therefore, can be used as an alternative route to bypass the skin main barrier. However, also the hair follicles are act as a barrier. Still, penetration of high-molecular substances faces similar issues when comparing to topical treatment. However, hair follicles can act as a drug reservoir aiming on a slow but constant penetration over a longer period.

In addition to the stratum corneum also tight junctions, located in the stratum granulosum, are discussed to have barrier characteristics for topically applied drugs.[34,35] A barrier-like behavior at the epidermal-dermal border within the region of the basal layer is observed and will be discussed in this work.[36] The main components of the basal layer are the proteins of type IV collagen and laminin.[37]

Unlike the epidermis, the dermis is part of the transport system of the lymph and blood vessels. The lymph and blood vessels can be found all over the dermis and extent up to the basal membrane.[38] Also, nerves terminate within the dermis without reaching the epidermis. Therefore, drugs or nanocarriers reaching the dermis are systemically available by reaching the circulatory system of the organism. The dermis is made of collagen fibers and elastin embedded in mucopolysaccharide networks.[22] Hairs, except for terminal hairs, have their origin within the dermis as the sweat glands.

The subcutis is localized below the epidermis and is made of fat cells and collagen fibers. Here, differences between female and male skin can be observed.[39] The collagen fibers in female skin form a vertical structure, while in male skin additional diagonal cross-striation formations of collagen fibers can be observed.[40] The subcutis is also part of the lymph and

blood vessel systems, as the epidermis. The roots of terminal hairs, scalp, and pubic hairs are located within the subcutis.

Another important cell type found within skin's epidermis are Langerhans cells. Langerhans cells are part of the skin's defense against environmental pathogens and act as, among other defensive functions, antigen-presenting cells.[23] The skin immune defense is a very complex system. It reaches from keratinocytes as a sensor for danger (immune response by ligation of Toll-like receptors by pathogen-associated molecular patterns), Langerhans cells (antigen-presenting function), inflammatory dendric epidermal cells (respond to antibody-allergen complexes), dermal dendric cells (antigen presenting, cytokine and chemokine secretion), inflammatory dendric cells (TNF and nitric oxide production), macrophages (antimicrobial, production of pro- and anti-inflammatory mediators), to plasmacytoid dendric cells (IFNα production, involved in psoriasis and recognition of self-DNA-LL37 complexes).[41]

With its multilayered structure, skin is efficient in defending the human body against pathogens and mechanical impact, while also making the topical drug application challenging. Understanding each skin layer will help improving the topical treatment of inflammatory skin diseases by adapting drug formulations to the specific skin properties.

Murine Skin and Induced Inflammatory Skin Diseases

Animal testing has been subject of intense discussions.[42,43] Reducing the amount of animal testing is desired, especially if the 3R Principle (Replacement-Reduction-Refinement) is considered.[44–46] However, in some cases animal testing is necessary. While human skin, for research purpose, is available in limited amounts, inflamed human skin is even more difficult to receive for research from patients. Since drug penetration properties can be significantly different for inflamed and healthy human skin, tests also must be conducted on inflamed skin. Therefore, inflamed animal skin, with characteristics similar to that of human skin, is required for such research. Similarities between human and animal skin are found for rodents. In this work, two types of mice were used for animal testing, hairless SKH1 and BALB/c mice.[47] The histology for murine skin and human skin is similar, but not the same.[48] For example, the stratum corneum and the viable epidermis of healthy murine skin are significantly thinner than in human skin. However, a detailed discussion on differences between human and murine skin would exceed the scope of this Introduction. Therefore, if necessary, characteristic differences between human and murine skin will be pointed out further below, whenever this is needed. In general, the subdivision of murine skin into the

epidermis, dermis, and subcutis with all the sub layers, e.g. the stratum corneum, is similar to human skin.

Inflammatory skin diseases in mice were induced by different techniques either leading to a psoriasis like or an atopic dermatitis like skin disease. For psoriasis-like inflammatory skin disease BALB/c mice were used. Here, a TOLL-like receptor agonist which act as a immune response modifier, imiquimod (1-isobutyl-1H-imidazo[4,5-c]quinolin-4-amine, $C_{14}H_{16}N_4$) was used. Imiquimod binds to immune cells and induces an inflammation by activation of the immune cells.[49] Imiquimod cream was applied for 5 to 7 days on one flank of the mouse. This has the advantage to receive from one mouse both, intact and inflamed skin samples. BALB/c mice are not hairless. Therefore, two days prior to the imiquimod treatment, the mice were treated with Veet cream to remove the hairs.

Hairless SKH1 mice were used for experiments on atopic dermatitis-like inflammatory skin diseases. Note that SKH1 mice do have a working immune system which is necessary to induce an inflammation. The atopic dermatitis was induced by exposing the murine skin *in vivo* to allergens. Here, oxazolone was used as an allergen[50], which was applied topically onto the murine skin *in vivo*.[50] When applied for the first time, no inflammation will occur. However, antibodies countering oxazolone will be produced by the murine immune system. After a waiting period of 7 days oxazolone was applied onto the murine skin continuously, in a two-day cycle, until a constant intensity of inflammation was reached.

After psoriasis- or atopic dermatitis-like inflammation was induced, the mice were sacrificed, and the inflamed parts of the skin were extracted. Compared to human skin, the available skin areas are quite limited in size. While for excised human skin usually skin sections of 4 cm² were used for treatment of an area of 1 cm², the size of murine skin samples is usually below 0.5 cm². Topical treatment of the small skin areas was conducted carefully by avoiding any drug flow around the edges of the skin sections. In Figure 2.1.3 skin extracted murine skin sections are shown.

Fig. 2.1.3: Typical murine skin sections for topical treatment.

The size of the murine skin sections in Figure 2.1.3 clearly indicates the challenge when treating them with drug formulations.

2.2 Inflammatory Skin Diseases and Topical Treatment

Inflammatory skin diseases, often associated with allergies and asthma, are increasing within the last decades among the population of the developed world.[1,2] Two common inflammatory skin diseases, significantly decreasing the patient's quality of life, will be discussed within the further text, namely atopic dermatitis and psoriasis.[51–54]

Atopic Dermatitis

Atopic dermatitis is a chronic inflammatory skin disease where a cutaneous hyperreactivity can be triggered by environmental influences leading to its typical visual characteristics of red, cracked, and swollen skin.[55] The diseased part of the skin also results in an itchy skin, decreasing the patient's health-related quality of life significantly.[51] Atopic dermatitis leads to a dysfunction of the skin barrier affecting the transepidermal water loss and the intake of unwanted substances.[28,56,57] Therefore, the loss in barrier function is discussed to cause also asthma and allergies by the increased uptake of allergens.[57,58] The reason for the decreased barrier function, despite mechanical damage by itching, can be found in an altered lipid composition within the stratum corneum.[59]

The number of people affected by atopic dermatitis is increasing in the developed world.[60] However, the prevalence of atopic dermatitis is significant lower for agricultural areas.[55] While genetic predisposition seems to play a significant role in developing atopic dermatitis, it cannot explain the significant increase in atopic dermatitis diseased people within the

developed world.[2,61] Therefore, despite genetic predisposition, evidence increases that environmental influences have a significant impact on the development of atopic dermatitis. Food, aeroallergen, and decreased bacterial stimulation caused by increased hygienic standards and the use of antibiotics are discussed to be a reason.[55] An example for the genetic predisposition of developing atopic dermatitis is the loss of function by mutation of the filaggrin gene, which is responsible for the terminal differentiation of keratinocytes.[62] It should be mentioned that the reasons for developing atopic dermatitis are still under discussion.[63] Several studies have shown that the activation of multiple complex immunologic and inflammatory pathways can lead to this inflammatory skin disease.[55,64]

Typically atopic dermatitis presents during the childhood with a lifetime prevalence of 10% - 20% and can last into the adulthood by 1% - 3%.[55] In Figure 2.2.1 atopic dermatitis diseased skin of a 2-year-old child (female) is shown. Red colored lesions can be observed near the elbow.

Fig. 2.2.1: Atopic dermatitis diseased skin of a 2-year-old child (female).

One can distinguish between two types of atopic dermatitis, the allergic form (extrinsic) which affects 70% - 80% of all cases and the non-allergic form (intrinsic) affecting 20% - 30% of the diseased people.[65,66] The former type is caused by environmental allergens and is accompanied by an increased serum Immunoglobulin E level and an antibody playing an essential role in allergic diseases. For the latter form of atopic dermatitis, patients show no signs to allergen sensitization, which goes hand in hand with a low serum Immunoglobulin E level. Distinguishing between the two types of atopic dermatitis can be important regarding the treatment, e.g. for extrinsic atopic dermatitis it is important to avoid allergens.

The treatment of atopic dermatitis depends on the degree of inflammation. For dry skin only, skin care using hydration cream and emollients are usually suggested for treatment. For mild

to moderate atopic dermatitis, in addition, corticosteroids and calcineurin inhibitors in amounts according to the degree of the atopic dermatitis are topically applied. In case of severe atopic dermatitis systemic or UV therapy has to be considered. In all cases triggering factors of atopic dermatitis, such as allergens, should be identified and avoided.[5]

Psoriasis

Psoriasis is an inflammatory skin disease with a high prevalence worldwide (2-3%).[67,68] Psoriasis is mediated by T cells, dendritic cells, cytokines, and chemokines.[69] Similar to atopic dermatitis, psoriasis significantly decrease the quality of life of affected people.[53,54] A strong genetic predisposition can be observed for psoriasis as well as differences in the prevalence regarding climatic differences and environmental antigen exposure.[70,71] In contrast to atopic dermatitis an increase in allergies and asthma is not observed for psoriasis suffering patients. However, an increase of other diseases can be observed, e.g. arthritis, diabetes, colitis, and hypertension.[72]

Psoriasis is characterized by a thickened epidermis caused by hyperkeratosis, the increased differentiation and proliferation of keratinocytes.[69] Also, an increased growth of dermal blood vessels is observed leading to characteristic red lesions, shown in Figure 2.2.2. Corneocytes within psoriasis diseased skin are often not terminally differentiated and contain a cell nucleus.[73] In addition, the extracellular lipid matrix is not properly grown. Consequently, the stratum corneum fails to shield the human body efficiently from pathogens.

Fig. 2.2.2 Psoriasis diseased skin of a 37-year-old male. The characteristic red lesions are covered by white plaque.

In Figure 2.2.2 a typical example of psoriasis diseased skin is shown. The red lesions are covered by silvery-white scaly skin, called plaque.

Treatment of psoriasis depends on the degree of inflammation and on the disease's impact on the patient's life. The most common treatment of psoriasis is conducted by topically applying corticosteroid creams.[74] Also topical immunomodulators, such as tacrolimus as well as other biological agents like alefacept, efalizumab, and etanercept can be used for psoriasis treatment.[6] Tacrolimus can be used in creams, however, due to its mass of 822.05 Da penetration towards the site of action is challenging. The biological agents alefacept (51801.25 g/mol), efalizumab (51234.9 g/mol), and etanercept (51235.07 g/mol) have a atomic mass of roughly 50 kDa and therefore, topical treatment is not possible. In fact, those agents are subcutaneously injected.[75] Lately, biological therapies aiming at the tumor necrosis factor or T cells have become available.[73] Also, treatment by UVB radiation for severe psoriasis is conducted.[76]

2.3 Drugs and Nanoscopic Drug Delivery Systems

This Thesis reports on different drugs and nanoscopic drug delivery systems, investigated regarding their penetration behavior into intact human and intact and diseased murine skin. Thereby, different characteristics and penetration mechanism were observed. This Chapter introduces the investigated drugs and nanoscopic drug delivery systems. All nanoscopic drug delivery systems were provided by collaborators within the CRC 1112 except for the micellar nanocarriers. Micellar nanocarriers were provided by Apidel SA (Geneva, Switzerland).

Dexamethasone and Tacrolimus

A well-known and widely used corticosteroid with anti-inflammatory characteristics is dexamethasone. The use of dexamethasone covers a wide range of treatments including the treatment of inflamed skin, pulmonary inflammation and eye inflammation.[77–79]

The sum formula of dexamethasone is $C_{22}H_{29}FO_5$. The structure of dexamethasone is visualized in Figure 2.3.1. Dexamethasone has a molecular weight of 392.47 Da and is practically insoluble in water with a logP value of 1.83.[80] However, it is soluble in ethanol, methanol, acetone, dioxane, and chloroform.[81] Dexamethasone was purchased from Sigma Aldrich with a purity of > 98%.

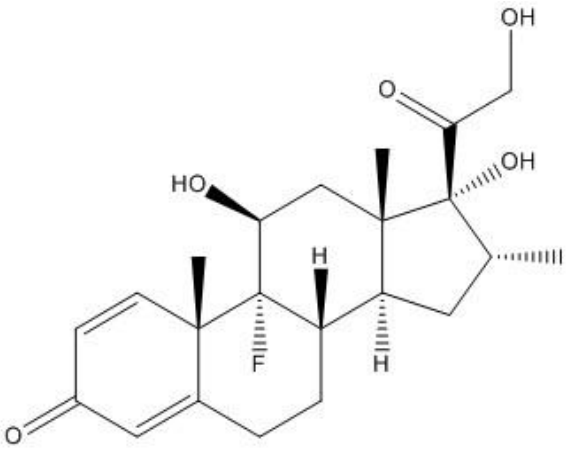

Fig. 2.3.1: Structure of dexamethasone.

Apart from dexamethasone, also the topical application of tacrolimus on skin was investigated. Tacrolimus is a macrolide lactone and is used as an immunosuppressant drug. Tacrolimus can be used to treat atopic dermatitis, but it is also used for organ transplantation.[82–84] The sum formula of tacrolimus is $C_{44}H_{69}NO_{12}$. Its structure is visualized in Figure 2.3.2. Tacrolimus has a molecular weight of 822.046 Da and is insoluble in water with a logP value of 3.3.[85] However, tacrolimus is soluble in methanol, ethanol, acetone, ethyl acetate, chloroform, and diethyl ether.[86] Tacrolimus was purchased from LC Labs with a purity of > 99%.

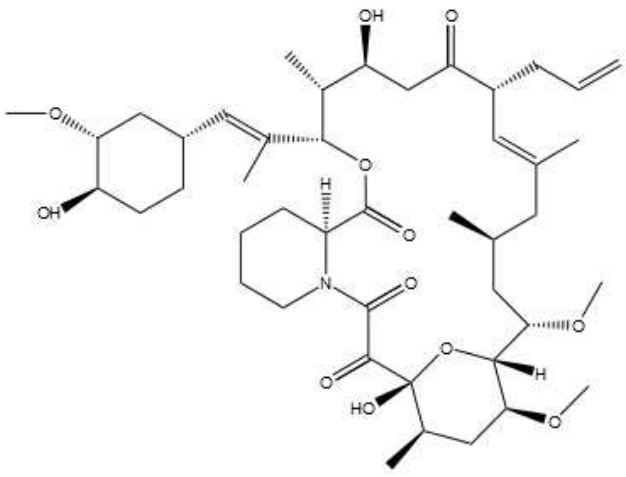

Fig. 2.3.2: Structure of tacrolimus.

The structures of the drugs were visualized by ChemDraw Professional.[87]

Nanoscopic Drug Delivery Systems – Core Multishell Nanocarriers, Micellar Nanocarriers, and Thermoresponsive Nanogel

Apart from standard drug formulation, such as cremes, improved formulations utilizing nanoscopic drug delivery systems were investigated. Also, to compare the penetration characteristics of the neat drug, drug dissolved in ethanol was used to achieve detectable concentrations of drugs. In this work the use of core multishell nanocarriers, micellar nanocarriers, and thermoresponsive nanogel is reported. For thermoresponsive nanogels, apart from the neat penetration characteristics, also triggering of the drug release and its impact on the drug penetration is investigated. For subsequent work also nanocarriers utilizing other triggering mechanism might be of interest such as nanocarriers sensitive to PH, redox gradient, enzyme concentration, ultrasound, magnetic field, light, and electric pulses.[88]

Core multishell nanocarriers, for skin penetration experiments, were provided by collaboration partners from Freie Universität Berlin (AG Haag).[89] The nanocarriers were made of three building blocks, the core, the inner shell, and the outer shell. A schematic description of the core multishell nanocarriers is shown in Figure 2.3.3. Thereby each building block has different characteristics. The core multishell nanocarriers are made of a polar core, a nonpolar inner shell, and a hydrophilic outer shell. Thus, nanocarriers can transport hydrophilic as well as hydrophobic agents. Transport of the encapsulated drugs is conducted by penetration of the nanocarriers into the skin.

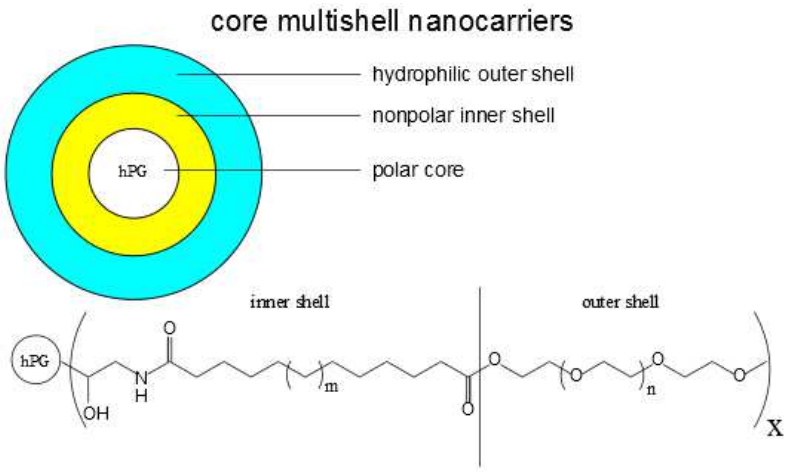

Fig. 2.3.3: Schematics of core multishell nanocarriers. All three building blocks, the core, the inner shell, and the outer shell are indicated. The structure of the inner and outer shells is included in the bottom part.

The core of the core multishell nanocarriers is made of hyperbranched polyglycerol (hPG) with 10 kDa in molecular weight. The inner and outer shell of the core multishell nanocarriers are made by linking Methoxy poly(ethyleneglycol) with a molecular weight of 350 g/mol (mPEG350) to the polyglycerol core. The mPEG350 was purchased from Acros Organics (Geel, Belgium). All other chemicals were purchased from Sigma Aldrich (Taufkirchen, Germany). The nanocarriers had a size of around 10 nm and a molecular mass ranging from 60 kDa to 80 kDa. The synthesis of the core-multishell nanocarriers has been reported in detail before.[12,90,91] Loading of the core-multishell nanocarriers was conducted by dissolving 11.3 mg core-multishell nanocarriers with 2.0 mg dexamethasone in 200 µL ethanol within a screw cap vial. Subsequently, the ethanol was removed by a rotary evaporator and drying overnight within a drying oven at 60 °C.[89] Thus, a drug load of approximately 5% was achieved.[89,92]

Micellar nanocarriers were provided by Apidel SA (Geneva, Switzerland) for topical delivery of tacrolimus, called ApidSOL™. ApidSOL™ is based on methoxy poly-ethylene glycol (mPEG) and Poly(caprylic acid) co-polymers. The drug concentration within the ApidSOL™ formulation is around 0.7%. An enhanced topical delivery of tacrolimus compared to Protopic, the standard formulation of tacrolimus in petroleum jelly, has been reported before.[93]

Furthermore, the use of thermoresponsive nanogels as a drug delivery system was investigated. Thermoresponsive nanogels can be characterized as a supramolecular network of cross linked polymeric units which can change their network structure when triggered inducing heat.[94] Thermoresponsive nanogels were provided by collaborators from Freie Universität Berlin (AG Calderon). Nanogels are highly capable in the uptake of water; reaching up to 90% of their weight. The penetration mechanism, however, is different than compared to core multishell nanocarriers for example. Thermoresponsive nanogels are assumed to hydrate the stratum corneum of the skin, making it more permeable to topically applied formulations, as reported previously.[95,96] Here, poly(N-isopropylacrylamide), pNIPAM, and di(ethylene glycol) methyl ether methacrylate - co - oligo ethylene glycol methacrylate (DEGMA-co-OEGMA475), OEG, nanogels were used for skin penetration experiments. The synthesis of the used thermoresponsive nanogels by the AG Calderon has been reported in literature.[97] The size of the thermoresponsive nanogels ranged from $(95 \pm 2)\ nm$ (pNIPAM) to $(112 \pm 2)\ nm$ (OEG). Triggering of the thermoresponsive nanogels is induced by IR radiation (Philips Infrared RI 1521, 30 s, 116.8 mW, 3.9 mJ/cm²).[97] Thereby, the nanogel shrinks and the encapsulated drug is released. For triggering of the

thermoresponsive nanogel it is important that the IR radiation induced temperature of the thermoresponse nanogel exceed the cloud point (T_{CP}). The cloud temperature for the pNIPAM nanogels used for this work was determined to be 34 °C.

2.4 Label Free Spectromicroscopy

The aim of this work is to determine penetration characteristics of drugs and nanocarriers in skin. Thus, when analyzing fixed skin sections *ex vivo* two types of information are needed: The spatial information on the structure under analysis and the amount of the species of interest, e.g. the drug, within the volume under investigation. Spectromicroscopy combines both pieces of information.

Two different methods for label-free spectromicroscopy were utilized within this work, X-ray microscopy and Stimulated Raman microscopy. Both setups and experimental methods are described in this Chapter.

Scanning Transmission X-Ray Microscopy

Scanning Transmission X-Ray microscopy was conducted at the UVSOR III facility (Ultra Violet Synchrotron Orbital Radiation) of the Institute of Molecular Science in Okazaki, Japan, at the BESSY II facility (Berliner Elektronenspeicherring-Gesellschaft für Synchrotronstrahlung) of the Helmholtz Zentrum in Berlin, Germany, and at the SLS (Swiss Light Source) of the Paul Scherrer Institute in Villigen, Switzerland.

Thereby, X-rays of a selected photon energy were focused by a Fresnel zone plate onto the sample under investigation; subsequently the transmitted photons were measured by using a photon detector (diode or photomultiplier). In this work the use of photon energies between 520 eV to 570 eV is reported. By moving the sample in x-y direction an area of interest was scanned. The chemical contrast between skin and species of interest is achieved by making use of a modifying the Beer-Lambert law.

The Beer-Lambert law is shown in equation E2.4.1.

$$ln\left(\frac{I}{I_0}\right) = \sigma \cdot N \cdot d \qquad \text{(E2.4.1)}$$

According to the Beer-Lambert law I is the transmitted light through the sample, I_0 is the initial intensity of the incident radiation, σ is the absorption cross section of the species under investigation, N is the density of particles within the investigated volume, and d is the thickness of the sample.

The Beer-Lambert law describes the attenuation of incident radiation by matter. Thereby, the attenuation strength depends on the thickness of the sample, the particle concentration, and the absorption cross sections of the contained species. However, the Beer-Lambert law requires that the absorption only occurs due to the species of interest. Strong background absorption will lead to false values. Therefore, the Beer-Lambert law cannot be used to describe the attenuation of the incident radiation by a specific molecule of interest within a sample containing other absorbing species. To separate the absorption of different species some changes are necessary.

The Beer-Lambert equation E2.4.1 is modified to:

$$ln\left(\frac{I_{E2}}{I_{E1}}\right) = \sigma \cdot N \cdot d \qquad \text{(E2.4.2)}$$

; where I_{E2} is the transmission at a photon energy for which the absorption cross section of the species of interest differs from the absorption of the background, while I_{E1} describes a photon energy at which the absorption cross sections between the species of interest and the background are similar to each other.

From Equation E2.4.2 follows that the transmission of the sample must be determined for two photon energies in the described manner to determine the amount of the species of interest within the sample material. The photon energies were carefully selected by making use of X-ray absorption spectra.

Inner Shell Electron Excitation

In this work X-ray spectroscopic and X-ray spectro-microscopic techniques are used for label-free detection of drugs and nanocarrier in skin. The chemical contrast between the species of interest and the surrounding, mostly skin, is obtained from the unique absorption characteristics of soft X-rays by the sample.

X-ray absorption-based results reported in this work rely on the inner shell electron excitation of oxygen and carbon by soft X-rays. Thereby, the absorption cross section σ has a characteristic energy-dependent value. It defines the amount of electrons excited into a bound or continuum state for an atom or molecule per unit area, divided by the amount of incident photons.[98] X-Ray absorption cross sections for Z = 1 to 94 atoms for photon energies $E = 100\ eV\ to\ 2000\ eV$ were reported by Henke.[99] The absorption cross section has the dimension of an area and is typically given in barn or cm². Thus, the absorption cross section can be treated as the effective area on which a photon is absorbed. The absorption cross

section σ can be calculated according to Fermi's Golden Rule for the transition probability P_{if} of an electron within the initial state $|i>$ to the final state $|f>$ and the photon flux F_{ph}:

$$\sigma = \frac{P_{if}}{F_{ph}} \tag{E2.4.3}$$

; where P_{if} is the transition probability of an electron within the initial state and F_{ph} is the photon flux. The transition probability P_{if} is given by:

$$P_{if} = \frac{2\pi}{\hbar} |< f|V|i >|^2 \rho(E_f) \tag{E2.4.4}$$

; here $|< f|V|i >|$ is the matrix element of the perturbation operator V, $\hbar$ is the reduced Planck constant, and $\rho(E_f)$ is the energy density of the final state.[98]

The photon flux F_{ph} is given by:

$$F_{ph} = \frac{E_0^2 c}{8\pi\hbar\omega} \tag{E2.4.5}$$

; with E_0 the electric field, c the speed of light, $\hbar$ the reduced Planck constant, and ω the frequency.

When discussing electron transition to bound states and intensities of resonances, often the optical oscillator strength f is used, which is related to the cross section as follows:[98]

$$\sigma(E) = C\frac{df}{dE} \tag{E2.4.6}$$

; where $C = 2\pi^2\hbar/mc$.

For this work electron transitions of 1s electrons into bound states are of importance. Resonant transitions can be determined from the molecular orbital concept.[98] Within this work, X-ray absorption spectro-microsocpy is conducted on low-Z elements only, such as oxygen or carbon. The initial state is of σ symmetry, the final state is of σ or π symmetry, depending on the involved p-orbital component. Thus, the contrast within the observed X-ray spectromicroscopy images relies on differences in $1s \rightarrow \pi^*$ and $1s \rightarrow \sigma^*$ transitions. The transition energy and the available molecular orbitals depend on the electronic structure of the molecule under investigation. Possible transitions into unoccupied states can be visualized by Molecular Orbital Theory. Molecular orbitals can be described by linear combination of atomic orbitals and can be described by addition and subtraction of atomic orbitals, called linear combination of atomic orbitals.[100,101] The addition and subtraction of atomic orbital wave functions, of two atoms (a) and (b), result in bonding molecular orbitals.

$$\psi_{MO} = \psi_a \pm \psi_b \tag{E2.4.7}$$

; where ψ_{MO} is the wave function of the molecular orbital, while ψ_a and ψ_b are the wave function of the atomic orbitals, respectively.

Available molecular orbitals also depend on the bond type between the involved atoms. Atoms bind via σ bonds result in σ bonding and anti-bonding molecular orbitals. An example for molecular O_2 is shown in Figure 2.4.1.

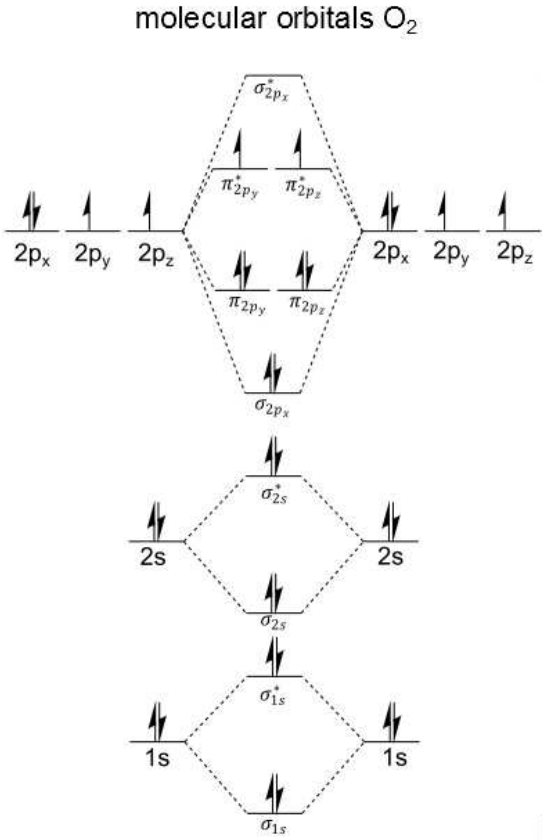

Fig. 2.4.1: Molecular orbitals for O_2 are shown. The bonding and anti-bonding σ and π molecular orbitals and the atomic orbitals are indicated.

In Figure 2.4.1 the $2P_y$ and the $2P_z$ atomic orbitals of both oxygen atoms contribute to the π bonding and anti-bonding molecular orbitals. The 1s, the 2s, and the $2P_x$ atomic orbitals contribute to the σ bonding and anti-bonding molecular orbitals. Taking O_2 as an example, $1s \rightarrow \pi^*$ and $1s \rightarrow \sigma^*$ transitions are possible, which will result in X-ray absorption features for both transition within the oxygen 1s absorption spectrum. The transition energy thereby depends on the probed bond, the atoms involved, and on the chemical surrounding, which will influence the energy of molecular orbitals. This can be well interpreted by the molecular orbital theory.[102] The impact on the transition energies of the molecular orbitals can be observed by X-ray absorption spectroscopy.[103] Thus, it is possible to distinguish different

chemical species according to the energy position of the $1s \rightarrow \pi^*$ and $1s \rightarrow \sigma^*$ transitions. Example given, for this work, the selective excitation of dexamethasone in skin was conducted at one of its two carbonyl groups. The resonant structure, between 529 eV and 533 eV, within the oxygen 1s spectra can be reasoned by the two carbonyl groups at C3 and C20 site.[104,105] In this work the energetic lower resonance, centered at 531 eV, was used for selective excitation of dexamethasone, which could be related to the C3 site, the quinoic carbonyl. The higher portion of the resonance observed within the dexamethasone oxygen 1s spectra, between 529 eV and 532 eV, is related to the C20 site. Thus, a chemical shift between both carbonyl groups could be observed, similar to when comparing the resonant structures at the oxygen 1s spectra of p-benzoquinone and acetone.[104,106] In Figure 2.4.2 the oxygen 1s spectra of dexamethasone and skin is shown. One can clearly distinguish between skin and dexamethasone at its $1s \rightarrow \pi^*$ resonances. Next to the oxygen 1s spectra the skeletal structure of dexamethasone with its two carbonyl sites indicated is shown. Within the oxygen 1s spectra energies used for selective excitation of dexamethasone in skin are indicated.

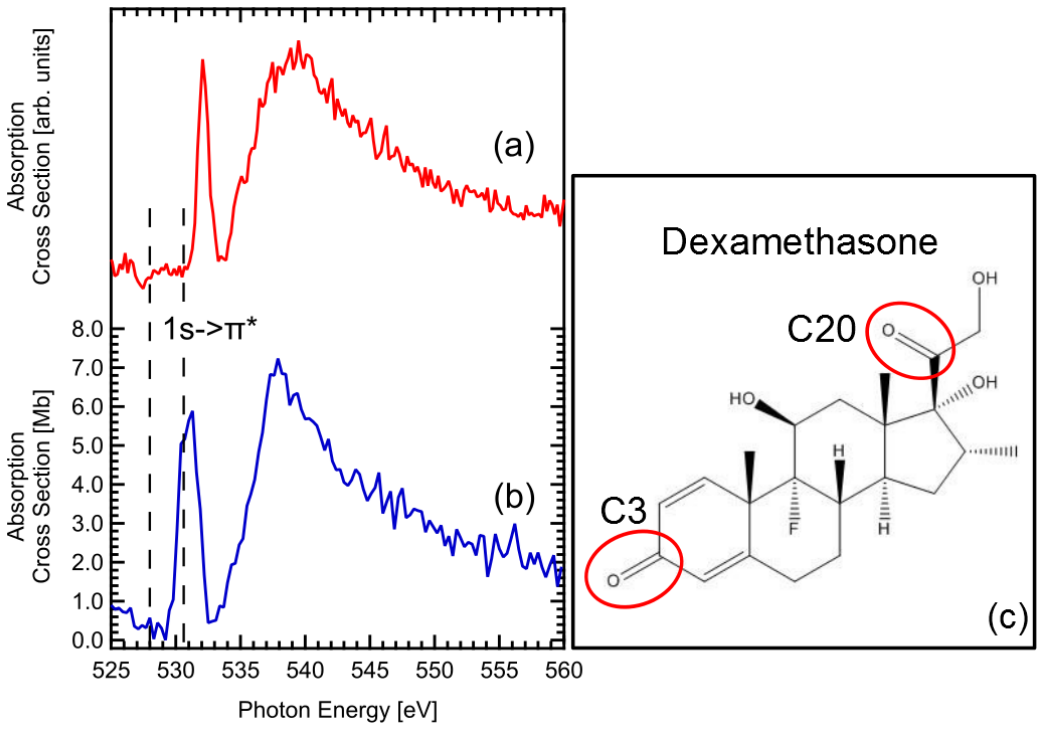

Fig. 2.4.2: (a) Oxygen $1s$ absorption spectra of human skin and (b) dexamethasone. Excitation energies, used for X-ray spectromicroscopy, at the pre-edge (528.0 eV) and at the $O\ 1s \rightarrow \pi^*$ transition of dexamethasone (530.6 eV), are indicated by dashed lines. In (c) the skeletal structure of dexamethasone is shown. Oxygen atoms contributing to the $O\ 1s \rightarrow \pi^*$ transition are indicated at the C3 and C20 site.

Experimental Setups for Scanning Transmission X-Ray Microscopy

The scanning transmission X-ray microscope at the UVSOR III facility is located at the BL4U undulator beamline. A combination of an in-vacuum undulator together with a variable-included-angle Monk-Gillieson mounting monochromator was used for dispersing synchrotron radiation.[107] The monochromator was equipped with a varied-line-spacing plane grating. The effective energy range reaches from 75 eV to 1000 eV. The transmitted photons were detected by using a photomultiplier tube and a phosphor screen (Hamamatsu R647P with a P43 scintillator). The energy resolution $E/\Delta E$ is 3000 at an exit slit size of 50 µm. The measurements were conducted inside a vacuum recipient that was back-filled by 50 hPa helium. The recipient was separated from the ultrahigh vacuum of the beamline by a silicon nitride window.

The scanning transmission X-ray microscope setup "Magnetic X-ray Microscope with UHV Spectroscopy" (MAXYMUS) at the BESSY II facility is located at the UE46-PGM-2 undulator beamline. At MAXYMUS an apple type undulator together with a collimated plane grating (0.7° reflection angle) high flux monochromator, equipped either with a 600 l/mm or a high resolution 1200 l/mm grating was used to disperse the photon energy. The covered energy range of this instrument reached from 150 eV to 1900 eV. The transmitted photons were detected using a photomultiplier tube and a phosphor screen (Hamamatsu C9744 with a P43 scintillator). The energy resolution $E/\Delta E$ is 4000 at an exit slit size of 20 µm. The experimental chamber was used under high vacuum conditions $10^{-4}\ mbar$ in the single bunch mode.

At the Swiss Light Source the scanning transmission X-ray microscope at the PolLux bending magnet beamline was used.[108] Two spherical gratings with 300 l/mm and 600 l/mm were used to access a photon energy range from 270 eV to 1600 eV. The transmitted photons were detected by using a photomultiplier tube and a phosphor screen (Hamamatsu 647P together with a P43 scintillator). The energy resolution $E/\Delta E$ is 5000 at 400 eV photon energy when using an exit slit width of 10 µm. The measurements were conducted under high vacuum ($10^{-3}\ mbar$).

All three scanning transmission X-ray microscopes that were used in this work were built by Bruker Advanced Supercon GmbH (Bruker ASC). The design of the X-Ray microscopes was developed by North Carolina State University, the Advanced Light Source, and McMaster University.[109] A schematic description of the setups is shown in Figure 2.4.3. The

beam path and crucial components for X-ray microscopy are highlighted. Firstly, the radiation at a selected photon energy hits the zone plate. The zone plate is crucial, since it focuses the photons onto the sample by diffraction and determines the spatial resolution of the X-ray microscope. The central beam stop suppresses zero order light, reducing the signal-to-background ratio. An order sorting aperture is placed between the zone plate and the sample at roughly 0.75 times the focal distance. If aligned properly, the order sorting aperture only allows the positive first diffraction order to pass. Thus, radiation from unwanted diffraction orders is avoided leading again to a decreased background-to-noise ratio. Subsequently, after hitting the sample, the transmitted radiation is detected by the photodetector.

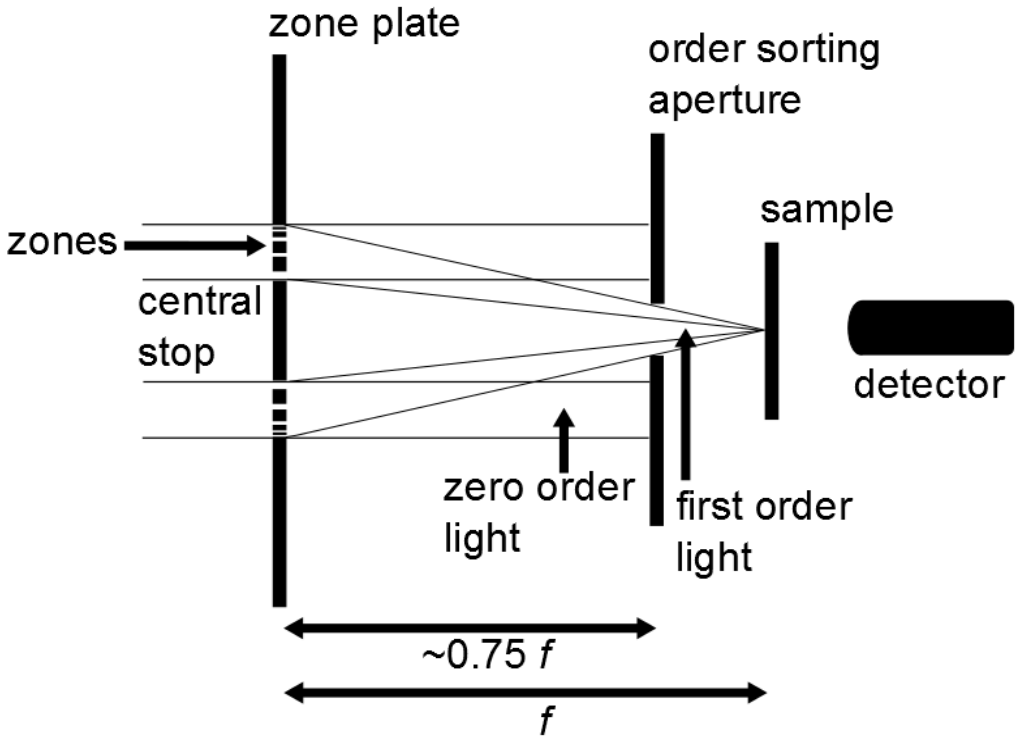

Fig. 2.4.3: Schematic drawing of the scanning X-ray microscopy setup including the zone plate, the order sorting aperture, the detector, and the sample. The focal length is indicated by *f*.

An implemented differential interferometer control allows for precise determination of the sample position with respect to the zone plate. Together with a closed-loop piezoelectric stage x,y imaging with a precision of 2 nm root mean square is possible. Due to the closed-loop piezoelectric stage also drifts and vibrations are reduced by real-time communication between the interferometers and the piezoelectric stage. The piezoelectric stage was used for

fine and reproducible x,y imaging. However, for overview scans and sample positioning stepping motors were used. The stepping motors also come into play for approaching quickly specific regions of interest.

All three X-ray microscopy setups used a combination of a P43 ($Gd_2O_2S:Tb$) phosphor screens (scintillator) and photo-multiplier tubes to detect the transmitted X-rays. The scintillator converts the soft X-rays to visible light by photo luminescence which is subsequently detected by the photo-multiplier tube. P43 was chosen for the scintillator material due to its high efficiency when using photon energies in the regime of 150 eV to 2000 eV and because of its stability during prolonged X-ray exposure.[110] However, when using a P43 phosphor the dwell time for a single measuring point must be at least 1 ms or longer due to the long scintillator decay time of the P43 phosphor, which is around 1 ms.[111] This was of no concern for this experimental work. The dwell times used ranged typically from 1 ms to 2 ms.

Experimental Requirements

All reported measurements were conducted either at the oxygen 1s or carbon 1s absorption of around 533 eV and 286 eV, respectively. However, also photon energies for the investigation of the 1s-edges of other light elements, such as nitrogen, and fluorine were accessible at all three beamlines.[112]

The excitation energies were carefully selected also considering the available energy resolution. The energy resolution within the region of interest ranged typically between 0.1 eV and 0.2 eV. The spatial resolution was adapted to the structures under investigation. In this work X-ray microscopy measurements using a pixel size from 1 µm down to 50 nm are reported. Structures under investigation usually had a size of 100 nm to some µm. No significant drawbacks or advantages were observed when measuring under high vacuum or He backfilled (50 mbar) conditions, respectively. However, overheating of the X-ray microscope stepper motors must be considered when using the setup under high vacuum condition.

The photon flux had to be carefully adjusted to the sample to avoid any sample damage. An important fact, which has to be considered is that organic materials, such as cells or tissue suffer in general from ionizing radiation.[113,114] Therefore, the operating mode of the electron storage ring was of high importance for the MAXYMUS and PolLux setup. For both setups, the amount of photons per area and time, namely the brilliance ($\frac{photons}{s \cdot mrad^2 \cdot mm^2 \cdot 0.1\%\ bandwith}$), was too high causing severe sample damage, especially in multi bunch mode. Single bunch

mode was mandatory. The operation modes, multi bunch and single bunch, describe the electron bucket population within the ring during operation. A higher electron population will yield into a higher number of emitted photons and therefore, into a higher brilliance. At the UVISOR III facility this issue was of no concern since the brilliance matched the experimental needs also in multi bunch mode and top-up operation of the storage ring.

For X-ray spectro-microscopic measurements the degradation of biologicals samples was an issue. Therefore, samples were dehydrated and fixed into EPON resin.

The time consumed by image and energy scans was similar for all three setups. A typical X-ray microscopy image with a spatial dimension of 25 µm times 100 µm at a resolution of 100 nm with 1 ms dwell time took around 15 min for one photon energy. An oxygen 1s absorption spectrum, from 520 eV to 570 eV, typically took around 20 min.

Transmission Spectra

For X-ray spectromicroscopy experiments described in this work excitation energies which can be used to distinguish between the species of interest (drug, nanocarrier) and the background, such as skin, are needed, see Equation E2.4.2. Therefore, taking transmission spectra of the samples within the energy range of interest, was always the first step of the experiments.

The transmission spectra of the neat drug, nanocarriers, or drug loaded nanocarriers were taken after applying the sample of interest on a silicon nitride membrane.

For skin, transmission spectra were always taken from regions that have a similar structure compared to the regions of the subsequent spectromicroscopy measurements.

Furthermore, in order to obtain an absorption spectrum of the species of interest, absorption from contaminations within the photon beam path must be considered. For the reported measurements of oxygen containing also contaminations on top of the mirrors, the grating, and on the surface of the Si_3N_4 windows were of relevance. Therefore, additional transmission spectra of the background photon flux were measured. The transmission I of the sample under investigation is corrected by the transmission I_0 of the transmitted rays without the sample, yielding the absorbance A of the investigated sample, according to:

$$A = -ln\left(\frac{I}{I_0}\right) \tag{E2.4.8}$$

From data on the chemical composition of the sample and its atomic absorption cross section the absorbance of the species under investigation can be quantified.[99]

To avoid sample damage the spot size of the X-ray beam, for absorption spectra, was always defocused to 1 µm or more.

Scanning X-Ray Micrographs

The amount of penetrated drug and nanocarriers in the skin samples is determined by site selective X-ray microscopy. Scanning X-ray micrographs link the chemical information to the morphology of the skin under investigation. All scanning X-ray micrographs were measured in the transmission mode. Thereby, X-rays are focused onto the sample and the transmitted photon flux is measured by the detector. The intensity of the transmitted radiation depends on the absorption characteristics of the sample under investigation. Moreover, the absorption depends on each atom within the molecule influenced by its chemical surrounding. Site selective excitation of the species of interest was conducted by adapting the excitation energy according to observed resonances within the absorption spectra. For example, to detect dexamethasone in skin we made use of the $O\ 1s \rightarrow \pi^*$ transition of the oxygen bound at the carbonyl site (C3).[13]

Scanning X-ray micrographs are measured by mapping the sample when moving the x, y stage according to the investigated region. Two different scanning modes, “point by point” and “line at once”, were available. Using the “point by point” mode the x, y stage is moving from a specific point to the next measurement point. Thereby, measuring the transmitted photons for a pre-defined dwell time after arrival at the selected point. When using the “line at once” mode the image is taken line by line without stopping of the x, y stage at each measurement point. The dwell time for each measurement point is adjusted by the scanning velocity of the x, y stage. Usually, the “line at once” mode was used since it is less time consuming than the “point by point” mode. Furthermore, the acceleration phase (positive and negative) for each measuring point is avoided.

The detection limit of the drug under investigation depends on its photon energy dependent absorption cross section. The chemical contrast is achieved by differences within the absorption cross section, between drug and skin, when exciting the sample at different photon energies, as described in Equation E2.4.2. As an example, for a measuring point with a spatial extent of $1\ \mu m^2 \cdot 300nm$ the detection limit for dexamethasone is within the sub fg regime. This is estimated from the absolute drug concentration using X-ray microscopy in the O 1s-regime. From this, it follows that a topically applied concentration of dexamethasone of $0.2\ \mu \frac{g}{cm^2} \cdot \mu m$ can be detected in the skin. This corresponds roughly to one million dexamethasone molecules within a volume of 0.3 µm³ skin tissue, which again

corresponds to approximately < 0.16% of the volume under investigation. For this estimation, a molar mass of 392.47 g/mol and a molar volume of $(296 \pm 5) cm^3$ were assumed for dexamethasone. The latter value was predicted using the ACD/Labs Percepta Platform – PhysChem Module.[115] This detection limit is valid for all three scanning X-ray microscopic setups, which is due to their similar design and characteristics.

Stimulated Raman Microscopy

Raman microscopy was introduced as a powerful approach, combining optical microscopy with Raman spectroscopy. The setup of a Raman microscope usually includes an optical microscope combined with a laser, a monochromator, and a photon detector. Raman microscopes are used to acquire Raman spectra of specific structures, pre-selected by using an optical microscope.[116] Thus, the chemical characteristics of structures under investigation can be analyzed selectively. Furthermore, it is possible to conduct Raman spectromicroscopy, also called Raman imaging. Thereby, the Raman scattered light of specific Raman bands is recorded while scanning the sample.[117] By conducting Raman microscopy label-free detection of specific chemical compounds within a sample is possible. However, several issues arise conducting Raman imaging.[118] Approximately, only one of a million photons is Raman scattered. This results in long image acquisition times and long irradiation times of single spots within the sample. The irradiation time can be reduced by increasing the laser intensity. However, increasing the laser intensity can have significant disadvantages for the samples, as well. Sample heating will result in sample damage, which is especially true for biological samples.[119] Also, Raman microscopy may suffer from significant fluorescence background.

Lately novel Raman microscopy methods were developed to overcome those drawbacks. Coherent anti-Stokes Raman Scattering (CARS) was reported as a method for label-free chemical contrast microscopy.[120,121] However, CARS suffer from non-resonant backgrounds and a nonlinear concentration dependence.[122] Stimulated Raman microscopy can be used as an alternative technique.[123] First reports on Stimulated Raman emission were made by Woodbury and Ng in 1962.[124]

Stimulated Raman microscopy is based on resonant excitation of vibrational states in molecules. The sample is excited by two laser beams with different frequencies that are spatially overlapped at the location of the sample. One beam is called the pump beam with the intensity I_p the other one is called the Stokes beam with the intensity I_s. Thereby, the

difference in frequencies matches a specific Raman band under investigation. The difference in frequency $\Delta\omega$ is called the Raman shift.

$$\Delta\omega = \omega_P - \omega_S \tag{E2.4.9}$$

Here, ω_P is the frequency of the pump beam and ω_S is the frequency of the Stokes beam. When both laser beams hit the sample an intensity transfer is observed, caused by resonant excitation of the probed molecule, which results in Raman scattered light. The pump beam experiences a loss, and the Stokes beam experiences a gain in intensity. If the Raman shift does not match a particular Raman band, Stimulated Raman Scattering will not occur. Still, also in Stimulated Raman microscopy non-resonant background must be considered.

The Raman gain and the Raman loss can be described by:

$$\Delta I_S \propto N \cdot \sigma_{Raman} \cdot I_P \cdot I_S \tag{E2.4.10}$$

$$\Delta I_P \propto -N \cdot \sigma_{Raman} \cdot I_P \cdot I_S \tag{E2.4.11}$$

, where N is the number of molecules within the probed volume and σ_{Raman} is the Raman scattering cross section of the molecule. [123]

The linear concentration dependency is of advantage when analyzing the measured data. Since Stimulated Raman Scattering is a resonant process the number of scattered photons is significantly increased. Therefore, Stimulated Raman microscopy can be used for Raman imaging with moderate laser powers and within acceptable data acquisition times. In 2010 also video rate Raman imaging is reported.[125]

The Setup

Commercially available components were used to develop a unique Stimulated Raman microscope. The development and characterization of this setup was part of this doctoral thesis. The Stimulated Raman microscope was built using a tunable, pulsed, picosecond laser and an inverted optical microscope. The setup is shown in Figure 2.4.4.

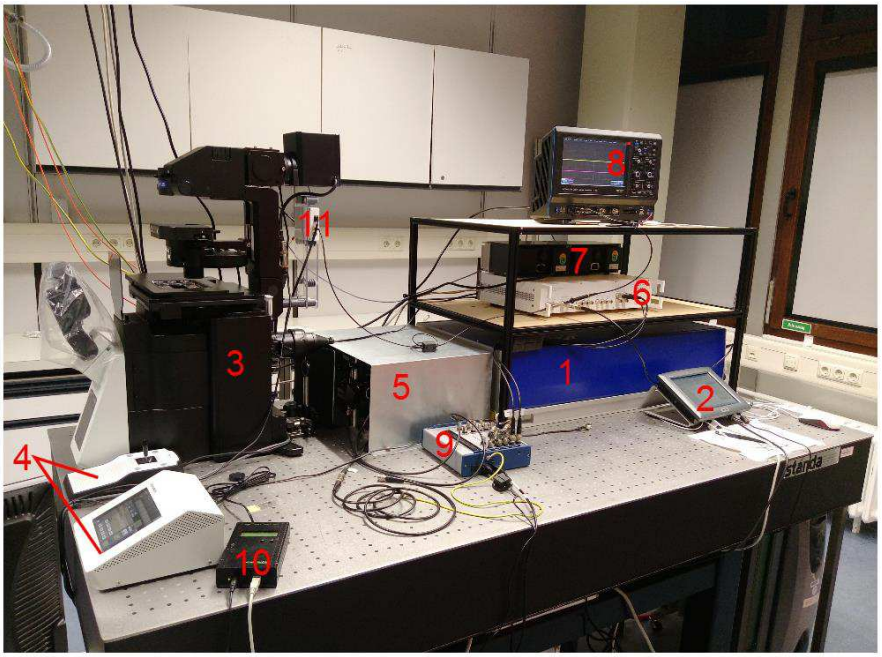

Fig. 2.4.4: The SRS microscope: (1) pulsed picosecond laser, (2) laser control panel, (3) inverted optical microscope, (4) microscope control and control panel, (5) cover shielding of the open optical path of the laser beam, (6) lock-in amplifier, (7) voltage source, (8) digital oscilloscope, (9) data acquisition module, (10) hygrometer, and (11) transimpedance amplifier.

A picoEmerald^{TM} laser (1) was purchased from the Angewandte Physik & Elektronic GmbH (APE Berlin, Germany) for the use within the Stimulated Raman setup. The picoEmerald^{TM} is designed to suit Stimulated Raman and coherent anti-stokes Raman scattering. Using an optical parametric oscillator (OPO) the picoEmerald^{TM} can generate picosecond pulses with wavelengths between 780 nm to 970 nm (OPO signal) and 1150 nm to 2030 nm (OPO idler). The generated OPO idler and OPO signal pulses as well as parts of the fundamental laser beam, a neodymium-doped yttrium orthovanadate laser (Nd:YVO_4) at 1064 nm, are individually available or at the same time. In Figure 2.4.5 the schematic view of the picoEmerald^{TM} laser main components and the optical path of the laser beam are illustrated.

The fundamental of the laser pulses is emitted at 1064 nm and at 532 nm for the second harmonic using a monopotassium phosphate crystal for frequency doubling. A dichroic mirror is splitting the two beams. The 1064 nm beam is guided towards the laser exit after being modulated to a repetition rate of 20 MHz by an electro-optical modulator. The 532 nm beam is guided towards the optical parametric oscillator. Here, wavelength tuning is conducted and the OPO signal as well as the OPO idler beam are guided to the same beam

exit as the fundamental beam of 1064 nm. The repetition rates of the signal and idler pulses are kept at 80 MHz. All three beams exit the picoEmerald™ at a single output port and therefore are overlapping in space at a defined time structure. The temporal overlapping between different pulses, which is mandatory for Stimulated Raman measurements, can be tuned via the installed software. Accessible Raman bands reach from 1400 cm^{-1} to 9000 cm^{-1} ($\Delta\nu$ signal – idler) and from 700 cm^{-1} to 3400 cm^{-1} ($\Delta\nu$ signal – pump). The 1064 nm beam at 20 MHz will be called "Stokes beam" and the wavelength modulated beam at 80 MHz will be called the "pump beam".

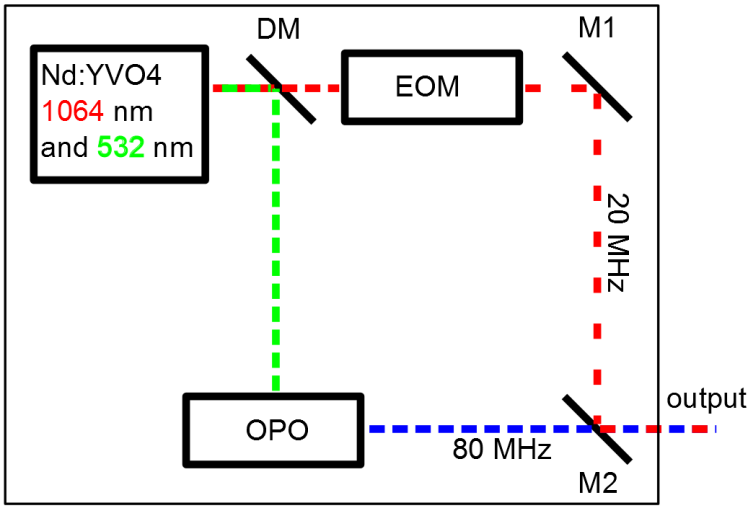

Fig. 2.4.5: Schematic view of the picoEmerald™ main components and the optical path of the laser pulses are shown. The Nd:YVO_4 laser, the optical parametric oscillator (OPO), the electro-optical modulator (EOM), the dichroic mirror (DM), and the mirrors (M1 and M2) for bending the beam path are indicated.

The maximum output powers of the picoEmerald™ laser are > 600 mW for the signal pulse, > 500 mW for the idler pulse, and > 750 mW for the fundamental beam. Output powers of around 180 mW were used. However, even at reduced output powers the skin samples sustained severe damage. Therefore, several neutral-density filters were set up to lower the output power by an order of magnitude. The initial output power was necessary for internal control cycles, keeping the laser stable. The laser power was measured by using a DET100A photo-detector, manufactured by Thorlabs, for the pump and the Stokes beam. A DET10A detector was used to measure the modulation of the pump beam. The used detectors differ in their rise time. The DET100A detector has a rise time of 43 ns, the DET10A detector has a rise time of 1 ns. The 1 ns rise time of the DET10A detector was necessary to detect the

modulation of the 80 MHz pump beam by the 20 MHz Stokes beam. The 80 MHz pulses correspond to a pulse every 12.5 ns. The modulation of the pump beam is monitored by a digital oscilloscope. A wavesurfer 3024 oscilloscope from LeCroy, with a bandwidth of 200 MHz, was used for this purpose.

The beam path outside of the picoEmerald^{TM} is schematically shown in Figure 2.4.6. After emission of a pulse by the laser, the laser pulse is guided into a beam expander (BE). The collimated light is expanded to a larger spot size avoiding damage to the optics. Mirrors (M1 and M2) are used to guide the beam towards the microscopy setup. After passing a neutral density filter (F1) the beam is divided by the beam splitter (BS1). Here, 40% of the beam is guided towards the power measurement setup while 60% are guided towards the microscope using a periscope (P). The beam is passing an adjustable slit (B) before being guided into the microscope. The periscope is needed to overcome the height difference between the exit port of the laser and the entrance slit of the microscope. The slit can be used to adjust the photon flux.

The part of the beam guided towards the power measurement setup passes a neutral density filter (F2) and hits a beam splitter (BS2). One part of the beam is guided towards the detector (D1) to monitor the modulation of the pulses by using the digital oscilloscope (OSC). The lens (L1) is needed to focus the beam onto the detector diode, with a surface area of 0.8 mm². The second part of the beam is guided to another beam splitter. One part of the beam is guided from there towards the detector (D2) which is used to measure the power of the pump beam. The beam passes the filter (F4) which blocks light at a wavelength of 1064 nm. The power of the Stokes beam is measured by the detector (D3). Here, the beam passes the filter (F3), where the pump beam is blocked. The current measured at both detectors (D2) and (D3) is gathered by the data acquisition module (DAQ, National Instruments), where the current is converted into a voltage. The amplitude of the voltage can be read by a personal computer (PC).

The beam guided towards the microscope is detected by the detector (D4) after passing the sample. The current is converted into a voltage by using a transimpedance amplifier (TA), which is also significantly reducing the background noise. The resulting voltage is guided towards the lock-in amplifier (Zurich Instruments), where the stimulated Raman loss signal is measured. The acquisition of the measurement signal at the lock-in amplifier is done by using a personal computer (PC).

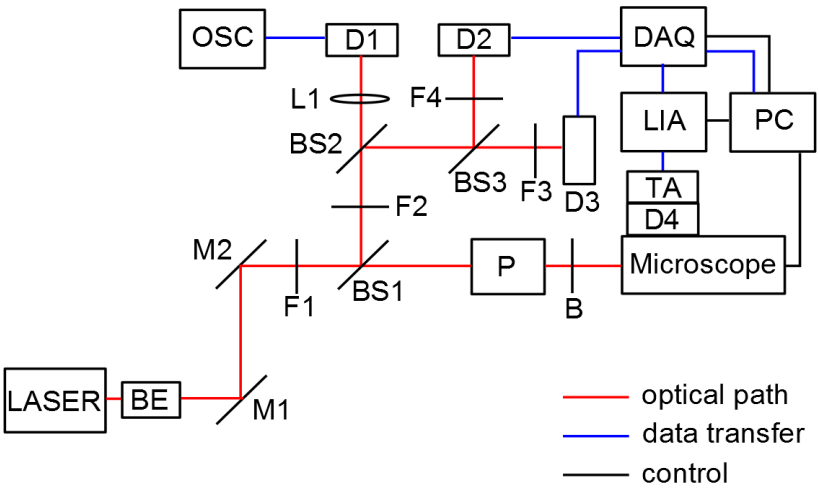

Fig. 2.4.6: Schematic overview of the Stimulated Raman microscopy setup. For detailed information on the components, see text. Acronyms are used as follows: beam expander (BE), mirror (M), filter (F), beam splitter (BS), lens (L), detector (D), oscilloscope (OSC), periscope (P), adjustable slit (B), data acquisition module (DAQ), lock-in amplifier (LIA), transimpedance amplifier (TA), and personal computer (PC).

Details on the microscope and the optical path of the laser beams within the microscope are shown in Figure 2.4.7. In Figure 2.4.7 (a) the IX83 inverted optical microscope (Olympus) and its controls for the x, y-stage, and the objectives are shown. The z-axis control for focusing the sample by moving the objectives is shown in Figure 2.4.7 (a1). The control stick shown in Figure 2.4.7 (a2) is connected to the Märzhäuser x, y-stage, which is used to move the sample that is mounted on this stage. The x, y-stage can also be moved by using CellSens or the Stimulated Raman microscopy program SRSLab. However, it is more intuitive to use the control stick. The control panel shown in Figure 2.4.7 (a3) is used for the microscope control including switching of the objectives and the adjustment of the illumination.

Figure 2.4.7 (b) shows the screens used to monitor information on the samples gathered by the optical microscope, including microscope controls (see Figure 2.4.7 (b1)), and for Stimulated Raman measurements (see Figure 2.4.7 (b2)). CellSens software was used for optical microscopy, which was acquired together with the IX83 inverted microscope from Olympus. For Stimulated Raman mapping a non-commercial software was used. Developing a Stimulated Raman mapping program was part of this doctoral thesis.

In Figure 2.4.7 (c) the optical paths of the laser beams within the IX83 microscope are shown. Laser beams entering the microscope are guided towards a beam splitter and are directed towards the objective, used to focus the laser beams onto the sample. For Stimulated Raman mapping the 20x and 50x objectives can be used. The 10x objective cannot be used because of its diaphragm used for phase-contrast imaging, which would suffer from radiation damage. After being focused on the sample, the transmitted light is gathered by the condenser. The pump beam and its Stimulated Raman loss signal, as a part of the transmitted light, are forwarded towards the detector (D4). The detector D4 is used to measure Stimulated Raman loss as well as measurements in transmission mode. The photodiode current of the detector (D4) is converted into a voltage by the transimpedance amplifier (TA). The resulting voltage is forwarded to the lock-in amplifier. The Stimulated Raman loss and the transmission signal can be acquired by the lock-in amplifier (LIA) using a computer (PC). The camera (CAM2) which is mounted close to detector (D4) is used for manual adjustment of the condenser. The halogen lamp (H), the camera (CAM1), and the eyepiece (EP) are used for optical microscopy.

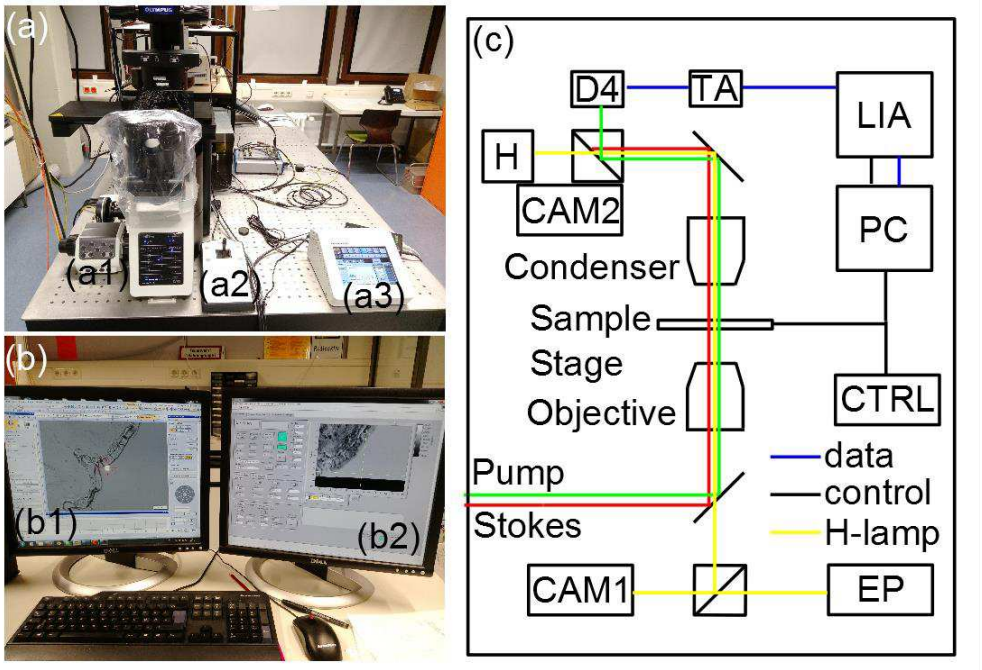

Fig. 2.4.7: IX83 inverse microscope (Olympus) used for Stimulated Raman studies. In (a) the inverted microscope IX 83 and its controls are shown. (a1) this control device is used for focusing the radiation onto the sample, (a2) a control stick for the Märzhäuser x, y-stage, (a3) control panel of the microscope. In (b) both screens for monitoring the sample information during data acquisition are shown. (b1) is used to monitor information of the

CellSens program and (b2) is used for the SRS program. In (c) the pathway of the laser beams within the IX 83 microscope are shown.

This setup is developed with special focus on combining Life Science microscopy with SRS studies. The benefits on combining several microscopy techniques using a single setup are explained in detail in Chapter 3.6.

Other methods, than SRS, available at this experimental setup are namely: bright field microscopy, phase contrast, fluorescence microscopy and hyper-spectral imaging at different wavelength.[126–129] All methods are commonly known, and a detailed description of all methods would exceed the purpose of this dissertation.

2.5 Sample Preparation

For X-ray microscopy and Stimulated Raman microscopy, different methods for sample preparation were used. All experiments were conducted in accordance with the Helsinki guidelines.[130] Human skin samples were used after the signed consent of the donors was received. All samples were prepared by collaboration partners at the Department of Dermatology, Venerology and Allergology of the Charité Universitätsmedizin Berlin

Sample Preparation for Scanning X-Ray Spectromicroscopy

After receiving the skin, either from plastic surgery in case of human skin or sacrificing a mouse for murine skin, the subcutaneous fat was removed. Afterwards, the skin was cleaned with sterile saline solution. The cleaned skin then was cut into pieces with a size allowing the treatment of 1 cm² of skin surface by the drug formulation. Skin pieces usually had a surface area of $2\ cm \cdot 2\ cm$. However, for mouse skin the skin size varied because of the small amount of skin available. Eventually, in dependence on the experimental needs skin pieces were treated by tape-stripping prior to drug application. This was conducted for experiments involving the investigation of the influence of an altered skin barrier. By using tape-stripping the topmost layer of the skin, the stratum corneum, was damaged by removing parts of it.[131] After cleaning, the skin was fixed onto Styrofoam plates with aluminum foil by using needles. The skin samples were then placed into an incubator to warm the skin to a temperature, comparable to skin temperature when not excised. Typically 32° C was used as the target skin temperature.[22] In earlier experiments also a Franz cell apparatus was used for skin treatment. While Franz cell preparation is different to the incubation chamber, results from both skin preparation methods were comparable to each other and yielded similar

results. After the skin reached the target temperature, which took approximately 10 min to 30 min, the skin was treated with the formulation to be tested for a set amount of time. The treated area had a size of 1 cm²; less for murine skin. Human skin samples during treatment are shown in Figure 2.5.1. After the drug treatment the remaining drug formulation was carefully removed by using a pipette or a cotton swab. In case a pipette was used, the remaining drug formulation was filled into a PCR tube and was finally stored. Also, one tape strip was applied to remove smaller remains of the drug formulation.

Fig. 2.5.1: Human skin sample fixed on styrofoam and aluminum foil during topical treatment. The target area for the topical treatment is indicated by the 4 black dots. This image was provided by the Department of Dermatology, Venerology and Allergology of the Charité Universitätsmedizin Berlin (Dr. Fiorenza Rancan).

After removing the remaining drug, samples were cut into $1\ mm \cdot 1mm \cdot 1mm$ pieces by using a razor blade. The 1 mm^3 skin pieces were fixed in 2.5% glutaraldehyde in 0.1 M Na-cacodylate buffer for 3 h. Subsequently a fixation of the skin samples in $1\%O_SO_4$, $0.8\%K_4[Fe(CN)_6]$ in 0.1 M cacodylate buffer was conducted for 1.5 h. The skin samples were dehydrated by rinsing with ethanol, starting at 50% ethanol concentration. By slowly increasing the ethanol concentration, samples were finally rinsed using pure ethanol. Subsequently, the samples were embedded in EPON (Electron Microscopy Science, Kit 812) resin. The embedded skin samples were cut to approximately 300 nm thin skin slices using an ultra-microtome RM2065 (Leica). Within the final step of sample preparation, the skin

slices were placed on silicon nitride membranes (Silson, U.K.) with a spatial extent of $500\ \mu m \cdot 500\ \mu m$ and a thickness of 100 nm (thickness of the silicon nitride membrane). In Figure 2.5.2 a 300 nm thick slice of a skin sample, mounted on a silicon nitride membrane, is shown by using a false color scale of the optical micrograph.

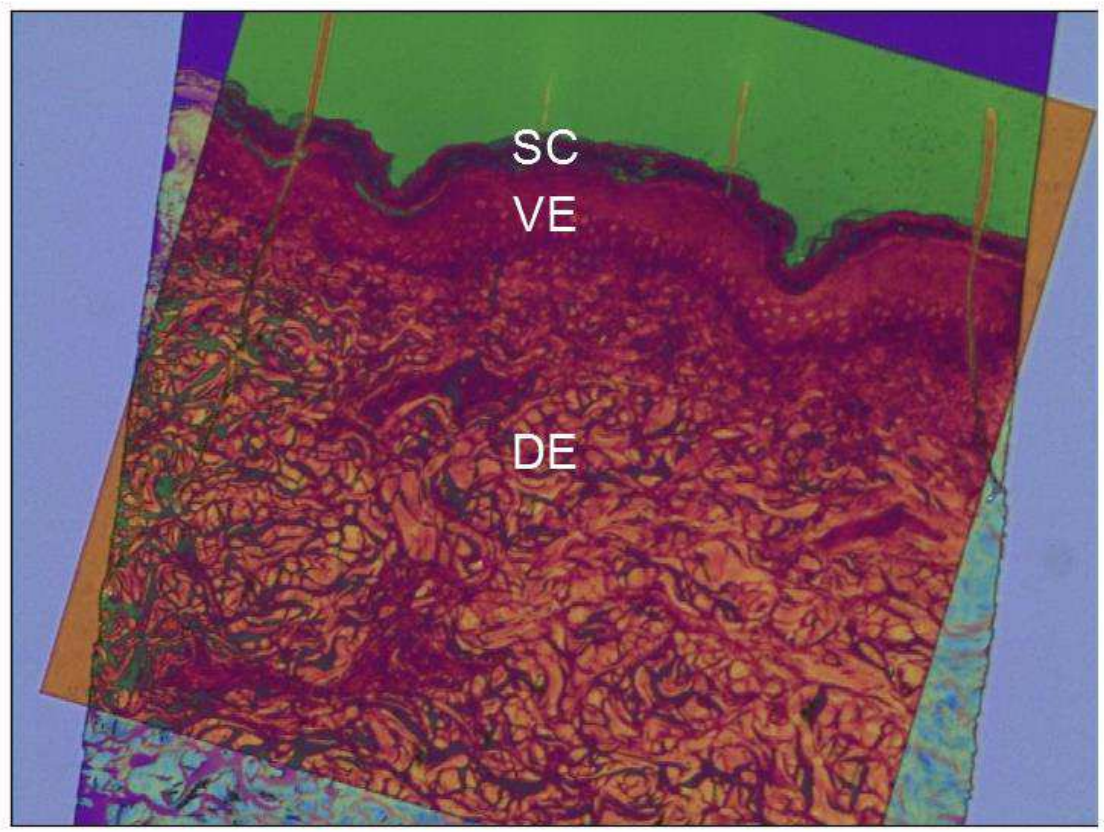

Fig. 2.5.2: Skin slice with a thickness of roughly 300 nm mounted onto a silicon nitride membrane. The optical micrograph is shown in a false color scale. The stratum corneum (SC), the viable epidermis (VE), and the dermis (DE) are indicated.

Sample Preparation for Stimulated Raman Spectromicroscopy

Sample preparation for Stimulated Raman Spectromicroscopy was less challenging compared to sample preparation for scanning X-Ray spectromicroscopy. Differences can be found in the preparation procedure after treatment of the sample.

Similar to sample preparation for scanning X-Ray spectromicroscopy a skin piece of $2\ cm \cdot 2\ cm$ was used for treatment. The skin was fixed on a Styrofoam block and put into an incubator. The drug formulation was applied on a 1 cm² surface. In this work measurements using fluorescent dye (fluorescein, 2 µg/cm²), for skin treatment, are reported. After a given incubation time, keeping the humidity and the temperature constant, the non-penetrated

formulation was removed by using cotton swabs. Subsequently, the treated area was cut into a $0.5\ cm \cdot 0.5\ cm$ piece. After cutting, the skin tissue was frozen using liquid nitrogen and stored at -20 °C. For the Stimulated Raman experiments the tissue was cut into 6 µm thick skin sections using a microtome. Prior to cryo-slicing the tissue was embedded in tissue freezing medium (Tissue-Tek®). After cutting, the sample is ready for the Stimulated Raman measurements.

3. Publications and Results

3.1 Selective Probing of the Penetration of Dexamethasone into Human Skin by Soft X-ray Spectromicroscopy

Author:
K. Yamamoto, R. Flesch, T. Ohigashi, S. Hedtrich, A. Klossek, P. Patoka, G. Ulrich, S. Ahlberg, F. Rancan, A. Vogt, U. Blume-Peytavi, P. Schrade, S. Bachmann, M. Schäfer-Korting, N. Kosugi, E. Rühl

Publication:
Analytical Chemistry

Publisher:
American Chemical Society

Date:
Jun 1, 2015

Anal. Chem. 2015, 87, 6173−6179

Online available at: https://doi.org/10.1021/acs.analchem.5b00800

Author contribution: In this work the author contributed to measurements, evaluating, and interpreting the results, and wrote parts of the publication.

analytical chemistry

Article

pubs.acs.org/ac

Selective Probing of the Penetration of Dexamethasone into Human Skin by Soft X-ray Spectromicroscopy

K. Yamamoto,[§] R. Flesch,[§] T. Ohigashi,[∥] S. Hedtrich,[¶] A. Klossek,[§] P. Patoka,[§] G. Ulrich,[§] S. Ahlberg,[†] F. Rancan,[†] A. Vogt,[†] U. Blume-Peytavi,[†] P. Schrade,[‡] S. Bachmann,[‡] M. Schäfer-Korting,[¶] N. Kosugi,[∥] and E. Rühl*[,§]

[§]Physikalische Chemie, Institut für Chemie und Biochemie, Freie Universität Berlin, 14195 Berlin, Takustrasse 3, Germany

[∥]Institute for Molecular Science, Myodaiji, Okazaki 444-8585, Japan

[¶]Institut für Pharmazie, Freie Universität Berlin, 14195 Berlin, Germany

[†]Klinisches Forschungszentrum für Haut-und Haarforschung, Charité Universitätsmedizin, 10117 Berlin, Germany

[‡]Abteilung für Elektronenmikroskopie at CVK, 13353 Berlin, Germany

ABSTRACT: Selective probing of dexamethasone in excised human skin using soft X-ray spectromicroscopy provides quantitative concentration profiles as well as two-dimensional drug distribution maps. Element- and site-selective excitation of dexamethasone at the oxygen K-edge with the lateral step width adjusted to 1 μm provides detailed information on the location of the drug in the different skin layers. The key of this work is to probe dexamethasone selectively at the carbonyl site (C3) by the O 1s $\rightarrow \pi^*$ transition, providing also a most efficient way to quantify the drug concentration as a function of penetration depth in correlation with structural properties of the skin containing carboxyl and amide oxygen sites occurring at higher transition energy than dexamethasone. Following drug exposure for 4 h, the glucocorticoide is located in about equal amounts in the stratum corneum, the outermost horny layer of skin, and in the viable epidermis, whereas in the dermis no dexamethasone is detected. In the stratum corneum, most of the lipophilic drug is found in regions between corneocytes, where epidermal lipids are dominating.

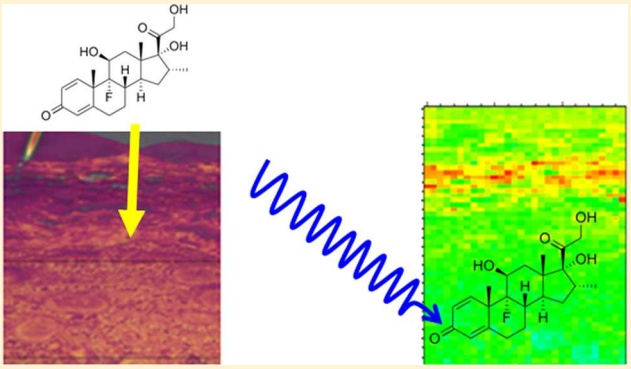

Skin absorption of drugs in various topical formulations is studied by a variety of different experimental approaches permitting to measure either in vivo or ex vivo the penetration or permeation profiles of substances overcoming the stratum corneum barrier.[1,2] In volunteers (in vivo studies), the stratum corneum can be removed stepwise by tape stripping of skin.[3] The amount of drug in the stratum corneum is reported to reflect penetration of viable skin and systemic availability.[4] For quantification, optical approaches[5] including infrared and Raman microscopy are used.[6−8] For ex vivo studies, the skin mounted to Franz diffusion cells is exposed to the drug for defined time periods. Then, the skin is removed and the penetrated drug is quantified either in full-thickness skin or within horizontal slices (e.g., 100 μm). Alternatively, the upper epidermis is heat separated form the dermis layer for analysis.[2] The permeated amount is retrieved from the drug concentration in the receptor fluid, respectively.[9,10] High-pressure liquid chromatography (HPLC)[2,11] is another preferred method for analyzing the drug distribution in skin.[2] In this context cryo sectioning techniques lead to a superior vertical resolution of skin sections reaching down to 20 μm, as has been demonstrated recently.[12] However, most of these approaches do not reach a spatial resolution on the subcellular level.

Furthermore, skin absorption studies are performed, in which, instead of a drug, dyes are used as a suitable model substances for visualizing the uptake and transport processes by fluorescence microscopy.[13−15] Confocal laser scanning microscopy and two-photon microscopy have the inherent advantage of high sensitivity reaching single-molecule detection.[16] Yet, this sensitive approach can be used for probing the uptake of drugs into skin only rarely, since most drugs are not fluorescent. Therefore, probing drugs within the skin requires label-free approaches, in which the intrinsic properties of the drug are used along with spectroscopy or spectromicroscopy. For example, Raman-based techniques are used for spatially resolved drug uptake studies,[17] and stimulated Raman microscopy is applied for depth profiling of substances in the upper skin layers.[18] More recently, drug uptake processes are studied by time-of-flight secondary ion mass spectrometry and

Received: February 28, 2015
Accepted: May 5, 2015
Published: May 5, 2015

DOI: 10.1021/acs.analchem.5b00800
Anal. Chem. 2015, 87, 6173−6179

scanning electron microscopy allowing for a multicomponent detection of skin lipids and drugs in high spatial resolution that can reach the submicron regime.[19] This is superior to matrix-assisted laser desorption/ionization mass spectrometry imaging (MALDI-MSI) studies, in which the spatial resolution is 30 μm.[20]

X-ray microscopy is a powerful label-free technique which has been used in the past for probing with high selectivity a variety of samples reaching from polymers,[21] to environmental samples, studies on single cells,[22] as well as the uptake of nanoparticles into human skin.[23] X-ray spectromicroscopy relies on the resonant excitation of the species under study in the soft and hard X-ray regime. This provides besides element selectivity also chemical selectivity, since the chemical shift of absorption bands yields site-selective information and the spatial distribution of the species under study.[24] Furthermore, thick samples, which may even include entire cells, can be investigated. This cannot be done by electron microscopy approaches. X-ray spectromicroscopy has the additional advantage that spatially resolved absorption maps can be quantified by using mass absorption coefficients in core ionization continua,[25] i.e., in spectral regions well above the near-edge structure. This approach has been used for several types of samples, such as, e.g., polymer membranes and films[26−28] as well as composite materials[29] and microcapsules.[30]

In this work we report on the penetration of dexamethasone into human skin ex vivo using scanning X-ray microscopy. The motivation for this study is to derive most detailed insights on the depth profile of the drug concentration and its spatial distribution in the upper skin layers. X-ray microscopy provides chemical selectivity by tunable soft X-rays, so that the absorption of skin is efficiently suppressed. Quantification of the results is also reported along with the skin layers in which dexamethasone is observed after topical application. These results are discussed along with previous data on glucocorticoid penetration[31] and regarding the role of the stratum corneum as both the penetration barrier and a reservoir for lipophilic, topically applied drugs.[32]

METHODS

Skin Samples, Uptake of Dexamethasone, and Sample Preparation. Freshly excised human abdominal skin from healthy donors undergoing plastic surgery was used for the experiments. The study was conducted with consent of the subjects, after approval by the Ethics Committee of the Charité—Universitätsmedizin Berlin and in accordance with the Declaration of Helsinki guidelines (approval EA/1/135/06 updated 05.2012). Skin was used a few hours after surgery. Subcutaneous fat was removed from the skin. Only regions of healthy skin were used, which contained neither scars nor coloring, etc. The viable skin was cut a few hours after excision into pieces of approximately 2 cm^2, and 20 μL of a solution containing 0.5 g dexamethasone dissolved in 100 mL of a 10:90 ethanol/water mixture was applied on a surface of 1 cm^2 in a humid chamber at 37 °C for 4 h. This corresponds to an initial dose of 100 μg/cm^2 (finite dose approach). After 4 h exposure at 37 °C, the superficial fluid was subsequently removed and one tape strip was applied to the dry skin to remove drug adhering to the skin surface. Subsequently, the skin was cut into 1 × 1 mm pieces and transferred into brown glass flasks, where it was fixed at room temperature for 3 h using 2.5% glutaraldehyde in 0.1 M Na-cacodylate buffer. A postfixation by 1% OsO_4, 0.8% $K_4[(Fe(CN)_6]$ in 0.1 M cacodylate buffer was done for 1.5 h. Dehydration was accomplished by rinsing the samples with increasing fractions of ethanol starting at 50% ethanol and reaching finally pure ethanol. The samples were successively embedded in epoxy resin EPON (Electron Microscopy Sciences, Kit 812). Finally, the embedded samples were selected for regions of interest and sliced into 350 nm sections using a microtome RM2065 (Leica). Finally, the skin samples were placed on silicon nitride membranes with a size of 500 μm × 500 μm and a thickness of 100 nm (Silson, U.K.). Optical microscopy studies on the samples were performed (MM-400/L, Nikon), which served for selecting areas of interest for X-ray microscopy studies.

The thickness of the skin sections was determined by atomic force microscopy (NeaSNOM, Neaspec). The instrument used has been described before.[33,34] It was used in the intermittent contact mode (tapping frequency between 146 and 267 kHz, typical tapping amplitude 60 nm, scan sizes 25 μm times 100 μm, resolution 0.625 μm/pixel, 0.5 μm/pixel, respectively). The substrate was set as the point of origin, and the step at the edge of the EPON film taken as the determined thickness at various positions for the samples under study. The results indicate that the samples under study had a thickness of 310 ± 10 nm. This information is used in the following to quantify the drug distribution. However, there were local regions that were more than 50 nm thicker, especially in the upper stratum corneum as a result of slightly irregular or ragged cuts or fraying of corneocytes.

X-ray Absorption and X-ray Microscopy. The experiments on X-ray absorption and X-ray microscopy were carried out at the UVSOR III synchrotron radiation facility (Institute for Molecular Science, Okazaki, Japan) at the BL4U beamline. The beamline consists of an in-vacuum undulator and a variable included angle Monk-Gillieson mounting monochromator, which is equipped with a varied-line-spacing plane grating.[35,36] The end station is a scanning X-ray microscope (Bruker ASC), in which the tunable soft X-rays are focused by a zone plate onto the sample. The X-rays transmitting through the sample and a blank window are measured by a photomultiplier (Hamamatsu R647P, equipped with a P 43 scintillator). X-ray absorption of the samples is derived from these measurements. During the experiments the slits of the X-ray monochromator were set to 50 μm, corresponding to an energy resolution ($E/\Delta E$) of typically 3000. The spatial step size during scans was set to 1 μm. Skin samples were investigated up to a depth of 500 μm from the skin surface, but it turned out that dexamethasone-specific X-ray absorption was only detected in the upper 100 μm, i.e., near the skin surface. The energy scale of the monochromator was carefully calibrated by using gaseous CO_2 for calibrating the O 1s regime.[37]

Model Calculations. The assignment of the near-edge spectrum of dexamethasone is performed by quantum chemical calculations using the following approach: ab initio quantum chemical calculations on the O 1s transitions into the lowest unoccupied orbitals probed by near-edge spectra were carried out by using the GSCF3 code.[38,39] The geometry was optimized by the second-order Møller−Plesset perturbation theory using the 6-31G(d,p) basis set. The ground and O 1s excited states were obtained from the Hartree−Fock method, namely, ΔSCF (self-consistent field), which gives reasonable term values for core-to-valence transitions. The core hole was localized on a specified oxygen atom. Primitive Gaussian-type basis functions (73/7) and (6) were contracted as (3111121/3112) for O atoms, (721/52) for C atoms, and (42) for H

DOI: 10.1021/acs.analchem.5b00800
Anal. Chem. 2015, 87, 6173−6179

atoms.[40] Primitive 3s3p2d diffuse functions on each core excited oxygen atom were added.[41]

RESULTS AND DISCUSSION

Figure 1 shows the O 1s excitation regime, corresponding to the oxygen K-edge, of fixed human skin (blue trace, Figure 1a)

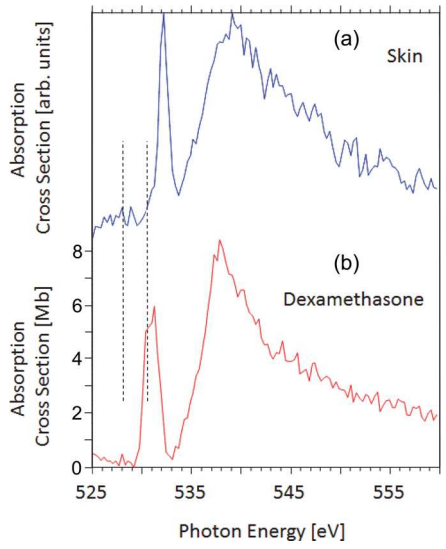

Figure 1. X-ray absorption cross section of (a) fixed in Epon resin embedded human skin and (b) dexamethasone at the O K-edge. Vertical dashed lines visualize the photon energies used for the experiments at 528.0 and 530.6 eV, respectively.

and dexamethasone (red trace, Figure 1b). The near-edge spectrum of both species is essential for gaining chemical selectivity in order to probe the drug distribution in fixed human skin. This has not been reported before to the best of our knowledge.

Dexamethasone ((11β,16α)-9-fluoro-11,17,21-trihydroxy-16-methylpregna-1,4-diene-3,20-dione, $C_{22}H_{29}FO_5$) has two differently bound oxygen sites contributing to the near-edge structure in the O 1s regime: (i) two carbonyl groups bound at C3 and C20 and (ii) three hydroxyl groups bound at C11, C17, and C21, respectively. In analogy to earlier work (cf. refs 42−44), the lowest energy resonance centered at 531 eV is assigned to the O 1s → π^* transition, which is due to the carbonyl groups. It is evident that this resonance is fairly broad, and its intensity relative to the O 1s continuum is weak. This points to the fact that both carbonyl groups in dexamethasone are located in different chemical environments. This gives evidence for a chemical shift, as can be deduced from earlier work obtained from electron energy loss spectroscopy on similar molecular systems.[45] As a result, the lower energy portion of the band centered at 531 eV is evidently due to the quinoic carbonyl (C3), similar to *p*-benzoquinone, where the corresponding resonance is observed at 529.85 eV.[45] The higher portion of this resonance is expected to be similar to acetone, where the O 1s → π^* transition occurs at 531.3 eV,[42] resembling the present results on dexamethasone at C20. These considerations are consistent with results from model calculations, as shown in Table 1. There, theoretical transition energies to the lowest O 1s excited states, i.e., carbonyl and hydroxyl oxygen sites, in dexamethasone are compared to the experimental values. Clearly, the lowest energy feature at 530.6 eV in the experimental spectrum is due to the C3 site, as shown

Table 1. Comparison of the Experimental and Calculated O 1s Excitation Energies into the Lowest Unoccupied Orbitals of Dexamethasone in eV

	carbonyl oxygen O 1s → π^*	hydroxyl oxygen O 1s → σ^*_{O-H}
experimental	530.6[a]	534.5
	531.2[b]	
theoretical	530.05[a]	534.46[c]
	530.57[b]	534.82[d]
		535.25[e]

[a]Oxygen site bound to C3. [b]Oxygen site bound to C20. [c]Oxygen site bound to C11. [d]Oxygen site bound to C17. [e]Oxygen site bound to C21.

in Figure 1b. The other higher energy feature at 531.2 eV is due to the C20 site. A shoulder is observed at 534.5 eV, which is according to the model calculations due to O 1s → $\sigma^*_{(OH)}$ transitions, similar to earlier experimental work. These have slightly different transition energies, as they are bound to C11, C17, and C21, respectively, and cannot be resolved in the experimental spectrum (cf. Figure 1b and Table 1).

The dominant higher energy, intense feature near 538 eV is due to the O 1s → σ^* transition, which is typical for the oxygen bound in carbonyl groups. In addition, alcohols are known to show a lower energy feature which is due to excitations into low-lying Rydberg states. Such resonances have been observed in methanol at 534.1 eV.[43] However, it is known that such features can easily vanish in complex environments, such as clusters.[46] Therefore, it is not surprising that no such sharp Rydberg-type resonance is observed in dexamethasone (cf. Figure 1b).

The near-edge spectrum of fixed skin is shown in Figure 1a (blue trace). The composition of fixed skin samples is complex, so that we do not speculate here about detailed spectral assignments. The X-ray absorption spectrum of fixed skin was investigated at different locations and depths. We did not find significant changes in O 1s near-edge spectra. Briefly, the near-edge spectrum shows an intense resonance at 532 eV, which is tentatively assigned to carboxyl and amide oxygen sites, which appears to be reasonable due to the occurrence of ceramides in the stratum corneum.[47] The continuum intensity is weak, and the broad feature near 540 eV is due to an O 1s → σ^* transition, similar to previous spectroscopic work on epoxy resins.[48]

The most important finding from the spectroscopic results is that dexamethasone can be clearly distinguished from the skin by characteristic differences in absorption properties near the O K-edge. This is of importance for the following results where this spectral selectivity is used to probe the penetration of topically applied dexamethasone into human skin by X-ray microscopy. Two photon energies were chosen for determining the differential absorption that is due to the drug: (i) 528.0 eV, corresponding to the pre-edge regime that gives rise to weak absorption, and (ii) 530.6 eV. This photon energy corresponds to the lower energy portion of the O 1s → π^* transition of the drug. This is due to an excitation of dexamethasone at the quinoic carbonyl site (bound to C3), as outlined above. We have chosen the lower energy part of this resonance, in order for the skin to be as transparent as possible, so that the chemical contrast due to dexamethasone is as high as possible. Note that dexamethasone also contains at C9 a fluorine site. Therefore, we also attempted to perform experiments in the F

DOI: 10.1021/acs.analchem.5b00800
Anal. Chem. 2015, 87, 6173−6179

1s regime (680−710 eV). However, the photon flux of the X-ray monochromator was too low to obtain usable results.

Figure 2a shows a representative skin section that was investigated by optical microscopy providing detailed information on the morphology of the skin sample under study. The layered structure of the anuclear stratum corneum (SC) extends to a depth of approximately 10−20 μm followed by the viable epidermis (VE) with the stratum granulosum and deeper strata. Viable keratinocytes with cell nuclei are found in a depth region between ca. 20 and 80 μm. The underlying dermis (D) can easily be distinguished from the epidermis due to distinct differences in morphology.

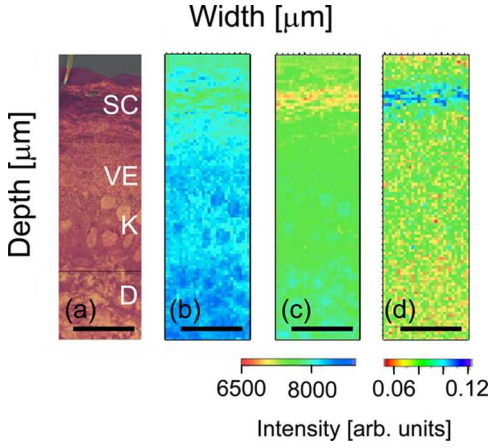

Figure 2. Uptake of dexamethasone into human skin (SC, stratum corneum; VE, viable epidermis; K, nuclei of keratinocytes; D, dermis): (a) optical micrograph of a vertical skin section of 30 μm × 100 μm; (b) absorption of the same skin section shown in (a) at 528.0 eV (pre-edge regime); (c) absorption of the same skin section shown in (a) at 530.6 eV (O 1s → π^* resonance); (d) optical density of taken up dexamethasone as a function of depth. The scale bar corresponds to 20 μm.

X-ray microscopy studies were performed using the same area of the skin section shown in Figure 2a at 528.0 eV (see Figure 2b) and 530.6 eV (see Figure 2c), respectively. The internal skin structure is clearly visible from Figure 2b and c and serves to match the positions of the optical and X-ray micrographs within the accuracy of the chosen pixel size, i.e., ± 1 μm. Note that the micrographs have been taken at constant photon flux, since the UVSOR III storage ring was operated in the top-up mode at typically 300 mA current, which facilitates quantifying the spatially resolved absorption of dexamethasone in fixed human skin. No indication of radiation damage was observed, as evidenced from repeated scans of the same sample.

Figure 2d shows the result of data reduction, where the differential absorption was determined from both photon energies according to Beer−Lambert law. Specifically, the color scale corresponds to $\ln(I(528.0\ \text{eV})/I(530.6\ \text{eV}))$. After 4 h of topical exposure, the local drug concentration is highest in the upper skin layers of the stratum corneum (SC), as indicated by the false color presentation. Strong extinction is indicated by blue color in the SC, whereas green color dominates in the viable epidermis (VE). This is due to lower local drug concentration as compared to the stratum corneum. Yellow and red color indicates lower concentrations and thus minor dexamethasone access to the dermis (D) (cf. Figure 2d). This qualitative result is in accordance with earlier drug uptake studies.[32,49] We also note that the concentration profile is qualitatively similar to the skin penetration of the glucocorticoids betamethasone valerate and prednicarbate,[31] as well as more recent work on the uptake of the macrolide tacrolimus into human skin,[12] despite the fact that tacrolimus is significantly more voluminous than dexamethasone. In fact, the molecular mass of tacrolimus ($C_{44}H_{69}NO_{12}$) is at the cutting edge of skin penetration (804.02 g mol^{-1}). For the first time we show that there is only minor dexamethasone access for the distinct nuclei of keratinocytes detectable in the viable epidermis (labeled as K in Figure 2a), where no distinct changes in X-ray absorption are observed.

Besides two-dimensional aspects of drug uptake, i.e., the extent of penetration, further insights into drug concentration profiles were gained. These are obtained from summing the changes in differential absorption, so that a depth profile of dexamethasone concentration is derived (see Figure 3a, red curve). In addition, an untreated reference skin sample was investigated in order to rule out any cross sensitivity that can be due to other species which might be contained in low concentration in fixed, embedded skin and are also absorbing at 530.6 eV. Indeed, a small, but distinct depth profile is observed for an untreated skin sample, corresponding to the blue curve in Figure 3a. This is due to other substances which show changes in differential absorption at the chosen photon energies, i.e., 530.6 and 528.0 eV, respectively. Clearly this is not due to the resin which is used for fixing the skin. It is rather assumed that traces of other species besides dexamethasone, such as carbonyl compounds contained in skin or even natural steroids, explain this cross sensitivity, which is found with highest concentration in the stratum corneum. Therefore, this component must be subtracted, so that exclusively the contribution of the topically applied drug is considered and quantified in the following. As a result, the difference between the red and the blue curve is due to dexamethasone, since all other parameters have been kept identical in the skin exposure and fixation protocols. Quantification of the results requires according to Beer−Lambert law (eq 1) that the change in absorption cross section σ between both photon energies (528.0 and 530.6 eV, respectively) and the sample thickness d is known.

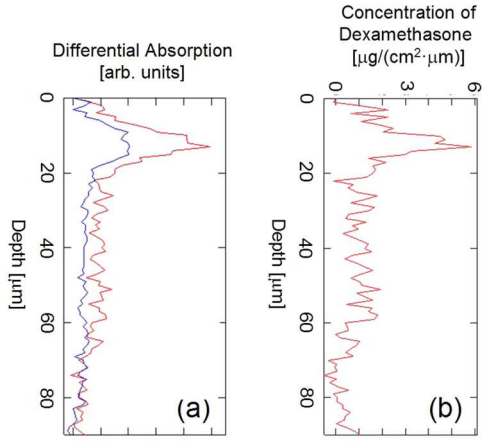

Figure 3. (a) Depth profile of differential absorption of dexamethasone penetrating human skin (red curve, exposure time: 4 h, data taken from Figure 2d). The blue curve corresponds to a concentration profile of untreated skin; (b) depth profile of dexamethasone concentration (see text for further details).

DOI: 10.1021/acs.analchem.5b00800
Anal. Chem. 2015, 87, 6173−6179

$$\ln(I_0/I) = \sigma \cdot d \cdot (N/V) \quad (1)$$

The results can be easily quantified using the known atomic mass absorption coefficient of the sample under study.[25] Both experimental quantities I and I_0, corresponding to the attenuation of X-rays due to skin and dexamethasone, are referenced either to the EPON resin in which the skin is embedded or to the dermis, respectively. Both regions are assumed to contain no dexamethasone, yielding comparable results. N/V corresponds to the drug concentration, which can also be expressed by the mass of drug found in a given sample volume. In the present work we used 1 μm step width for the spatially resolved scans probing the drug uptake. It has to be noted that the spatial resolution of the X-ray microscope is about a factor 30 higher than the selected step width, indicating that the full potential of this method is not exploited in this study.

The following approach is used to determine the absorption cross section near the O 1s absorption of dexamethasone, corresponding to the vertical scale of Figure 1b: The sum of the atomic mass absorption coefficients of the drug in the O 1s continuum (E = 560 eV) is used to determine the absolute cross section of the O 1s $\rightarrow \pi^*$ transition at 530.6 eV, which is not known to date. The difference in mass absorption coefficient between 560 and 525 eV is derived from ref 25, using the Optical Grapher Program. This yields a O 1s continuum cross section σ at 560 eV of 1.8 $\pm$ 0.2 Mb, where 1 Mb corresponds to 10^{-22} m^2. The maximum of the O 1s $\rightarrow \pi^*$ resonance at 531 eV corresponds with this calibration to a cross section σ of 5.7 $\pm$ 0.2 Mb. At 530.6 eV, where the experiments were performed, the cross section is slightly lower, i.e., 5.1 $\pm$ 0.2 Mb. Note that the same procedure cannot be applied to the near-edge spectrum of fixed skin (cf. Figure 1a), since the stoichiometry of this sample is not exactly known.

Furthermore, the thickness of the sample d is determined by atomic force microscopy yielding 310 $\pm$ 10 nm, as measured by random checks over the entire skin sample (500 μm $\times$ 500 μm). In the small area of the investigated sample (100 μm $\times$ 30 μm), the error limit is expected to be smaller. In addition, the thickness of the reference skin sample that was not exposed to dexamethasone had a thickness d = 350 $\pm$ 10 nm. With this information one derives quantitatively the vertical drug distribution after 4 h exposure. Note that the dose was 100 $\pm$ 5 μg/cm^2. In the stratum corneum one finds a drug concentration of 50 $\pm$ 25 μg/cm^2, corresponding in the peak concentration to 5.5 $\pm$ 1.5 μg/cm^2 per μm depth, as shown in Figure 3b. This sizable error limit is determined by considering the following sources of error: (i) uncertainty in absorption cross section ($\pm$0.2 Mb); (ii) uncertainty in sample thickness ($\pm$10 nm); (iii) normalization of the statistical noise using either the resin in which the skin is embedded, i.e., the region above the skin surface, or the dermis, in which no drug is detected. Note that both approaches yield similar results, but for the analysis of the data the resin appears to be more straightforward, since we cannot exclude that there is drug contained in the dermis. Evidently, the highest contribution to this error limit arises from heterogeneities of the skin sample. Indeed, the present experiments indicate that different parts of the skin sample contain different amounts of drug due to the variability in local structural properties, as can be seen from the data shown in Figure 2. This implies that after 4 h the highest amplitude of drug concentration is found in the stratum corneum (SC). The drug concentration shows in the viable epidermis a significantly lower local concentration; i.e., the drug is more diluted in the viable epidermis than in the stratum corneum. Nevertheless, if one sums the drug load in the viable epidermis (VE), a similar value of 50 $\pm$ 25 μg/cm^2 is derived. This is due to the fact that the volume of the VE compartment is larger than that of the SC. However, the local drug concentration is quite low, not exceeding 2.0 μg/cm^2 per μm depth. The vertical drug distribution appears to be quite noisy in the viable epidermis. This is clearly due to low and nonuniform local drug concentration. Therefore, the noise level is at least in part due to the distribution of cell nuclei in the skin section under study, which is not leveled out due to the limited size of the skin section that is used for horizontal summation of the drug concentration in order to derive Figure 3.

There is no drug observed in the lower skin layer, i.e., the dermis (D). Clearly, there is a significant drop in drug concentration near the basal membrane, i.e., the boundary between the epidermis and the dermis, indicating that virtually no dexamethasone is found in the dermis. This result is supported by the fact that, according to the present data, 100 $\pm$ 35 μg/cm^2 of the drug penetrated into skin. This appears to be consistent with the amount of dexamethasone (100 $\pm$ 5 μg/cm^2) that was applied to the skin surface.

It is also noted that this value is quite realistic considering that a small amount of nonadsorbed solution volume was wiped off from the skin surface and the single tape strip removing the outermost layer of the stratum corneum prior to skin fixation. It is estimated that this fraction of nonpenetrated drug can be up to 10 $\pm$ 5 μg/cm^2, indicating that the mass balance of the administered drug can be retrieved and that the penetration of dexamethasone into the dermis is evidently small after 4 h exposure time. These numbers appear to be reasonable and consistent and underscore that one can derive a quantitative understanding on drug uptake and distribution by X-ray microscopy. It should also be kept in mind that especially in the viable epidermis the local drug concentration is slightly above the noise level, which hampers on the one hand the reduction of error limit, but on the other hand very low concentrations of dexamethasone are clearly probed.

Furthermore, the question arises why there is no dexamethasone probed in the dermis. Most likely, more drug will gain access to the dermis with prolonged exposure.[10,14] Moreover, the resistivity in the dermis is significantly lower than in the viable epidermis, and dexamethasone rapidly gains access to the acceptor medium, probed by in vitro testing, and dermal blood vessels that are probed in vivo, respectively. The experimental results (Figure 3b) show a gradient in drug concentration near a depth of 60 μm. This implies that in the dermis the permeability of the drug is higher than in the viable epidermis, which explains together with the large volume of the dermis that no drug can be probed in deeper skin layers. This result is also in agreement with earlier work, in which percutaneous penetration of steroids was systematically investigated and systemic effects of topically applied dexamethasone have been found.[50] However, considering the mass balance outlined above, the amount of drug penetrating into the dermis must be negligibly small after 4 h of topical treatment.

Finally, Figure 4 shows in close-up a comparison of the region in the SC near the skin surface, where the optical micrograph (Figure 4a) is compared to the drug distribution in the same sample, as shown in Figure 4c.

Figure 4b shows the superposition of both images. There are clearly regions in which drug uptake is observed, as indicated by

DOI: 10.1021/acs.analchem.5b00800
Anal. Chem. 2015, 87, 6173−6179

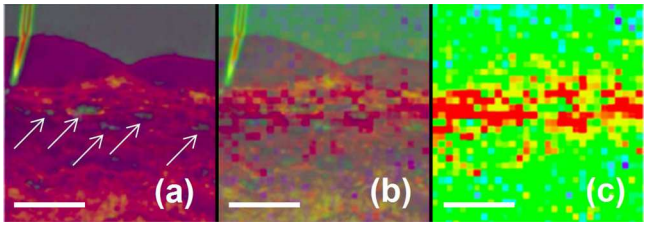

Figure 4. Detailed view on the spatially resolved uptake of dexamethasone into human skin in the stratum corneum: (a) optical micrograph; (b) superposition of X-ray absorption and optical micrograph; (c) X-ray absorption. Red areas correspond to high differential absorption by dexamethasone; green areas correspond to low differential absorption. Thin white arrows in (a) mark regions of corneocytes (see text for details). The scale bar corresponds to 10 μm.

red color in Figure 4b and c. It is aimed to determine specific regions in which drug uptake occurs. It is expected that the lipophilic drug dexamethasone should predominantly be found in the areas between the corneocytes, in which lipids, such as ceramides, free fatty acids, cholesterol, and cholesterol esters, occur.[47] Using the classical bricks and mortar model for the stratum corneum,[51] one expects that the drug should be predominantly found in the mortar, i.e., in the lipophilic region between the corneocytes. The structures observed in Figure 4a require an assignment regarding the location of corneocytes. These correspond evidently to the gray regions in which no drug is observed (cf. white arrows in Figure 4a), according to X-ray absorption. Further evidence for this assignment comes from additional atomic force microscopy studies. There, the thickness of the sample varies tremendously, so that the gray areas correspond to sections that are by about 50 nm thicker than the surrounding areas. These are clearly parts of the stratum corneum that are not well cut by the ultramicrotome knife. One would assume that thicker sections of the skin increase the absorption length, which would make these parts of the sample more sensitive to X-ray absorption of dexamethasone, if the drug would be taken up by these parts of the sample. However, this is evidently not observed and underscores the result that in these sections no drug uptake is observed, which is evidently due to corneocytes.

CONCLUSIONS

X-ray microscopy has been used to probe selectively the uptake of dexamethasone into human skin with a lateral resolution of 1 μm. Chemical selectivity is provided by resonant excitation of the carbonyl O 1s $\rightarrow \pi^*$ transition of dexamethasone at the C3 site. Its excitation energy is different from that of skin containing carboxyl and amide oxygen sites, so that exclusively this drug is probed. This provides details on the uptake routes and the drug distribution in the stratum corneum and the viable epidermis. After 4 h of exposure almost the total amount of drug is found in the stratum corneum and in the viable epidermis, whereas no dexamethasone is found in the dermis. The highest local drug concentration is observed in the stratum corneum, where the lipophilic phase around the corneocytes acts as a reservoir for dexamethasone. Lower local drug concentration is observed in the viable epidermis, where the drug is more evenly distributed, but evidently no drug is taken up into the cell nuclei of the keratinocytes.

X-ray microscopy bears the potential to probe drugs and drug carriers in biological samples without the use of any label. Note that only a single skin sample is discussed in this work, but it is evident from the present findings that these are of general use to probe quantitatively drug penetration in human skin. The full potential of this method is not fully exploited in this work, since the spatial resolution can be routinely as high as 20−30 nm. This appears feasible for subsequent work, so that further details on transport processes, which go beyond the scope of this work, can be investigated by label-free spectromicroscopy using tunable soft X-rays.

AUTHOR INFORMATION

Corresponding Author

*E-mail: ruehl@zedat.fu-berlin.de.

Author Contributions

The manuscript was written through contributions of all authors.

Notes

The authors declare no competing financial interest.

ACKNOWLEDGMENTS

Financial support by German Research Foundation (DFG) within SFB 1112 is gratefully acknowledged. Support of this work by the Institute for Molecular Science and Freie Universität Berlin is gratefully acknowledged. We thank G. Ulm (Physikalisch-Technische Bundesanstalt, Berlin) for the access to the atomic force microscope. We thank Yu-Fu Wang (Tamkang University, Taiwan) for preliminary theoretical calculations on dexamethasone and his help during the beam time. N.K. acknowledges financial support by JSPS Grant-in-Aid for Scientific Research (A) (No. 26248010).

REFERENCES

(1) Selzer, D.; Abdel-Mottaleb, M.; Hahn, T.; Schaefer, U.; Neumann, D. *Adv. Drug Delivery Rev.* **2013**, *65*, 278−294.
(2) Gysler, A.; Kleuser, B.; Sippl, W.; Lange, K.; Korting, H. C.; Höltje, H.-D.; Schäfer-Korting, M. *Pharm. Res.* **1999**, *16*, 1386−1390.
(3) Lademann, J.; Weigmann, H. J.; Rickmeyer, C.; Barthelmes, H.; Schaefer, H.; Mueller, G.; Sterry, W. *Skin Pharmacol. Appl. Skin Physiol.* **1999**, *12*, 247−256.
(4) Dupuis, D.; Rougier, A.; Roguet, R.; Lotte, C. *Br. J. Dermatol.* **1986**, *115*, 233−238.
(5) Wartewig, S.; Neubert, R. H. H. *Adv. Drug Delivery Rev.* **2005**, *57*, 1144−1170.
(6) Tfayli, A.; Piot, O.; Manfait, M. *J. Biophoton.* **2008**, *1*, 140−153.
(7) Tfayli, A.; Piot, O.; Pitre, F.; Manfait, M. *Eur. Biophys. J.* **2007**, *36*, 1049−1058.
(8) Ashtikar, M.; Matthäus, C.; Schmitt, M.; Krafft, C.; Fahr, A.; Popp, J. *Eur. J. Pharm. Sci.* **2013**, *50*, 601−608.
(9) OECD. *Test No. 428: Skin Absorption: In Vitro Method*; OECD Publishing: Paris, 2004.
(10) Schäfer-Korting, M.; Bock, U.; Diembeck, W.; Duesing, H. J.; Gamer, A.; Haltner-Ukomadu, E.; Hoffmann, C.; Kaca, M.; Kamp, H.; Kersen, S.; Kietzmann, M.; Korting, H. C.; Krachter, H. U.; Lehr, C. M.; Liebsch, M.; Mehling, A.; Mueller-Goymann, C.; Netzlaff, F.; Niedorf, F.; Rubbelke, M. K.; Schaefer, U.; Schmidt, E.; Schreiber, S.; Spielmann, H.; Vuia, A.; Weimer, M. *ATLA* **2008**, *36*, 161−187.
(11) Medendorp, J. P.; Paudel, K. S.; Lodder, R. A.; Stinchcomb, A. L. *Pharm. Res.* **2007**, *24*, 186−193.
(12) Lapteva, M.; Mondon, K.; Möller, M.; Gurny, R.; Kalia, Y. N. *Mol. Pharmaceutics* **2014**, *11*, 2989−3001.
(13) Küchler, S.; Radowski, M. R.; Blaschke, T.; Dathe, M.; Plendl, J.; Haag, R.; Schäfer-Korting, M.; Kramer, K. D. *Eur. J. Pharm. Biopharm.* **2009**, *71*, 243−250.
(14) Alnasif, N.; Zoschke, C.; Fleige, E.; Brodwolf, R.; Boreham, A.; Rühl, E.; Eckl, K. M.; Merk, H. F.; Hennies, H. C.; Alexiev, U.; Haag,

DOI: 10.1021/acs.analchem.5b00800
Anal. Chem. 2015, 87, 6173−6179

R.; Küchler, S.; Schäfer-Korting, M. *J. Controlled Release* **2014**, *185*, 45−50.
(15) Rancan, F.; Papakostas, D.; Hadam, S.; Hackbarth, S.; Delair, T.; Primard, C.; Verrier, B.; Sterry, W.; Blume-Peytavi, U.; Vogt, A. *Pharm. Res.* **2009**, *26*, 2027−2036.
(16) So, P. T. C.; Dong, C. Y.; Masters, B. R.; Berland, K. M. *Annu. Rev. Biomed. Eng.* **2000**, *2*, 399−429.
(17) Wang, P.; Li, J.; Wang, P.; Hu, C.-R.; Zhang, D.; Sturek, M.; Cheng, J.-X. *Angew. Chem., Int. Ed.* **2013**, *52*, 13042−13046.
(18) Freudiger, C. W.; Min, W.; Saar, B. G.; Lu, S.; Holtom, G. R.; He, C. W.; Tsai, J. C.; Kang, J. X.; Xie, X. S. *Science* **2008**, *322*, 1857−1861.
(19) Sjövall, P.; Greve, T. M.; Clausen, S. K.; Moller, K.; Eirefelt, S.; Johansson, B.; Nielsen, K. T. *Anal. Chem.* **2014**, *86*, 3443−3452.
(20) Hart, P. J.; Francese, S.; Claude, E.; Woodroofe, M. N.; Clench, M. R. *Anal. Bioanal. Chem.* **2011**, *401*, 115−125.
(21) Raabe, J.; Tzvetkov, G.; Flechsig, U.; Böge, M.; Jaggi, A.; Sarafimov, B.; Vernooij, M. G. C.; Huthwelker, T.; Ade, H.; Kilcoyne, D.; Tyliszczak, T.; Fink, R. H.; Quitmann, C. *Rev. Sci. Instrum.* **2008**, *79*, 113704 (10 pages).
(22) Schneider, G.; Guttmann, P.; Heim, S.; Rehbein, S.; Mueller, F.; Nagashima, K.; Heymann, J. B.; Müller, W. G.; McNally, J. G. *Nat. Methods* **2010**, *7*, 985−988.
(23) Graf, C.; Meinke, M.; Gao, Q.; Hadam, S.; Raabe, J.; Sterry, W.; Blume-Peytavi, U.; Lademann, J.; Rühl, E.; Vogt, A. *J. Biomed. Opt.* **2009**, *14*, 021015(9 pages).
(24) Lawrence, J. R.; Swerhone, G. D. W.; Dynes, J. J.; Korber, D. R.; Hitchcock, A. P. *J. Microsc.* **2014**, DOI: 10.1111/jmi.12156.
(25) Henke, B.; Gullikson, E.; Davis, J. *At. Data Nucl. Data Tables* **1993**, *54*, 181−342.
(26) Koprinarov, I. N.; Hitchcock, A. P.; McCrory, C. T.; Childs, R. F. *J. Phys. Chem. B* **2002**, *106*, 5358−5364.
(27) Collins, B.; Ade, H. *J. Electron Spectrosc. Relat. Phenom.* **2012**, *185*, 119−128.
(28) McNeill, C.; Ade, H. *J. Mater. Chem. C* **2013**, *1*, 187−201.
(29) McNeill, C. R.; Watts, B.; Thomsen, L.; Belcher, W. R.; Kilcoyne, A. L. D.; Greenham, N. C.; Dastoor, D. C. *Small* **2006**, *2*, 1432−1435.
(30) Araki, T.; Hitchcock, A. P.; Shen, F.; Chang, P. L.; Wang, M.; Childs, R. F. *J. Biomater. Sci., Polym. Ed.* **2005**, *16*, 611−625.
(31) Schlupp, P.; Blaschke, T.; Kramer, K. D.; Höltje, H. D.; Mehnert, W.; Schäfer-Korting, M. *Skin Pharmacol. Physiol.* **2011**, *24*, 199−209.
(32) Teichmann, A.; Jacobi, U.; Weigmann, H.-J.; Sterry, W.; Lademann, J. *Skin Pharmacol. Physiol.* **2005**, *18*, 75−80.
(33) Hermann, P.; Hoehl, A.; Patoka, P.; Huth, F.; Rühl, E.; Ulm, G. *Opt. Express* **2013**, *21*, 2913−2919.
(34) Hermann, P.; Hoehl, A.; Ulrich, G.; Fleischmann, C.; Hermelink, A.; Kästner, B.; Patoka, P.; Hornemann, A.; Beckhoff, B.; Rühl, E.; Ulm, G. *Opt. Express* **2014**, *22*, 17948−17958.
(35) Ohigashi, T.; Arai, H.; Inagaki, Y.; Kondo, N.; Sakai, M.; Hayashi, K.; Shigemasa, E.; Hitchcock, A.; Kosugi, N.; Katoh, M. *UVSOR Activity Report 2012*; Institute for Molecular Science: Okazaki, Japan, 2013; p 43.
(36) Ohigashi, T.; Arai, H.; Araki, T.; Kondo, N.; Shigemasa, E.; Ito, A.; Kosugi, N.; Katoh, M. *J. Phys.: Conf. Ser.* **2013**, *463*, 012006 (4 pages).
(37) Hitchcock, A. P.; Mancini, D. C. *J. Electron Spectrosc. Relat. Phenom.* **1994**, *67*, 1−132.
(38) Kosugi, N.; Kuroda, H. *Chem. Phys. Lett.* **1980**, *74*, 490−493.
(39) Kosugi, N. *Theor. Chim. Acta* **1987**, *72*, 149−173.
(40) Huzinaga, S.; Andzelm, J.; Klobukowski, M.; Radzio-Andzelm, E.; Sakai, Y.; Tatewaki, H. In *Gaussian Basis Sets for Molecular Calculations*; Elsevier: Amsterdam, 1984.
(41) Kaufmann, K.; Nager, C.; Jungen, M. *Chem. Phys.* **1985**, *95*, 385−390.
(42) Hitchcock, A. P.; Brion, C. E. *J. Electron Spectrosc. Relat. Phenom.* **1980**, *19*, 231−250.
(43) Wight, G. R.; Brion, C. E. *J. Electron Spectrosc. Relat. Phenom.* **1974**, *4*, 25−42.
(44) Ishii, I.; Hitchcock, A. P. *J. Electron Spectrosc. Relat. Phenom.* **1988**, *46*, 55−84.
(45) Fancis, J. T.; Hitchcock, A. P. *J. Phys. Chem.* **1992**, *96*, 6598−6610.
(46) Geiger, J.; Rabe, S.; Heinzel, C.; Haumgärtel, H.; Rühl, E. In *Linking the Gaseous and Condensed Phases of Matter*; Christophorou, L., Illenberger, E., Schmidt, W., Eds.; Plenum: New York, 1994; pp 217−222.
(47) Zbytovska, J.; Vavrova, K.; Kiselev, M. A.; Lessieur, P.; Wartewig, S.; Neubert, R. H. H. *Colloids Surf., A* **2009**, *351*, 30−37.
(48) McGrath, L. M.; Parnas, R. S.; King, S. H.; Schroeder, J. L.; Fischer, D. A.; Lenhart, J. L. *Polymer* **2008**, *49*, 999−1014.
(49) Pelchryzim, R.; Weigmann, H. J.; Schaefer, H.; Hagemeister, T.; Linscheid, M.; Shah, V. P.; Sterry, W.; Lademann, J. *JDDG* **2004**, *11*, 914−919.
(50) Feldmann, R. J.; Maibach, H. I. *J. Invest. Dermatol.* **1969**, *52*, 89−94.
(51) Michaels, A. S.; Chandrasekaran, S. K.; Shaw, J. E. *AIChE J.* **1975**, *21*, 985−996.

DOI: 10.1021/acs.analchem.5b00800
Anal. Chem. 2015, 87, 6173−6179

3.2 Core-multishell nanocarriers: Transport and release of dexamethasone probed by soft X-ray spectromicroscopy

Author:

K. Yamamoto, A. Klossek, R. Flesch, T. Ohigashi, E. Fleige, F. Rancan, J. Frombach, A. Vogt, U. Blume-Peytavi, P. Schrade, S. Bachmann, R. Haag, S. Hedtrich, M. Schäfer-Korting, N. Kosugi, E. Rühl

Publication:

Journal of Controlled Release

Publisher:

Elsevier

Date:

28 November 2016

Volume 242, 28 November 2016, Pages 64-70

Online available at: https://doi.org/10.1016/j.jconrel.2016.08.028

Author contribution: In this work the author contributed to planning of the experiment, measurements, evaluating and interpreting the results, and wrote parts of the publication.

Journal of Controlled Release 242 (2016) 64–70

Contents lists available at ScienceDirect

Journal of Controlled Release

journal homepage: www.elsevier.com/locate/jconrel

Core-multishell nanocarriers: Transport and release of dexamethasone probed by soft X-ray spectromicroscopy

K. Yamamoto [a], A. Klossek [a], R. Flesch [a], T. Ohigashi [b], E. Fleige [c], F. Rancan [d], J. Frombach [d], A. Vogt [d], U. Blume-Peytavi [d], P. Schrade [e], S. Bachmann [e], R. Haag [c], S. Hedtrich [f], M. Schäfer-Korting [f], N. Kosugi [b], E. Rühl [a,*]

[a] Physikalische Chemie, Freie Universität Berlin, Takustr. 3, 14195 Berlin, Germany
[b] UVSOR Synchrotron Facility, Institute for Molecular Science, Okazaki 444-8585, Japan
[c] Institut für Chemie und Biochemie, Freie Universität Berlin, Takustr. 3, 14195 Berlin, Germany
[d] Klinisches Forschungszentrum für Haut- und Haarforschung, Charité Universitätsmedizin Berlin, Charitéplatz 1, 10117 Berlin, Germany
[e] Abteilung für Elektronenmikroskopie at CVK, 13353 Berlin, Germany
[f] Institut für Pharmazie, Freie Universität Berlin, Königin-Luise-Str. 2–4, 14195 Berlin, Germany

ARTICLE INFO

Article history:
Received 23 May 2016
Received in revised form 16 August 2016
Accepted 23 August 2016
Available online 24 August 2016

Keywords:
Drug delivery
Core-multishell nanocarriers
X-ray microscopy
Human skin

ABSTRACT

Label-free detection of core-multishell (CMS) nanocarriers and the anti-inflammatory drug dexamethasone is reported. Selective excitation by tunable soft X-rays in the O 1s-regime is used for probing either the CMS nanocarrier or the drug. Furthermore, the drug loading efficiency into CMS nanocarriers is determined by X-ray spectroscopy. The drug-loaded nanocarriers were topically applied to human skin explants providing insights into the penetration and drug release processes. It is shown that the core-multishell nanocarriers remain in the stratum corneum when applied for 100 min to 1000 min. Dexamethasone, if applied topically to human ex vivo skin explants using different formulations, shows a vehicle-dependent penetration behavior. Highest local drug concentrations are found in the stratum corneum as well as in the viable epidermis. If the drug is loaded to core-multishell nanocarriers, the concentration of the free drug is low in the stratum corneum and is enhanced in the viable epidermis as compared to other drug formulations. The present results provide insights into the penetration of drug nanocarriers as well as the mechanisms of controlled drug release from CMS nanocarriers in human skin. They are also compared to related work using dye-labeled nanocarriers and dyes that were used as model drugs.

1. Introduction

Polymeric drug delivery systems have been successfully used to penetrate and release molecular or nanosized objects, such as drugs, in skin. The drugs can penetrate in this way to the desired location by transdermal and follicular routes, respectively [1–5]. The dimensions of polymeric drug delivery systems are typically between 1 and 100 nm, so that they can penetrate biological matter, but also the use of larger particles has been reported before [6]. Polymer drug delivery systems are advantageously applied, especially if the drugs are difficult to formulate, e.g. hydrophobic drugs to be transported into aqueous media [7,8]. Also, hydrophilic agents can be transported by drug delivery systems [9]. Various nanoscopic drug carrier architectures have been applied reaching from dendritic structures [3,10,11], nanogels [12,13] to multilayer nanocapsules [14]. Especially, nanogels are known for triggered drug release [12,13].

For mechanistic studies on polymeric drug delivery systems often model drugs are used, such as dyes [15]. These are sensitively probed by fluorescence microscopy, permitting to derive precise information on the penetration properties in cells or tissue [16,17]. Typically dyes, such as Nile Red or Rhodamine B, which have a similar molecular weight as drugs, have been used for dermal drug delivery studies [15,17,18]. There, it is of interest to understand the penetration properties of drugs in intact and barrier-damaged skin [16]. An alternative to fluorescence labels are spin labels, which have been used for studying drug delivery along with electron paramagnetic resonance (EPR) spectroscopy [19–21]. Furthermore, the biocompatibility of such systems has been investigated [22].

Inflammatory skin diseases have been topically treated by using nanoscopic drug delivery systems [23,24]. Lesions in inflammatory skin diseases, such as psoriasis or atopic dermatitis, lower the skin barrier and enhance penetration of topically applied drugs. Model studies in this field also include mechanical removal of the skin barrier by tape-stripping [16,25].

It has been shown before that polymeric drug delivery systems, which are dye-labeled, remain essentially in the intact stratum

* Corresponding author.
E-mail address: ruehl@zedat.fu-berlin.de (E. Rühl).

http://dx.doi.org/10.1016/j.jconrel.2016.08.028
0168-3659/

corneum, the top horny layer of skin, whereas the model drugs penetrate into deeper skin layers, i.e. the viable epidermis and the dermis [16]. These studies provided clear insights into the key role that polymeric drug delivery systems play in topical drug delivery processes. However, these investigations relied essentially on fluorescence probing, where it is not clear, if the same results can be derived from label-free approaches involving neat drug nanocarriers and drugs. To date, there is limited information from label-free approaches for probing nanoscopic drug delivery systems as well as the drug following topical drug delivery besides Raman approaches [26,27]. In the past, skin samples have been investigated by spontaneous and stimulated Raman scattering (SRS) as well as coherent anti-Stokes Raman scattering (CARS) [28–31]. The advanced Raman techniques show enhanced sensitivity compared to spontaneous Raman scattering. However, the spatial resolution is diffraction limited, which is significantly lower than in X-ray microscopy, which is used in this study. An alternative Raman technique for ultimate spatial resolution provides tip-enhanced Raman spectroscopy [32], which combines the advantages of Raman microscopy with atomic force microscopy. This approach has not been used for skin research to the best of our knowledge.

The motivation for the present work is to extend the scope of label-free spectromicroscopy to be applied to probe drug-loaded polymer nanocarriers and their penetration in human skin. We have developed recently a quantitative and spatially resolved detection scheme that is based on X-ray microscopy [33], which allowed us to probe dexamethasone in fixed human skin without the need of any label. Recently, more systematic work was performed, indicating that drug penetration in human skin over time can be followed as a function of exposure time by X-ray microscopy [34]. The importance of the skin barriers for drug penetration was highlighted, as well. In this work we extend the scope for probing label-free polymeric drug nanocarriers, as well as drugs. We use core-multishell (CMS) nanocarriers, a well established drug nanocarrier system, which was extensively studied in skin along with fluorescent dyes or spin probes [15–17,19,35]. It is aimed in this work to derive quantitative information on drug loading of nanocarriers, drug penetration profiles, and if there are different penetration routes of nanocarriers and the transported drug dexamethasone, as compared to other drug formulations.

2. Materials and methods

2.1. Skin samples

Human skin samples were prepared similar to previous work [33]. Briefly, excised human abdominal skin from healthy donors undergoing plastic surgery was used. The study was approved by the Ethics Committee of the Charité – Universitätsmedizin Berlin and conducted in accordance with the Declaration of Helsinki guidelines (approval EA/1/135/06 updated 07.2015). Surplus material from plastic surgery was obtained from patients who signed the consent. The skin samples were incubated in a humidified chamber for 10 min at 32 °C before the exposure to the following formulations, which included (i) dexamethasone incorporated in hydroxyethyl cellulose (HEC) gel with a drug concentration of 0.5% (drug applied to skin: 177 μg/cm^2) and (ii) dexamethasone-loaded core-multishell (CMS) nanocarriers in HEC gel (CMS concentration in HEC gel: 0.025%, drug applied to skin: 177 μg/cm^2). These skin samples were exposed to the drug formulations for 100 min and 1000 min, respectively. Control samples were treated in the same way with neat HEC gel. For a comparison we used 0.5% dexamethasone dissolved in ethanol (applied drug: 100 μg/cm^2, as taken from ref. [33], exposure time: 240 min). Subsequently, the skin surface was cleaned from non-penetrated drug formulation and the tissue was cut into 1 × 1 mm^2 pieces which were fixed using 2.5% glutaraldehyde [33] and post-fixed by 1% OsO_4, 0.8% $K_4[Fe(CN)_6]$ both in 0.1 M cacodylate buffer. This was followed by dehydration with an increasing fraction of ethanol. The samples were subsequently embedded in epoxy resin EPON (Electron Microscopy Sciences, Kit 812). Regions of interest were cut into vertical sections of 350 nm thickness by means of a microtome RM2065 (Leica). The sample thickness is of crucial importance, since the detection scheme relies on X-ray absorption. The X-ray absorption cross section of the samples under study requires to optimize the thickness (typically 350 nm) of the samples and was controlled by atomic force microscopy (AFM) similar to previous work [33].

2.2. Preparation of CMS nanocarriers

Analytical grade solvents and chemicals were purchased from Sigma Aldrich (Steinheim, Germany) and used as received. Methoxy poly(ethylene glycol) with a molecular weight of 350 g/mol (mPEG350) was purchased from Acros Organics (Geel, Belgium). The dendritic CMS nanocarriers were synthesized as described in the literature [7]. It is known that the size of isolated core-multishell (CMS) nanocarriers is around 10 nm, at higher concentrations the formation of bigger aggregates was observed. The molecular weight ranges typically between 60,000 and 80,000 g/mol [35,36]. Drug loading of the CMS nanocarriers was accomplished as follows: In a screw-cap vial 11.3 mg CMS nanocarriers and 2.0 mg dexamethasone were dissolved in 200 μL ethanol. The ethanol was removed by a rotary evaporator and by additionally drying over night at 60 °C in a drying oven. 2.26 mL of Milli-Q water (Millipore) was added on top of the guest thin film. The resulting sample had a CMS particle concentration of 5 mg/mL. The sample was stirred at 1200 rpm for 24 h. Subsequently, the sample was filtered through 0.45 μm regenerated cellulose syringe filters to remove any unsolubilized guest.

2.3. Scanning transmission X-ray microscopy (STXM)

X-ray spectroscopy is used to selectively probe both dexamethasone and core-multishell nanocarriers. The procedure for probing selectively and quantitatively dexamethasone has been described before [33]. Briefly, the experiments were performed at the UVSOR III synchrotron radiation facility (Institute for Molecular Science, Okazaki, Japan) using the BL4U beam line where a scanning transmission X-ray microscope is operated (Bruker). The experiments were performed in the regime of the oxygen 1s-excitation (520 eV–570 eV). Selective probing of the drug and drug nanocarriers was accomplished by tuning the excitation wavelength to the O 1s → π*-resonances of the species under study. These are slightly shifted in energy, so that dexamethasone and core-multishell nanocarriers can be distinguished from each other, even if they are contained with low concentration in fixed human skin samples. Identification of CMS nanocarriers in fixed skin required slightly different photon energies (531.4 eV and 535.9 eV), as is outlined in the following.

3. Results and discussion

Fig. 1(a) shows schematically the molecular structure of dendritic core-multishell nanocarriers (cf. [7,35]). Fig. 1(b) shows the structure of dexamethasone. Selective probing of these core-multishell nanocarriers is accomplished by measuring the inner-shell absorption spectrum near the O 1s-edge of the neat drug nanocarriers, as shown in Fig. 2(a).

It is compared to the X-ray absorption of dexamethasone depicted in Fig. 2(b). The O 1s-absorption of core-multishell nanocarriers is rationalized by different oxygen sites. These are in the dendritic core ether and hydroxyl groups. In the hydrophilic shell there are also ether groups. These saturated functional groups contribute mostly to the O 1s → σ*-transitions, which are found in the O 1s-continuum around 538 eV [37]. Finally, in the nonpolar shell one finds unsaturated oxygen sites belonging to amide and carboxyl groups. The latter species give rise to the distinct resonance in the pre-edge regime, i.e. at 532.1 eV, which is assigned to the O 1s → π*-resonance. It is higher in energy

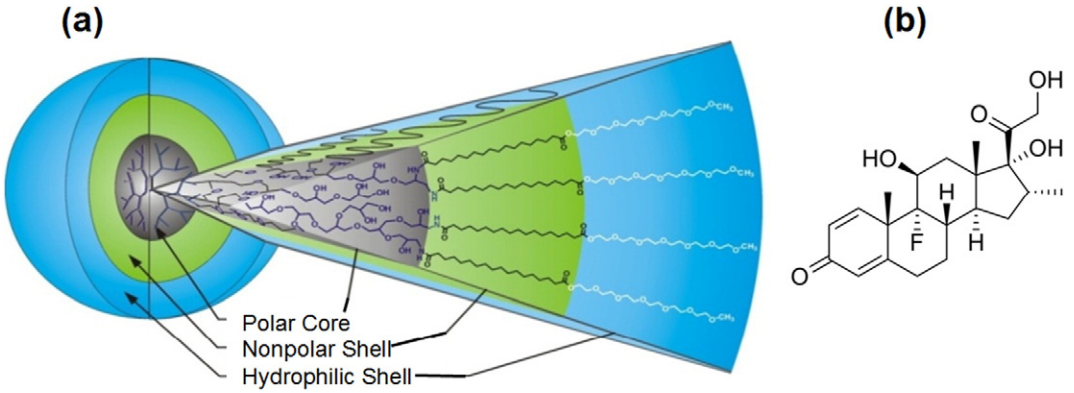

Fig. 1. Schematic diagram of (a) core-multishell (CMS) nanocarriers (as adapted from ref. [35]) and (b) structure of dexamethasone.

than the corresponding band in dexamethasone peaking at 530.8 eV (see Fig. 2(b)), which is due a chemical shift reflecting the local surroundings of the carbonyl groups. We have earlier shown that this band contains in dexamethasone two different transitions, which are not resolved [33].

The intensity of the O 1s → π*-resonance relative to the O 1s → σ*-resonance in CMS nanocarriers, occurring at 538 eV is lower than in dexamethasone, reflecting a lower fraction of unsaturated sites containing π-bonds than in the drug. These spectroscopic properties are of crucial importance for selective, label-free probing of dexamethasone and CMS nanocarriers, as it is outlined in the following. Before we discuss this issue, we first show that drug loading into CMS nanocarriers can be quantitatively determined by X-ray absorption. Fig. 2(c) shows the experimental X-ray absorption spectrum of drug-loaded nanocarriers at the O 1s-absorption edge. This is due to the substantial chemical shift of both components depicted in Fig. 2(a), (b). The open symbols in Fig. 2(c) correspond to the experimental results and the full curve is derived from a spectral de-convolution of the corresponding O 1s → π*-resonances by using Gaussian line shapes. The individual components, corresponding to the O 1s → π*-resonance of dexamethasone and CMS-nanocarriers are shown in Fig. 2(d).

Quantitative evaluation of the drug loading of dexamethasone by CMS nanocarriers is derived from these results as follows: A Gaussian profile is used to simulate the shoulder around 530.8 eV, and an exponentially modified Gaussian for the peak centered at 532.1 eV. This choice is due to the apparent asymmetry of this peak. The areas under the fit functions are required for determining the loading of dexamethasone in the nanocarrier sample. We find a ratio of 0.10 ± 40% for the areas under the peak functions. The substantial relative error limit comes mainly from the small Gaussian peak, which accounts for 37%

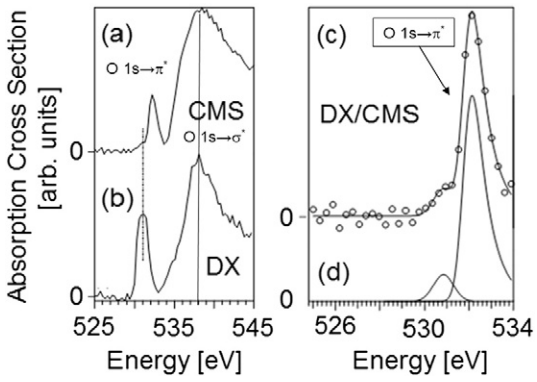

Fig. 2. Oxygen 1s-absorption spectra of (a) core-multishell nanocarriers (CMS); (b) dexamethasone (DX); (c) dexamethasone-loaded CMS nanocarriers (DX/CMS); (d) spectral de-convolution of (c). The vertical dashed line on the left hand side indicates the O 1s → π*-transition of dexamethasone.

of the overall uncertainty. This is essentially due to the considerable noise of the baseline of Fig. 2(c). The intensity ratio of both resonances is the key quantity for determining the drug loading of CMS nanocarriers. For this we need to consider the stoichiometry of the hydrocarbon chain of the CMS nanocarriers, which contain the spectroscopically probed C=O bonds. This is determined by elemental analysis, as compiled in Table 1.

The structure and elemental composition of CMS particles has been reported earlier [7,35,36]. Essentially, the CMS particles contain twice as many oxygen atoms bound in C=O bonds, belonging to amide and carboxyl groups, compared to nitrogen atoms. Taking the values from elemental analysis, shown in Table 1, one derives that the particles contain ~1.7 atom-% bound in C=O-bonds; the remaining ~8.5 atom-% oxygen is due to saturated oxygen atoms, i.e. mostly hydroxyl and ether groups.

Dexamethasone contains two C=O-sites per molecule. Taking its molecular mass of M = 392,47 g/mol one derives that there are 3.5 atom-% C=O-sites in this drug. This implies that a given mass of dexamethasone contains twice as much C=O-bonds as the same mass amount of CMS nanocarriers.

In the following it is assumed that the photoabsorption cross section of oxygen sites bound to C=O-bonds in different compounds, does not change significantly. This is in accordance to earlier results on the oscillator strength derived for various carbonyl compounds [38]. Then, the experimental signal of the O 1s → π*-resonance of dexamethasone should be twice as intense as that of CMS nanocarriers, since it contains twice as many C=O-sites. As a result, the intensity ratio between both resonances is twice as high as the mass ratio. Taking the experimental ratio of the Gaussians derived from spectral de-convolution (cf. Fig. 2(d)), which yields a ratio of 0.1 for the O 1s → π*-resonance of dexamethasone to CMS nanocarriers, one derives a drug load of 5%. This value is consistent with results derived from solubilization experiments probed by optical spectroscopy [39]. The approach for determining drug loading by inner-shell spectroscopy presented in this work is novel and allows us to analyze the samples under study using X-ray spectromicroscopy.

Once the drug nanocarriers are spectroscopically characterized regarding their drug load, they are investigated in human skin ex vivo by X-ray microscopy. Fig. 3 shows the O 1s-regimes of CMS nanocarriers and fixed human skin. Both O 1s → π*-resonances are not shifted in

Table 1
Elemental analysis of CMS nanocarriers.

Atom	Mass-%	Atom-%
N	2.054	0.9
C	60.860	30.3
H	9.805	58.6
O	27.281	10.2

energy, so that this resonance cannot be used for deriving a chemical contrast. This is unlike recent work on quantitative probing of dexamethasone in human skin [33]. However, the spectral shapes of both species are different from each other, where the O 1s → π*-resonance of fixed human skin is more intense relative to the O 1s → σ*-resonance, if compared to CMS nanocarriers (see Fig. 3). Therefore, we have chosen two photon energies, at which fixed human skin shows a similar X-ray absorption cross section, whereas that of CMS nanocarriers almost doubles due to a lower amount of C=O-bonds, providing a way for selective probing of CMS nanocarriers in fixed human skin. Specifically, we used the following photon energies: 531.4 eV and 535.9 eV. According to the Beer-Lambert law, the experimentally observed gain in differential absorption at both energies can be related to the occurrence of CMS nanocarriers in human skin. Note that for the analysis a background signal from the skin has been taken into account. This yields the result that CMS nanocarriers are only found in the stratum corneum, but neither in the viable epidermis nor in the dermis (cf. Fig. 4). This is in accordance with earlier studies using dye-labeled CMS nanocarriers, which were investigated by fluorescence microscopy [16].

Results from X-ray microscopy are shown in Fig. 4. Fig. 4(a) shows the image of the reference sample (neat HEC gel, 100 min penetration time), where the differential absorption is on the average 0.20 ± 0.02 in the lipid structures and in the corneocytes 0.15 ± 0.01. When the sample is exposed for 100 min to CMS nanocarriers, one derives Fig. 4(b). There, the average differential absorption remains for corneocytes at 0.15 ± 0.01, but increases for the lipid structures to 0.22 ± 0.02. At single locations the differential absorption exceeds 0.28, which is visualized by single yellow dots. These are regions, in which CMS nanocarriers occur. They are located within the stratum corneum lipid lamellae between the corneocytes [40], giving rise to narrow ribbons of CMS nanocarriers, whereas in the regions in between, i.e. the corneocytes, no evidence for CMS nanocarriers is found, especially after 100 min exposure. Cross sensitivities of the detection approach can be ruled out, as visualized in Fig. 4(a). The other striking observation is the detection of individual pixels of enhanced differential absorption. These have a size of 50 nm, corresponding to the step width used for recording the images. This is unlike neat dexamethasone penetrating into the stratum corneum, which is characterized by a homogeneous distribution within the lipid lamellae of the stratum corneum [34], indicating a distinct difference in the appearance of a low molecular weight drug (dexamethasone (M = 392.5 g/mol)) and CMS drug carriers, if they are selectively probed by X-ray microscopy. This implies that dexamethasone fits into all parallel lipid lamellae, which are known to have of a width of 13 nm [41]. This situation is different for CMS nanocarriers due to their sizable diameter of ~10 nm [35,36]. The present results indicate, especially for t = 100 min, that the CMS nanocarriers do not penetrate in parallel through a single 13 nm lipid lamella, which is likely due to the low nanocarrier concentration. We have also analyzed the intensity distribution of these single yellow colored pixels and observed a remarkably similar amplitude of differential absorption at different locations of the stratum corneum. This sheds light on the question on the CMS particle density within the lipid lamellae. Assuming that within one pixel of 50 nm^2 one finds four 13 nm lipid lamellae in which at most one CMS nanocarrier is accommodated, then there can be up to 20 drug carriers of a size of ~10 nm within a slice of 10 nm, corresponding to the approximated size of a nanocarrier [42]. The thickness of the investigated skin slices is 350 nm, so that at most 700 CMS nanocarriers can be found within a single pixel, corresponding to 100% loading. The observed changes in differential absorption due to drug nanocarriers yield a loading of 12 ± 6% at t = 100 min. The error limit considers that the lipid channels show some variations of differential absorption in different lipid channels. The present results clearly indicate that no aggregates of CMS nanocarriers can penetrate into the stratum corneum, which is explained by spatial restrictions of the lipophilic lamellae and the fact that at a given location no more than two or at most three pixels show enhanced absorption due to CMS nanocarriers. This situation changes as follows after 1000 min exposure time (see Fig. 4(c)).

Firstly, there is accumulation of CMS drug nanocarriers in the lower part of the stratum corneum at t = 1000 min (see Fig. 4(c)) and there is for both exposure times no evidence for penetration of CMS

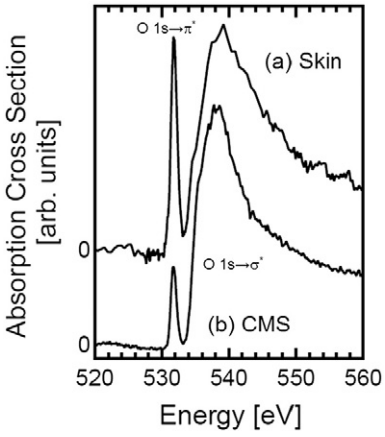

Fig. 3. O 1s-absorption spectra of (a) fixed human skin and (b) CMS nanocarriers (see text for further details).

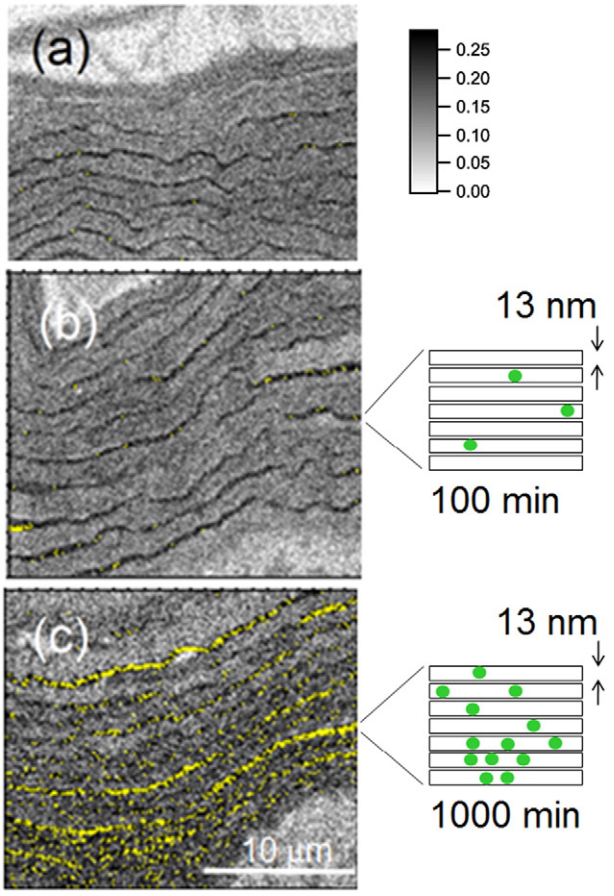

Fig. 4. High resolution X-ray micrographs of the stratum corneum of human skin samples derived from differential absorption recorded at 531.4 eV and 535.9 eV, respectively. Differential absorption is represented by a gray scale, where a gain in absorption corresponds to black color, which turns above a threshold value of 0.28 into yellow: Application of dexamethasone-loaded CMS nanocarriers for (a) reference sample containing only HEC gel; (b) 100 min; (c) 1000 min. The viable epidermis is located at the bottom of each micrograph. Schematic diagrams are shown in (b) and (c) symbolizing the location of the CMS nanocarriers within the 13 nm lipid lamellae.

nanocarriers into the viable epidermis. This points to the fact that there is a barrier for CMS nanocarriers which they cannot overcome. However, this barrier can be passed by the drug, as is outlined further below. The average differential absorption is increased in the lipophilic regions at 1000 min to 0.29 ± 0.02, i.e. by 45 ± 5% relative to the reference sample. Here, several drug carriers appear at the same position of the stratum corneum, indicating that at increased concentration, CMS nanocarriers can penetrate in parallel through this region. The occurrence of the drug carriers, which is significantly slower than the neat drug, points to a slow CMS penetration process. Secondly, CMS nanocarriers appeared more spread into the regions where corneocytes are located at t = 1000 min, especially in the lower part of the stratum corneum (cf. Fig. 4(c)). We assume that it is unlikely that an ~10 nm nanocarrier will penetrate into a region, which cannot be accessed by the drug nanocarrier and the neat drug (cf. ref. [33,34]). It rather appears to be plausible that this observation is due to a decay of the CMS nanocarriers in the lower part of the stratum corneum, most likely via cleavage induced by enzymes, such as lipases and esterases [43–45]. Therefore, nonpolar moieties of lower molecular weight will be released and probed by X-ray absorption. These species are more likely to penetrate into the corneocytes than entire CMS nanocarriers. At the same time one expects that this decay process is accompanied by a release of the loaded drug. We also assume that the drug is stably associated with the CMS nanocarriers during the penetration of the stratum corneum and it is released once the nanocarriers are degraded. This assumption is further proved by drug penetration profiles shown in Fig. 5.

Fig. 5(a)–(c) shows a comparison of drug penetration profiles obtained from different formulations of dexamethasone that is topically applied to the skin. Note that the uncertainty in local drug concentration is estimated to be of the order of 10%, substantial variations in this quantity occur due to the heterogeneity of the skin samples. Fig. 5(a) corresponds to four hours exposure to an ethanolic dexamethasone solution (ethanol:water: 90:10; drug concentration: 0.5%) (cf. ref. [33]). A distinct maximum in local dexamethasone concentration of 4 μg/(cm^2·μm) is observed in the stratum corneum. A distinct drop in local concentration is observed in the region between the stratum corneum and the viable epidermis. Such minimum in local drug concentration has also been observed for other formulations and exposure times [34]. This indicates the occurrence of another barrier at the transition between both epidermal layers and has been assigned as the region of the tight junction barrier in the stratum granulosum, which efficiently hinders the inside-out transport of voluminous solutes [46], and may influence the drug penetration into lower skin layers, as well. Compared to the stratum corneum, the local drug concentration within the viable epidermis is significantly lower reaching about 1.5 μg/(cm^2·μm) and no dexamethasone is detected in the dermis. There is a characteristic drop in drug concentration in the region of the basal cells, which has been recognized before [34]. The stratum basale and/or the basal membrane separating epidermis and dermis represent another barrier before the drug gains access to the vascularized dermis, which may result in systemic availability [34]. Fig. 5(b) shows for a comparison the drug penetration after 16 h of topical application of HEC gel containing dexamethasone. Similarly, the local drug concentration peaks in the stratum corneum, but with smaller amplitude (3 μg/(cm^2·μm)), whereas the concentration in the viable epidermis is enhanced reaching values up to 2 μg/(cm^2·μm). There are also the characteristic drops in local drug concentration between the stratum corneum and the viable epidermis as well as near the basal membrane. These occur at slightly different depths, due to the variability in thickness of the different skin layers in the skin samples under study. This implies that dexamethasone has penetrated into deeper regions, if the exposure time is increased from 4 h to 16 h. Fig. 5(c) shows the concentration profile of dexamethasone released from CMS nanocarriers at 16 h. This profile is unique, since it does not show a maximum in the stratum corneum, rather than in the viable epidermis. In the stratum corneum one observes only a moderate free dexamethasone concentration of about 1 μg/(cm^2·μm), whereas in the viable epidermis the local drug concentration reaches up to 3 μg/(cm^2·μm). This result is consistent with earlier findings observed for the detection of CMS nanocarriers [16] and provides specific information on the drug release mechanism from CMS nanocarriers. Evidently, the drug-loaded CMS nanocarriers translocate into the stratum corneum without massive drug loss. Otherwise one would observe high drug concentrations in this top skin layer, similar to topical application of the dissolved drug and the HEC gel. In accordance with the appearance of the degraded nanocarriers in the corneocytes after 1000 min, the nanocarriers appear to release the drug rather in the lower region of the stratum corneum and do not gain access to viable skin layers. Free dexamethasone, however, surmounts the tight junction barrier of the stratum granulosum and penetrates into the viable epidermis. There, it can accumulate due to slow penetration via the barrier provided by the basal cell layer and the basal membrane. Therefore, we also see in Fig. 5(c) a steep drop in dexamethasone concentration, as observed for the dissolved and HEC-formulated drug (see Fig. 5(a), (b)). Consistently, we also do not observe increased dexamethasone concentration in the dermis (DE). The results are summarized in Fig. 5(d) and (e), where the partitioning of dexamethasone in the stratum corneum and viable epidermis is deduced from the results depicted in Fig. 5(a)–(c). There, the integrated relative amount of the drug in each of these skin layers is shown on a relative scale. In the case of the ethanol solution (4 h exposure time) one observes that 71 ± 23% of the topically applied drug are found within the skin (indicated by red bars), of which a fraction of 33 ± 15% is found in the stratum corneum and 38 ± 17% are spread over the viable epidermis. Note that these error limits are essentially due to the heterogeneity of the skin samples. This leads to substantial error limits, as indicated in Fig. 5(d)–(e). As a result, one does not find significant differences, if the entire skin layers are compared to each other. However, if parts of the stratum corneum are compared to each

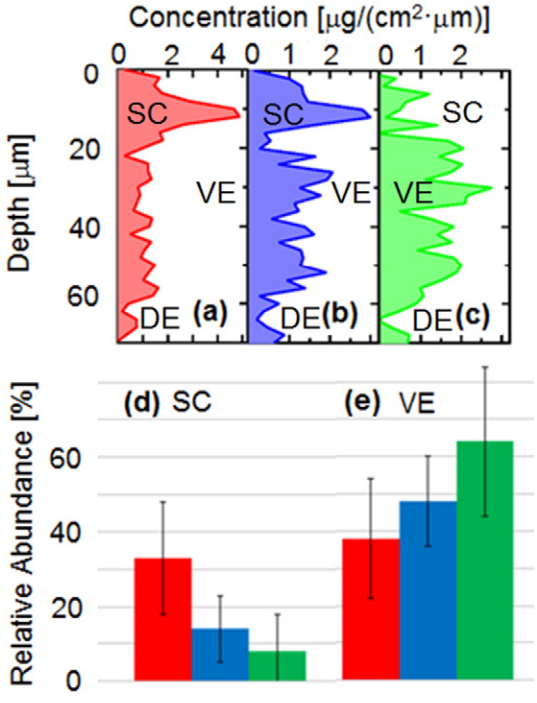

Fig. 5. Penetration profiles of dexamethasone in human skin ex vivo: (a) 4 h exposure to dexamethasone dissolved in ethanol (cf. ref. [33]); (b) 16 h exposure to dexamethasone in HEC gel; (c) free dexamethasone released from CMS nanocarriers after 16 h exposure time; (d) relative abundance of dexamethasone in the stratum corneum (SC); (e) relative abundance of dexamethasone in the viable epidermis (VE). No dexamethasone is found in the dermis (DE). The colors in (d) and (e) correspond to the different drug formulations shown in (a)–(c).

other, it is significant, that this layer is not used as a drug reservoir, if drug-loaded CMS-nanocarriers are applied, as compared to the other drug formulations. For the HEC gel formulated drug that was applied for 16 h (indicated by blue bars) one derives that only 14 ± 9% of dexamethasone are found in the stratum corneum and 48 ± 12% are located in the viable epidermis, yielding as a sum 62 ± 15% uptake into both skin layers, which is similar to the ethanolic solution applied for 4 h. Evidently dexamethasone is efficiently penetrating the viable epidermis with increasing exposure time. The situation is different for the use of CMS nanocarriers (green bars), where only 8 ± 10% of the drug are found in the stratum corneum and the overwhelming fraction of 63 ± 18% is observed in the viable epidermis. Note that the sum of both fractions is similar to the other formulations. The role of CMS nanocarriers, transporting the highly skin penetrating drug dexamethasone, becomes evident for these results. The stratum corneum cannot act as a drug reservoir, so that the drug is more efficiently penetrating into the viable epidermis.

Finally, we address the question whether label-free detection provides further insights into drug penetration compared to studies relying on dye-labeled CMS nanocarriers and dyes used as model drugs [7,9,16]. The result that CMS nanocarriers remain in the stratum corneum is fully consistent with the present work. However, the penetration of dyes, used as model drugs, appears to be observable in deeper skin layers than dexamethasone, where in the dermis a sizable amount of model drug was found. This is ascribed to different penetration properties of dyes compared to dexamethasone. Evidence for this conclusion comes from a comparison of intact and tape-stripped skin (cf. ref. [16]), where significantly enhanced dye-penetration into the dermis is observed for tape-stripped skin. This is unlike recent results on the penetration of dexamethasone in similarly prepared skin samples probed by X-ray microscopy, where no drug was found in the dermis [33,34]. This discrepancy cannot be explained by differences in sensitivity between both experimental approaches, rather than by different penetration properties of the respective dyes and drugs in skin. This highlights the need for label-free detections schemes providing high spatial resolution in the nanometer regime. Consistently, X-ray microscopy also provides rich details due to its superior spatial resolution compared to standard fluorescence microscopy approaches.

4. Conclusions

Label-free soft X-ray spectromicroscopy has the advantage that it does not require to label neither the drug delivery systems nor the drug for investigating skin penetration. This issue is less severe for drug delivery systems as heavy moieties of >50,000 g/mol, which are expected not to change their penetration properties in human skin upon labeling. Especially fluorescence- or EPR-labels, however, can change significantly the mass and chemical properties of low molecular weight drugs, which may affect their penetration properties. Specifically, we have shown by X-ray microscopy and the use of its high resolution capability, reaching nanoscopic dimensions, that the CMS nanocarriers remain in the stratum corneum upon topical application, even after 1000 min exposure. There is, however, evidence for a decay of the CMS nanocarriers in the lower stratum corneum. Dexamethasone shows different penetration properties, if released from CMS nanocarriers or conventional vehicles. We found evidence for drug release from CMS nanocarriers in the stratum corneum, which is clearly distinguished from topical delivery of dexamethasone using either the dissolved or HEC-gel formulated drug. In addition, X-ray spectromicroscopy is not only able to probe drug and nanocarrier penetration routes quantitatively, but also the drug loading of the polymeric nanocarriers. We observed for the present sample that the CMS nanocarriers were loaded with 5% dexamethasone. High spatial resolution provided by X-ray microscopy was used to derive further information on the penetration processes of CMS nanocarriers through the stratum corneum, providing evidence that no aggregates of CMS nanocarriers are penetrating into this skin layer. Finally, we note that X-ray microscopy is complimentary to Raman microscopy techniques. Both are label-free approaches, whereas the spatial resolution and the sensitivity of X-ray microscopy is shown to be superior.

Acknowledgments

Financial support by German Research Foundation (DFG) within SFB 1112 is gratefully acknowledged. Support of this work by the Helmholtz-Zentrum Berlin, Institute for Molecular Science, and Freie Universität Berlin is gratefully acknowledged.

References

[1] R. Alvarez-Roman, A. Naik, Y. Kalia, R.H. Guy, H. Fessi, Skin penetration and distribution of polymeric nanoparticles, J. Control. Release 99 (2004) 53–62.
[2] C. Pegoraro, S. MacNeil, G. Battaglia, Transdermal drug delivery: from micro to nano, Nanoscale 4 (2012) 1881–1894.
[3] I.N. Kurniasih, J. Keilitz, R. Haag, Dendritic nanocarriers based on hyperbranched polymers, Chem. Soc. Rev. 44 (2015) 4145–4164.
[4] A.S. Hoffman, The origins and evolution of "controlled" drug delivery systems, J. Control. Release 132 (2008) 153–163.
[5] M.J. Santander-Ortega, T. Stauner, B. Loretz, J.L. Ortega-Vinuesa, D. Bastos-Gonzalez, G. Wenz, U.F. Schaefer, C.M. Lehr, Nanoparticles made from novel starch derivatives for transdermal drug delivery, J. Control. Release 141 (2010) 85–92.
[6] V.C. Lopez, J. Hadgraft, M.J. Snowden, The use of colloidal microgels as a (trans)dermal drug delivery system, Int. J. Pharm. 292 (2005) 137–147.
[7] S. Küchler, M.R. Radowski, T. Blaschke, M. Dathe, J. Plendl, R. Haag, M. Schäfer-Korting, K.D. Kramer, Nanoparticles for skin penetration enhancement - a comparison of a dendritic core-multishell-nanotransporter and solid lipid nanoparticles, Eur. J. Pharm. Biopharm. 71 (2009) 243–250.
[8] B.N.S. Thota, L.H. Urner, R. Haag, Supramolecular architectures of dendritic amphiphiles in water, Chem. Rev. 116 (2016) 2079–2102.
[9] S. Küchler, M. Abdel-Mottaleb, A. Lamprecht, M.R. Radowski, R. Haag, M. Schäfer-Korting, Influence of nanocarrier type and size on skin delivery of hydrophilic agents, Int. J. Pharm. 377 (2009) 169–172.
[10] S. Mignani, S. El Kazzouli, M. Bousmina, J.-P. Majoral, Expand classical drug administration ways by emerging routes using dendrimer drug delivery systems: a concise overview, Adv. Drug Deliv. Rev. 65 (2013) 1316–1330.
[11] R.M. Kannan, E. Nance, S. Kannan, D.A. Tomalia, Emerging concepts in dendrimer-based nanomedicine: from design principles to clinical applications, J. Int. Med. 276 (2014) 579–617.
[12] M. Molina, M. Asadian-Birjand, J. Balach, J. Bergueiro, E. Miceli, M. Calderon, Stimuli-responsive nanogel composites and their application in nanomedicine, Chem. Soc. Rev. 44 (2015) 6161–6186.
[13] M. Asadian-Birjand, J. Bergueiro, F. Rancan, J.C. Cuggino, R.C. Mutihac, K. Achazi, J. Dernedde, U. Blume-Peytayi, A. Vogt, M. Calderon, Engineering thermoresponsive polyether-based nanogels for temperature dependent skin penetration, Polym. Chem. 6 (2015) 5827–5831.
[14] U. Bazylinska, J. Pietkiewicz, J. Saczko, M. Nattich-Rak, J. Rossowska, A. Garbiec, K.A. Wilk, Nanoemulsion-templated multilayer nanocapsules for cyanine-type photosensitizer delivery to human breast carcinoma cells, Eur. J. Pharm. Biopharm. 47 (2012) 406–420.
[15] M.A. Quadir, M.R. Radowski, F. Kratz, K. Licha, P. Hauff, R. Haag, Dendritic multishell architectures for drug and dye transport, J. Control. Release 132 (2008) 289–294.
[16] N. Alnasif, C. Zoschke, E. Fleige, R. Brodwolf, A. Boreham, E. Rühl, K.M. Eckl, H.F. Merk, H.C. Hennies, U. Alexiev, R. Haag, S. Küchler, M. Schäfer-Korting, Penetration of normal, damaged and diseased skin - an in vitro study on dendritic core-multishell nanotransporters, J. Control. Release 185 (2014) 45–50.
[17] A. Boreham, M. Pfaff, E. Fleige, R. Haag, U. Alexiev, Nanodynamics of dendritic core-multishell nanocarriers, Langmuir 30 (2014) 1686–1695.
[18] F. Rancan, M. Asadian-Birjand, S. Dogan, C. Graf, L. Cuellar, S. Lommatzsch, U. Blume-Peytavi, M. Calderon, A. Vogt, Effects of thermoresponsivity and softness on skin penetration and cellular uptake of polyglycerol-based nanogels, J. Control. Release 228 (2016) 159–169.
[19] S.F. Haag, E. Fleige, M. Chen, A. Fahr, C. Teutloff, R. Bittl, J. Lademann, M. Schäfer-Korting, R. Haag, M.C. Meinke, Skin penetration enhancement of core-multishell nanotransporters and invasomes measured by electron paramagnetic resonance spectroscopy, Int. J. Pharm. 416 (2011) 223–228.
[20] S. Kempe, H. Metz, K. Mäder, Application of Electron Paramagnetic Resonance (EPR) spectroscopy and imaging in drug delivery research - chances and challenges, Eur. J. Pharm. Biopharm. 74 (2010) 55–66.
[21] S. Küchler, W. Herrmann, G. Panek-Minkin, T. Blaschke, C. Zoschke, K.D. Kramer, R. Bittl, M. Schäfer-Korting, SLN for topical application in skin diseases - characterization of drug-carrier and carrier-target interactions, Int. J. Pharm. 390 (2010) 225–233.
[22] S. Kumar, N. Alnasif, E. Fleige, I. Kurniasih, V. Kral, A. Haase, A. Luch, G. Weindl, R. Haag, M. Schäfer-Korting, S. Hedtrich, Impact of structural differences in hyperbranched polyglycerol-polyethylene glycol nanoparticles on dermal drug delivery and biocompatibility, Eur. J. Pharm. Biopharm. 88 (2014) 625–634.
[23] M. Gupta, U. Agrawal, S.P. Vyas, Nanocarrier-based topical drug delivery for the treatment of skin diseases, Expert Opin. Drug Deliv. 9 (2012) 783–804.

[24] N. Parnami, T. Garg, G. Rath, A.K. Goyal, Development and characterization of nanocarriers for topical treatment of psoriasis by using combination therapy, Art. Cells Nanomed. Biotechnol. 42 (2014) 406–412.
[25] P.G. Ortiz, S.H. Hansen, V.P. Shah, T. Menne, E. Benfeldt, Impact of adult atopic dermatitis on topical drug penetration: assessment by cutaneous microdialysis and tape stripping, Acta Derm. Venereol. 89 (2009) 33–38.
[26] W.S. Chiu, N.A. Belsey, N.L. Garrett, J. Moger, G.J. Price, M.B. Delgado-Charro, R.H. Guy, Drug delivery into microneedle-porated nails from nanoparticle reservoirs, J. Control. Release 220 (2015) 98–106.
[27] N.A. Belsey, N.L. Garrett, L.R. Contreras-Rojas, A.J. Pickup-Gerlaugh, G.J. Price, J. Moger, R.H. Guy, Evaluation of drug delivery to intact and porated skin by coherent Raman scattering and fluorescence microscopies, J. Control. Release 174 (2014) 37–42.
[28] C.W. Freudiger, M.B.J. Roeffaers, X. Zhang, B.G. Saar, W. Min, X.S. Xie, Optical heterodyne-detected Raman-induced Kerr effect (OHD-RIKE) microscopy, J. Phys. Chem. B 115 (2011) 5574–5581.
[29] I.W. Schie, C. Krafft, J. Popp, Applications of coherent Raman scattering microscopies to clinical and biological studies, Analyst 140 (2015) 3897–3909.
[30] C. Freudiger, W. Min, B. Saar, S. Lu, G. Holtom, C. He, J. Tsai, J. Kang, X. Xie, Label-free biomedical imaging with high sensitivity by stimulated Raman scattering microscopy, Science 322 (2008) 1857–1861.
[31] Y. Pyatski, Q.H. Zhang, R. Mendelsohn, C.R. Flach, Effects of permeation enhancers on flufenamic acid delivery in ex vivo human skin by confocal Raman microscopy, Int. J. Pharm. 505 (2016) 319–328.
[32] E.V. Efremov, F. Ariese, C. Gooijer, Achievements in resonance Raman spectroscopy review of a technique with a distinct analytical chemistry potential, Anal. Chim. Acta 606 (2008) 119–134.
[33] K. Yamamoto, R. Flesch, T. Ohigashi, S. Hedtrich, A. Klossek, P. Patoka, G. Ulrich, S. Ahlberg, F. Rancan, A. Vogt, U. Blume-Peytavi, P. Schrade, S. Bachmann, M. Schäfer-Korting, N. Kosugi, E. Rühl, Selective probing of the penetration of dexamethasone into human skin by soft X-ray spectromicroscopy, Anal. Chem. 87 (2015) 6173–6179.
[34] K. Yamamoto, A. Klossek, R. Flesch, F. Rancan, M. Weigand, I. Bykova, M. Bechtel, S. Ahlberg, A. Vogt, U. Blume-Peytavi, P. Schrade, S. Bachmann, S. Hedtrich, M. Schäfer-Korting, E. Rühl, Influence of the skin barrier on the penetration of topically-applied dexamethasone probed by soft X-ray spectromicroscopy, Eur. J. Pharm. Biopharm. (2016) (submitted).
[35] E. Fleige, B. Ziem, M. Grabolle, R. Haag, U. Resch-Genger, Aggregation phenomena of host and guest upon the loading of dendritic core-multishell nanoparticles with solvatochromic dyes, Macromolecules 45 (2012) 9452–9459.
[36] C. Rabe, E. Fleige, K. Vogtt, N. Szekely, P. Lindner, W. Burchard, R. Haag, M. Ballauff, The multi-domain nanoparticle structure of a universal core-multi-shell nanocarrier, Polymer 55 (2014) 6735–6742.
[37] I. Ishii, A.P. Hitchcock, The oxcillator strengths for C1s and O1s excitation of some saturated and unsaturated organic alcohols, acids and esters, J. Electron Spectrosc. Relat. Phenom. 46 (1988) 55–84.
[38] L. Yang, H. Agren, L.G.M. Pettersson, V. Carravetta, On the initial and final state rules for predicting near-edge X-ray absorption intensities, J. Electron Spectrosc. Relat. Phenom. 83 (1997) 209–216.
[39] S. Stefani, I.N. Kurniasih, S.K. Sharma, C. Böttcher, P. Servin, R. Haag, Triglycerol-based hyperbranched polyesters with an amphiphilic branched shell as novel biodegradable drug delivery systems, Polym. Chem. 7 (2016) 887–898.
[40] M. Fartasch, I.D. Bassukas, T.L. Diepgen, Structural relationship between epidermal lipid lamellae, lamellar bodies and desmosomes in human epidermis - an ultrastructural study, Br. J. Dermatol. 128 (1993) 1–9.
[41] D. Groen, G.S. Gooris, J.A. Bouwstra, New insights into the stratum corneum lipid organization by X-ray diffraction analysis, Biophys. J. 97 (2009) 2242–2249.
[42] M.R. Radowski, A. Shukla, H. von Berlepsch, C. Böttcher, G. Pickaert, H. Rehage, R. Haag, Supramolecular aggregates of dendritic multishell architectures as universal nanocarriers, Angew. Chem. Int. Ed. 46 (2007) 1265–1269.
[43] P.W. Wertz, The nature of the epidermal barrier: biochemical aspects, Adv. Drug Deliv. Rev. 18 (1996) 283–294.
[44] F. Beisson, M. Aoubala, S. Marull, A.M. Moustacas-Gardies, R. Voultoury, R. Verger, V. Arondel, Use of the tape stripping technique for directly quantifying esterase activities in human stratum corneum, Anal. Biochem. 290 (2001) 179–185.
[45] F.M. Bätz, W. Klipper, H.C. Korting, F. Henkler, R. Landsiedel, A. Luch, U. von Fritschen, G. Weindl, M. Schäfer-Korting, Esterase activity in excised and reconstructed human skin - biotransformation of prednicarbate and the model dye fluorescein diacetate, Eur. J. Pharm. Biopharm. 84 (2013) 374–385.
[46] J.M. Brandner, Importance of tight junctions in relation to skin barrier function, Curr. Probl. Dermatol. 49 (2016) 27–37.

3.3 Influence of the skin barrier on the penetration of topically-applied dexamethasone probed by soft X-ray spectromicroscopy

Author:

K. Yamamoto, A. Klossek, R. Flesch, F. Rancan, M. Weigand, I. Bykova, M. Bechtel, S. Ahlberg, A. Vogt, U. Blume-Peytavi, P. Schrade, S. Bachmann, S. Hedtrich, M. Schäfer-Korting, E. Rühl

Publication:

European Journal of Pharmaceutics and Biopharmaceutics

Publisher:

Elsevier

Date:

September 2017

European Journal of Pharmaceutics and Biopharmaceutics, Volume 118, September 2017, Pages 30-37

Online available at: https://doi.org/10.1016/j.ejpb.2016.12.005

Author contribution: In this work the author contributed to planning of the experiment, measurements, evaluating and interpreting the results, and wrote parts of the publication.

European Journal of Pharmaceutics and Biopharmaceutics 118 (2017) 30–37

Contents lists available at ScienceDirect

European Journal of Pharmaceutics and Biopharmaceutics

journal homepage: www.elsevier.com/locate/ejpb

Research paper

Influence of the skin barrier on the penetration of topically-applied dexamethasone probed by soft X-ray spectromicroscopy

K. Yamamoto [a], A. Klossek [a], R. Flesch [a], F. Rancan [b], M. Weigand [c], I. Bykova [c], M. Bechtel [c], S. Ahlberg [b], A. Vogt [b], U. Blume-Peytavi [b], P. Schrade [d], S. Bachmann [d], S. Hedtrich [e], M. Schäfer-Korting [e], E. Rühl [a,*]

[a] Physikalische Chemie, Freie Universität Berlin, Takustr. 3, 14195 Berlin, Germany
[b] Klinisches Forschungszentrum für Haut- und Haarforschung, Charité Universitätsmedizin, Berlin, Charitéplatz 1, 10117 Berlin, Germany
[c] Max-Planck-Institut für Metallforschung, Heisenbergstraße 3, 70569 Stuttgart, Germany
[d] Abteilung für Elektronenmikroskopie at Campus Virchow Klinikum (CVK), Charité Universitätsmedizin, Augustenburger Platz 1, 13353 Berlin, Germany
[e] Institut für Pharmazie, Freie Universität Berlin, Königin-Luise-Str. 2+4, 14195 Berlin, Germany

ARTICLE INFO

Article history:
Received 1 July 2016
Revised 6 October 2016
Accepted in revised form 14 December 2016
Available online 18 December 2016

Keywords:
X-ray microscopy
Drug delivery
Drug penetration
Skin
Skin barrier

ABSTRACT

The penetration of dexamethasone into human skin *ex vivo* is reported. X-ray microscopy is used for label-free probing of the drug and quantification of the local drug concentration with a spatial resolution reaching 70 ± 5 nm. This is accomplished by selective probing the dexamethasone by X-ray absorption. Varying the penetration time between 10 min and 1000 min provides detailed information on the penetration process. In addition, the stratum corneum has been damaged by tape-stripping in order to determine the importance of this barrier regarding temporally resolved drug penetration profiles. Dexamethasone concentrations distinctly vary, especially close to the border of the stratum corneum and the viable epidermis, where a local minimum in drug concentration is observed. Furthermore, near the basal membrane the drug concentration strongly drops. High spatial resolution studies along with a de-convolution procedure reveal the spatial distribution of dexamethasone in the interspaces between the corneocytes consisting of stratum corneum lipids. These results on local drug concentrations are interpreted in terms of barriers affecting the drug penetration in human skin.

1. Introduction

Formed by anuclear corneocytes of low water content and embedded into a multilayer lipid matrix made up from phospholipids, ceramides, and cholesterol as the main components [1], the stratum corneum acts as the main barrier for topically applied drugs so that most efficiently only lipophilic and low molecular weight compounds below 500 g mol^{-1} can penetrate into viable skin layers [2]. Moreover, the stratum corneum forms a drug-specific reservoir [3]. Although this barrier is disrupted by inflammatory skin diseases, such as psoriasis [4] or atopic dermatitis [5], as well as by mechanical damage induced e.g. by tape-stripping [6], delivery of sufficient drugs amounts to the site of skin diseases is a major challenge. For enhanced drug penetration, enhancers of various types are extensively used [7]. These include ethanol, in particular improving the penetration of hydrophilic compounds [8].

There are several experimental approaches for probing the dermal drug concentration following topical drug delivery. For non-clinical studies OECD guideline 428 suggests the testing in human skin *ex vivo* mounted to Franz diffusion cells [9]. The procedure has been standardized and prevalidated [10] and the results are predictable for humans [11,12]. OECD guideline 428 allows other approaches, as well, e.g. testing on animal skin or reconstructed human skin and replacing Franz cells by transwells, provided the results are comparable to each other. Drug analytics makes use of e.g. high pressure liquid chromatography (HPLC) for the quantification of the penetration, i.e. drug amounts within the skin, and permeation, i.e. amounts which have diffused across the skin and are recovered in the receptor fluid [13–15]. The sensitivity of HPLC provides a limited spatial resolution of >20 μm, as seen e.g. for glucocorticoids [14,16–18], which are quantified after extraction from horizontal skin sections. The concentration gradient of drugs penetrating the stratum corneum and viable skin layers has been analyzed and modeled [19–21]. Transport in the stratum corneum as well as in the viable skin layers is diffusion driven, which yields an exponential drop of the drug concentration when sampling the stratum corneum by tape-stripping for analysis [22]. Also deviations in terms of biphasic depth profiles have been reported [23]. The spatial resolution of all these procedures is not sufficient to

* Corresponding author.
E-mail address: ruehl@zedat.fu-berlin.de (E. Rühl).

http://dx.doi.org/10.1016/j.ejpb.2016.12.005
0939-6411/

determine variations in local drug concentration within the stratum corneum and thus do not allow for gaining detailed insights into the processes that overcome this barrier.

The lipid matrix between the corneocytes within the stratum corneum depicts a lamellar phase with a periodicity of ~13 nm [1], which is of crucial importance for the skin barrier function. In addition, a short periodicity phase of ~6 nm has been identified [24], which is more frequent in lesional skin of atopic dermatitis. Penetration of compounds containing heavy elements, such as $HgCl_2$, through human skin has been probed by transmission electron microscopy along with energy-dispersive X-ray spectroscopy (EDX) [25] and revealed time-dependent changes in penetration. Initially, $HgCl_2$ was observed in the lipid matrix between the corneocytes and at later times some uptake into apical corneocytes was observed. However, EDX cannot be easily used for drugs containing light elements, such as dexamethasone, which is subject of this work.

Drug delivery processes are sensitively probed by fluorescence microscopy [26]. This requires a fluorescing drug, which is rare, or a fluorescing label bound to the drug of interest [27]. Often, the drugs are simply replaced by a fluorescing dye, so that the penetration processes into skin can be easily observed [28]. Recently, super-resolution fluorescence microscopy studies have been reported for elucidating the transdermal penetration of intact liposomes [29].

Label-free approaches for probing spatially resolved drugs make use of unique spectroscopic properties of the compounds to be detected, which includes mass spectrometry [30], Raman-based techniques including stimulated Raman microscopy [31,32], and coherent anti-Stokes Raman scattering [33]. More recently, X-ray microscopy has been used for probing the penetration of topically applied drugs into human skin [34]. We have highlighted in Ref. [34] advantages of X-ray microscopy in comparison to other established analytical techniques.

Dexamethasone is a glucocorticoid that is used for topical treatment of atopic dermatitis in particular. Dexamethasone can be measured in human skin *ex vivo* by X-ray microscopy [34]. Selective probing is accomplished by core level excitation of the O 1s → π^*-resonance at the C3-site. X-ray microscopy allowed us to suppress the background signal of glutaraldehyde fixed skin and to determine absolute drug concentrations as a function of depth after 4 h of dexamethasone application. This proof-of-concept study [34] indicated that also local variations of drug concentration occur in the stratum corneum, which provided evidence that the glucocorticoid is located in the intercellular lipid matrix and does not efficiently penetrate the corneocytes. More recently, we have also investigated by X-ray microscopy the role of topically applied core-multishell nanocarriers transporting dexamethasone into human skin [35].

This work goes beyond our recent study [34], here we report on systematic variations of the drug penetration time and the effect of mechanical removal of the outer stratum corneum by tape-stripping. In addition, we report on high resolution images, indicating that dexamethasone is indeed exclusively found in the lipophilic interspaces. Here, we aim also to determine the systematic of drug penetration, which becomes possible using a substantially higher spatial resolution than has been communicated before by label-free spectromicroscopy on drugs penetrating skin. Using tunable soft X-rays along with X-ray microscopy provides new insights regarding drug localization and penetration processes.

2. Materials and methods

2.1. Exposure of human skin ex vivo to dexamethasone and sample preparation

Human skin samples were prepared using excised human abdominal skin from one healthy female donor undergoing plastic surgery. The study was approved by the Ethics Committee of the Charité – Universitätsmedizin Berlin (approval EA/1/135/06 updated 07.2015). It was in accordance with the Declaration of Helsinki guidelines and the samples were obtained after the signed consent of the patients. The excised skin was examined for injuries or morphological changes. Only those samples with intact skin surface were used. The subcutaneous fat was removed and the skin was cut into 2 cm × 2 cm pieces. The skin samples were topically exposed to formulations containing dexamethasone using areas of 1 cm × 1 cm either as they were (intact barrier) or after they were tape-stripped 30 times (partial barrier disruption) [36]. 1.5% dexamethasone were dissolved in 70% ethanol. This solution was incorporated in hydroxethyl cellulose (HEC; Euro OTC Pharma; Cologne, Germany) gel for testing. Control samples were treated with drug-free HEC gel. Following preincubation of the skin in a humidified chamber for 10 min at 32 °C, 40 µL of dexamethasone gel (total dexamethasone load 600 µg/cm^2; infinite drug dosing) was applied and left in place for 10 min, 100 min, and 1000 min, respectively. Then, the residual gel was removed by means of a dry cotton swab followed by one tape-strip and the skin was cut into 1 mm × 1 mm pieces using a razor blade. These were fixed for 3 h at room temperature using 2.5% glutaraldehyde in 0.1 M Na-cacodylate buffer. Samples were subsequently post-fixed by 1% OsO_4, 0.8% $K_4[(Fe(CN)_6]$ in 0.1 M cacodylate buffer, and dehydrated by washing steps in water with an increasing fraction of ethanol (50–100%). Loss of dexamethasone due to washing with ethanol is avoided by fixation with OsO_4. We also conducted additional measurements on samples without fixation preceding the washing step. As a result, no drug was probed in these samples by X-ray microscopy (not shown). The samples were then embedded in epoxy resin EPON (Electron Microscopy Sciences, Kit 812, Hatfield, MA, U.S.A.) and regions of interest were cut into 350 nm sections by means of a microtome RM2065 (Leica, Wetzlar, Germany). Finally, the samples were placed on silicon nitride windows (thickness 100 nm, Silson, Northampton, UK). The samples were prepared in duplicates (n = 2) for each drug penetration time to be investigated by X-ray microscopy.

2.2. Measurement of thickness of the skin slices

The thickness of the vertical skin sections was determined by atomic force microscopy (NeaSNOM, Neaspec, Martinsried, Germany, cf. [37,38]). The instrument was used in the intermittent contact mode (tapping frequency between 146 and 267 kHz, typical tapping amplitude 60 nm, scan sizes 25 µm × 100 µm, resolution 0.625 µm/pixel, 0.5 µm/pixel, respectively). The substrate was set as the point of origin, and the step at the edge of the EPON film taken as the sample thickness, which was determined at various positions, yielding 350 ± 20 nm. This information is used in the following to quantify the drug concentration and distribution. However, there were local regions that were more than 50 nm thicker than other parts of the samples, especially in the upper stratum corneum. This is a result of slightly irregular or ragged cuts or fraying of corneocytes.

2.3. Scanning transmission X-ray microscopy (STXM) measurements

The STXM experiments were performed at the MAXYMUS instrument (Bruker ASC, Bergisch Gladbach, Germany) at the electron storage ring BESSY II (Helmholtz Zentrum Berlin, Germany) [39,40]. It is located at the UE46-PGM-2 beamline. The beamline features an APPLE type undulator and a collimated plane grating monochromator with an effective energy range from 150 eV of up to 1900 eV using one high flux 600 L/mm blazed (0.7° angle) and a high resolution 1200 L/mm grating. Soft X-rays are focused onto the sample by using a Fresnel zone plate of 240 µm diameter

and 25 nm outer zone width, with maximum spatial resolution given by the X-ray spot size (31 nm FHWM). The transmitted X-rays were converted to optical photons using a P43 phosphor and detected by a photomultiplier (Hamamatsu C9744). The energy resolution (E/ΔE) was typically of the order of 4000 at an exit-slit size of 20 μm. The samples were scanned in the line mode, in which they were moved row by row at constant velocity through the X-ray beam. This corresponds to a smallest step size ranging between 50 nm and 100 nm. This allowed us to cover for each data point collected an area of 750 nm^2, which is of importance for inhomogeneously distributed species, such as drugs in human skin.

Penetration of dexamethasone into human skin was probed by Scanning Transmission X-ray Microscopy (STXM), similar to recent work [34]. Briefly, the carbonyl (C3) site was excited at the O 1s → π*-transition. The sensitivity of this approach was further improved compared to our recent work [34] by lowering the excitation energy from 530.6 eV to 530.1 eV. This reduced the previously noticed cross-sensitivity of dexamethasone relative to untreated skin samples [34].

A detailed description of the data analysis is given in our previous work [34]. Briefly, skin regions of 25 μm × 100 μm were investigated near the skin surface at two photon energies, i.e. on the O 1s → π*-resonance (530.1 eV) and in the pre-edge regime (528.0 eV). This allowed us to derive the differential absorption and to quantify the number density of the drug as a function of penetration time using the Beer-Lambert law. The sample thickness is determined by atomic force microscopy to be 350 ± 20 nm and the absorption cross section at 530.1 eV has also been determined before [34].

3. Results and discussion

Fig. 1 shows two typical X-ray micrographs taken at 530.1 eV (O 1s → π*-transition of dexamethasone) of two sections of skin samples that were exposed to dexamethasone for 10 min. Fig. 1(a) shows intact skin, whereas the sample shown in Fig. 1(b) is from tape-stripped skin. The color scheme used for Fig. 1 represents high transmission in red color and high absorption in blue color. Both micrographs show the top part of the skin samples near the surface, indicating that X-ray microscopy recorded at a single photon energy provides detailed information on the morphology of skin, where the spatial resolution is significantly higher than in optical microscopy. The top layer is identified by the stratified structure of the stratum corneum (SC). Clearly, the stratum corneum of the tape-stripped samples (cf. Fig. 1(b)) is thinner by about 50% than that of the intact skin (see Fig. 1(a)). Fig. 1 also shows that the thickness of the viable epidermis is different in both samples.

One observes for both samples changes in absorption within the viable epidermis (VE), with lower absorption in the cell nuclei indicating a lower concentration of dexamethasone in these cellular compartments. These are identified by their round shape. Below the viable epidermis, in the dermis (DE), the dexamethasone amount sharply declines. Already these raw images shown in Fig. 1 indicate that there is evidence for absorption of dexamethasone. However, for a quantitative evaluation of the local drug concentration one has to apply the data reduction procedure outlined before [34].

Fig. 2 shows a series of drug penetration profiles recorded for different exposure times of human skin explants to dexamethasone. The data evaluation was performed as in recent work, where only four hours of dexamethasone exposure were investigated [34]. Each sample was investigated at two different locations for considering variations of local inhomogeneities and thickness of the skin layers.

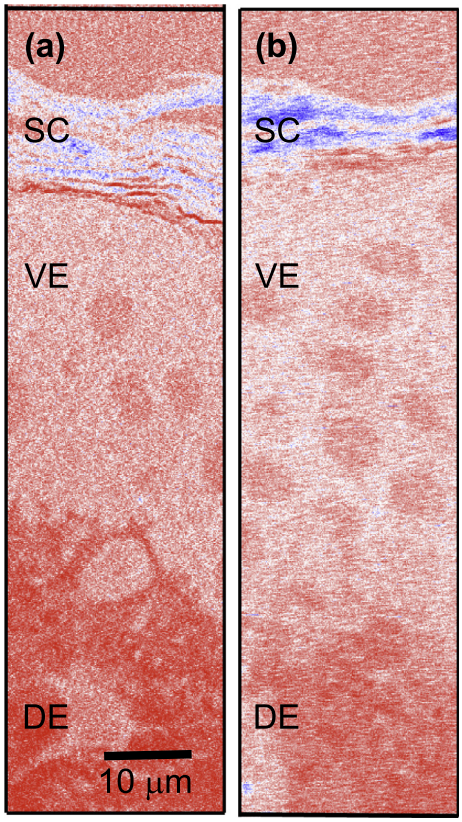

Fig. 1. X-ray micrographs of human skin *ex vivo* recorded at 530.1 eV: (a) topical exposure time to dexamethasone: 10 min of intact human skin; (b) topical exposure time to dexamethasone: 10 min of tape-stripped human skin. The samples were vertically aligned to the skin surface. The skin layers are labeled as follows: SC: stratum corneum; VE: viable epidermis, DE: dermis. The false color image indicates blue color for high absorption and red color for low absorption of dexamethasone. (For interpretation of the references to color in this figure legend, the reader is referred to the web version of this article.)

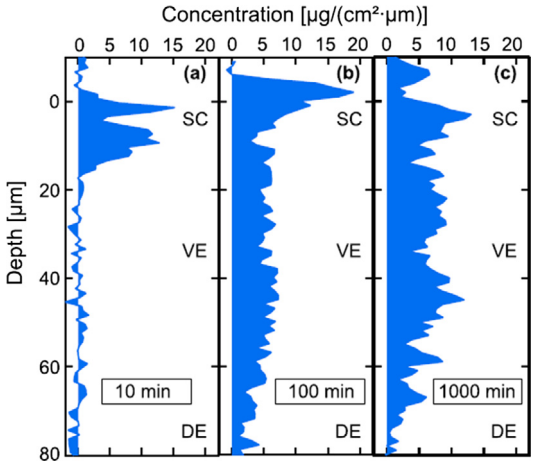

Fig. 2. Depth profiles of dexamethasone in human skin with intact SC following an exposure for: (a) t = 10 min; (b) t = 100 min; (c) t = 1000 min. The samples were vertically aligned to the skin surface, where the zero point of the depth scale is located. The location of different skin layers is indicated by SC (stratum corneum), VE (viable epidermis), and DE (dermis).

Briefly, from the optical density and the known absorption cross section of dexamethasone at 530.1 eV, as well as the sample thickness obtained from atomic force microscopy the depth dependent local concentration of dexamethasone is determined, which is used

to derive the horizontal axes of Figs. 2 and 3. The local drug concentration is referenced to an area of 1 cm^2 at a certain depth in μm, yielding the unit μg/(cm^2 μm), as it was reported in [34]. In addition, we also derive the total amount of drug found in a given skin region, i.e. stratum corneum, viable epidermis, and dermis, within an area of 1 cm^2. The attribution to specific skin layers is based on optical microscopy images as well as STXM results (see Fig. 1). These quantities appear to be useful for quantifying the drug penetration processes. The fraction of penetrating drug is determined from the drug concentration to which the skin sample was initially exposed (600 μg/cm^2). Note that the depth scale of the three skin samples has been re-aligned relative to the skin surface, which is required, since each sample shows a slightly different thickness of each skin layer. High drug concentration above the skin surface can be related to remaining drug formulation. These remaining amounts of drug are considered for estimating the total amount of dexamethasone. In addition, we marked in Figs. 2 and 3 the location of the stratum corneum (SC), the viable epidermis (VE), and the dermis (DE).

We chose three drug penetration times (t = 10 min, t = 100 min, and t = 1000 min). The results indicate that in the beginning (t = 10 min) the entire amount of drug that is penetrating into the skin is found in the stratum corneum (see Fig. 2(a)). The amplitude of the local drug concentration reaches after t = 10 min up to 15 μg/(cm^2 μm). There are some variations in local drug concentration, which are either caused by the non-uniform drug penetration into the lipophilic layers of the stratum corneum or defects.

Note that no background from untreated skin was subtracted in order to account for possible cross-sensitivity, which was observed before (cf. Ref. [34]). Hence, the drug concentration within the SC can be considered as an upper limit, which is estimated to affect mostly the stratum corneum by ~10% (cf. Ref. [34]). The present results indicate that there is no exponential drop in drug concentration, as was deduced for related drug formulations from tape-stripping studies [19]. Note that the spatial resolution obtained from X-ray microscopy provides more details than can be observed by standard approaches. This explains that there are deviations between the present and previous work. Especially, variations of local drug concentration within the stratum corneum cannot be probed by low spatial resolution work. Another reason for this finding is that some of the drug formulation may stick to the skin surface and is not removed by a single tape-strip at the end of the drug exposure time. As a result, in all cases shown in Fig. 2 the highest drug concentration occurs at the skin surface or slightly above. These drug penetration profiles show, unlike tape-stripping studies [19], that there are variations in local drug concentration within the stratum corneum. Recent low resolution X-rays microscopy work already indicated that the drug is not penetrating into the corneocytes, but rather remains in the lipophilic extracellular matrix in between [34], which is in agreement with the well-known bricks and mortar model [41,42]. Certainly, the local drug concentration is not properly displayed under these conditions, since from earlier electron microscopy and diffraction studies, these lipophilic structures are known to consist of narrow lamellar structures of ~13 nm periodicity separating the corneocytes [1,43]. These structures are essential for the barrier function of skin and consist mostly of glycolipids, ceramides, and fatty acids. They are not resolved at the spatial resolution used for recording Fig. 2. However, the spatial resolution can be further enhanced, as it is detailed further below. Clearly, no dexamethasone was found in the viable epidermis after 10 min penetration time. Considering that approximately 600 μg dexamethasone were topically applied per cm^2 skin, only 135 ± 25 μg were found per cm^2 as the total amount within the entire stratum corneum, corresponding to (23 ± 5)% of the applied drug. This corresponds to a maximum penetration velocity of 2.0 ± 0.2 μm/min for filling the entire stratum corneum with dexamethasone.

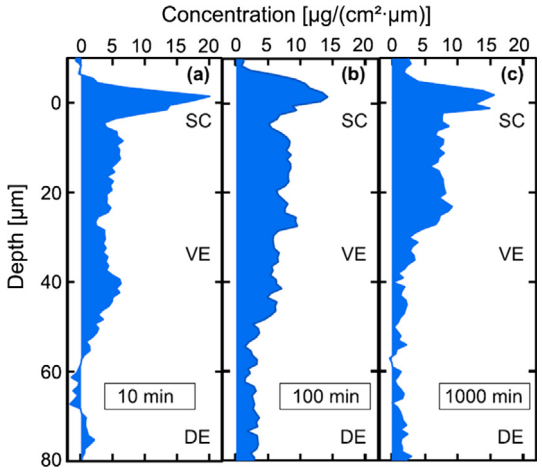

Fig. 3. Depth profiles of tape-stripped human skin treated with dexamethasone for different drug penetration times: (a) t = 10 min; (b) t = 100 min; (c) t = 1000 min. The samples were vertically aligned to the skin surface, where the zero point of the depth scale is located. The location of different skin layers is indicated by SC (stratum corneum), VE (viable epidermis), and DE (dermis).

As the penetration time is extended to 100 min (cf. Fig. 2(b)), the drug penetration profile is significantly changed, where the distinct maximum of the drug concentration is still found in the stratum corneum with a slightly higher amplitude in local concentration (see Fig. 2(b)). The total amount of dexamethasone in the stratum corneum is similar to t = 10 min, yielding for t = 100 min 100 ± 20 μg/cm^2. In addition, there is drug found in the viable epidermis with a lower local concentration reaching up to ca. 7 μg/(cm^2 μm). The drug concentration profile appears to be noisy, which is essentially ascribed to the heterogeneous composition of the viable epidermis consisting of ~95% keratinocytes. The drug penetrates also into the cell nuclei, but there is a concentration gradient between the cytoplasm and the nuclei. Therefore, local drug concentration depends on the investigated cut, i.e. if cell nuclei or cytoplasm is probed, explaining a heterogeneous local drug concentration. We find a total amount of 300 ± 50 μg/cm^2 of dexamethasone in the viable epidermis and a smaller amount of 65 ± 25 μg/cm^2 in the dermis, if the top 23 μm are analyzed. The total amount of dexamethasone that is found after 100 min in the skin section shown in Fig. 2(b) is 470 ± 60 μg/cm^2, corresponding to (80 ± 10)% of the topically applied drug. This mass balance indicates that within 100 min most of the dexamethasone is still located in the top skin layers and has not penetrated into the dermis in a substantial amount. Penetration corresponds roughly to more than a tripling of the penetrated drug compared to 10 min penetration time. This means that the stratum corneum is readily filled with dexamethasone, but once this process is finished, the permeation into the viable epidermis leads to a load of 300 ± 50 μg/cm^2, which corresponds to roughly a 1:3 partitioning of the absorbed drug that is found in the stratum corneum and the viable epidermis. Note that there is a characteristic drop in local drug concentration approximately at a depth of 10 μm, which is at the border between the stratum corneum and the viable epidermis, respectively. This was also seen in our previous work [34] and indicates that no local defect of the skin sample under study is the reason for this observation, but rather a general property of human skin. In addition, we observe a drop in drug concentration to the basal membrane separating the viable epidermis from the dermis approximately at a depth of 60 μm. This is taken as evidence that this skin layer represents another barrier for drug penetration, as is detailed further below.

Fig. 2(c) shows the distribution of dexamethasone after 1000 min. The following characteristics are observed: The amplitude of local drug concentration in the stratum corneum is decreased by about 30% relative to the shorter penetration times, so that a maximum amplitude of 13 μg/(cm^2 μm) is observed. The total amount of dexamethasone in the stratum corneum (SC) and in the viable epidermis (VE) are similar to those as after 100 min (SC: 120 ± 40 μg/cm^2 and VE: 300 ± 40 μg/cm^2), indicating that these concentrations can be assumed to be in an equilibrium condition. We also observe after 1000 min penetration time a drop in drug concentration near the basal membrane, similar as it is observed for 100 min penetration time. The concentration in the top layer of the dermis remains low, i.e. 90 ± 70 μg/cm^2. In total 500 ± 90 μg/cm^2 dexamethasone have penetrated the skin, which corresponds to about (85 ± 15)% of the applied drug. This underscores the fact that the most superficial skin layers, due to the depletion of dexamethasone in the applied gel, have reached a maximum drug loading capacity and its loss by distribution into the dermis and systemic uptake is slow. This is in agreement with a study in volunteers, in which urinary excretion of dexamethasone has been documented [3].

Moreover, the mass balance allows us to estimate the accuracy of the entire study reaching from sample preparation to data analysis. The missing amount of dexamethasone at higher exposure times ($t \geqslant 100$ min) is determined to be 15–20% and should be due to not penetrated drug which is removed by washing and the single tape-strip together with the remaining gel as well as a minor fraction that has penetrated into the dermis. As a result, the present results clearly indicate that the fixation process as well as using ethanol as a solvent does not have a significant impact on this missing fraction of the drug.

Dexamethasone penetration was also studied in tape-stripped skin from the same donor in order to investigate the importance of damage of the stratum corneum (cf. Fig. 1). The results are compiled in Fig. 3, indicating that the penetration of dexamethasone is significantly increased after 10 min, if the stratum corneum is removed by about 50%. The total amount of dexamethasone observed in this tape-stripped skin sample is 320 ± 60 μg/cm^2, of which 110 ± 50 μg/cm^2 are located in the stratum corneum and even 210 ± 40 μg/cm^2 in the viable epidermis (cf. Fig. 3(a)). This corresponds to ∼(55 ± 10)% of the topically applied drug and underscores that the barrier of the stratum corneum is reduced. Clearly, within 10 min the drug has reached a depth of 60 μm, which means that the penetration velocity has tripled from 2.0 ± 0.2 μm/min to 6.0 ± 0.2 μm/min. Again, at 10 min penetration time no significant amount of drug is found in the top part of the dermis (5 ± 3 μg per cm^2).

After 100 min the total amount of drug in the stratum corneum remains similar compared to t = 10 min in the tape-stripped sample (see Fig. 3(b)), implying that the penetration of dexamethasone in this layer 90 ± 35 μg/cm^2 has reached an equilibrium. The total amount of drug in the viable epidermis is increased to 270 ± 40 μg/cm^2, and the top part of the dermis contains 110 ± 30 μg/cm^2, so that in total 470 ± 60 μg/cm^2 have penetrated within 100 min, corresponding to (80 ± 10)% of the topically applied drug. The absolute value of drug found is similar to the value of intact skin. However absolute values are dependent on the local thickness of the skin layers. Despite the absolute value of drug found in both skin samples one can see that the average dexamethasone concentration within the viable epidermis of the tape-stripped sample increases from roughly 5 μg/(cm^2 μm) to approximately 7 μg/(cm^2 μm) compared to the intact skin.

Fig. 3(c) shows the situation after 1000 min. The highest amplitude in local drug concentration is still found in the stratum corneum and its maximum is similar to shorter exposure times (16 μg/(cm^2 μm)). The total amount of dexamethasone in the stratum corneum is 80 ± 30 μg/cm^2, i.e. slightly lower than at shorter drug penetration times. Similar findings are observed for the viable epidermis, where only 150 ± 15 μg/cm^2 of dexamethasone are found. This provides evidence that there is significant drug permeation into the dermis, for which we observe to a depth of 80 μm 100 ± 30 μg/cm^2. Note that in the skin section shown in Fig. 3(c) the drop in drug concentration into the dermis is observed at significantly lower depth (near 30 μm) than in the other skin sections, where it occurs about 20 μm deeper. This implies that the basal membrane is at this specific position closer to the skin surface than in the other samples, corresponding in the investigated sample to smaller thickness of the viable epidermis. This might explain the lower amount of drug that is extrapolated to be found in the entire viable epidermis, if the drug loading capacity scales with the thickness of this layer. On the other hand, substantial amounts of the drug are found in the dermis. If we sum up all compartments, we observe 325 ± 50 μg/cm^2, which corresponds only to (55 ± 8)% of the applied drug that is found after 1000 min penetration time. For instance, for intact skin (85 ± 15)% of the topically applied drug were found in the different skin layers. This might hint that there is already substantial drug diffusion into lower parts of the dermis, which are not probed in this study. We discuss this point in the following.

We summarize the above discussed findings shown in Figs. 2 and 3 for the viable epidermis in Fig. 4. Fig. 4(a) represents the total mass of dexamethasone in the viable epidermis of skin with intact stratum corneum, as obtained from numerical integration from the experimental results shown in Fig. 2. These results indicate for intact skin (blue bars) that the drug load reaches saturation already after 100 min penetration time. The red bars indicate a similar behavior for tape-stripped skin. However, it appears that there might be evidence for a loss of drug load already after 100 min. This might indicate that there is permeation of the drug into the dermis at penetration times exceeding 100 min. However, a close inspection of the samples under study indicates that there are variations in thickness of the skin layers in the analyzed skin areas, which need to be taken into account. This is specifically true for the tape-stripped skin sample that was exposed for 1000 min to dexamethasone (cf. Fig. 3(c)). Such variations between different skin areas appear to be misleading, so that we normalized the thickness of the viable epidermis to identical values, as shown in Fig. 4(b). Then, it becomes evident that the drug concentration reaches at long exposure times a maximum value independent from mechanical damage of the stratum corneum by tape-

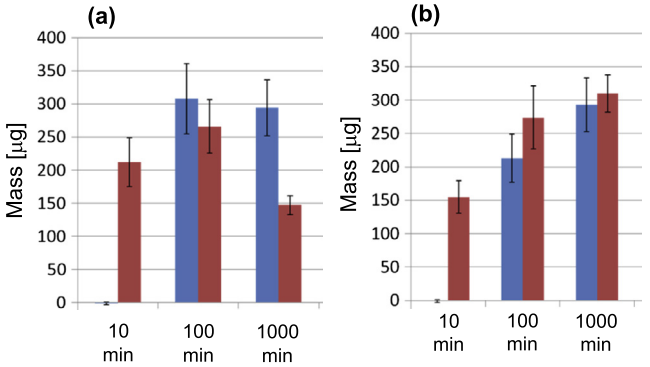

Fig. 4. (a) Mass of dexamethasone concentration within the viable epidermis as a function of the drug penetration time. The data corresponding to the blue bars are taken from Fig. 2 (skin with intact SC), the red bars are derived from Fig. 3 (tape-stripped skin); (b) Mass of dexamethasone in the viable epidermis corrected for a constant thickness of this skin layer (see text for details). (For interpretation of the references to color in this figure legend, the reader is referred to the web version of this article.)

stripping. This hints to the fact that the viable epidermis has a certain drug loading capacity and that the permeation of drug into the dermis is not dominating in the time periods investigated in this work.

Note that such normalizations on the layer thickness are primarily suitable for the viable epidermis due to its substantial variations in thickness. Similar corrections for the stratum corneum would add substantial error bars to the analysis, which is due to its small thickness as well as an inhomogeneous lateral drug distribution. Therefore, we have not included such corrections for the stratum corneum.

The stratum corneum represents a first, and well-known barrier for drug penetration. Other barriers are identified by changes in drug concentration in the vertical drug penetration profiles. There is a distinct minimum that occurs in the region below the stratum corneum (cf. Figs. 2(b) and (c), and 3(a) and (b) and [34]), i.e. near the granular cell layer [44], where tight junctions are known to occur. Defects in the skin samples can be ruled out and one might ask why there is no such minimum in Fig. 3(c). This is due to a slightly bent stratum corneum in the investigated skin area, which washes out this structure. Furthermore, another characteristic drop in drug concentration is always found in the region of the basal cells. There, the drug concentration drops within 5–10 μm, as shown in Figs. 2 and 3. This hints to another skin barrier within these palisade shaped cell layer, in which the drug concentration appears to drop near the background level. This concentration gradient cannot be due to a fast diffusive transport mechanism, which would lead to massive loss of dexamethasone into the dermis, which is, according to the mass balances outlined above, not observed. We may consider that the drug is well penetrating into the epidermal cell layer, which goes along with uptake into the cell nuclei and interactions with the glucocorticoid receptors [45]. This leads to hydrogen bonding with the C3 site that is probed in the experiments. It is known that hydrogen bonding leads to changes in electronic properties of molecular species [46]. If that is the case, then the local drug concentration is possibly underestimated, since the drug bound to the acceptor might absorb at a different photon energy. Here, we can only consider this general possibility, but a quantification is required by additional experiments that go beyond the scope of the present study.

Finally, we discuss high spatial resolution capabilities of X-rays microscopy. Fig. 5(a) shows with high spatial resolution, i.e. a step width of 50 nm, a section of the lower stratum corneum of intact skin, i.e. the region near the stratum granulosum after 10 min of dexamethasone penetration. There, the occurrence of dexamethasone is indicated by blue color. The stratified structure of the stratum corneum is clearly visible, as in Fig. 1, but the step width allows us to get further insights into the local drug distribution. Different regions are visible, corresponding to changes in X-ray absorption of the sample. It is evident that the drug is only contained in those regions of light color, i.e. optically thinner regions than the other ones. This region corresponds to the lipid phase with its lamellar structure. It contains mostly carbon and low amounts of absorbing material in the O 1s-near-edge regime, which is consistent with earlier work [42,47]. Their width is typically of the order of 100 nm. In some sections, wider regions occur with diameters reaching up to 350 nm. These might be due to desmosomes [42]. Regions corresponding to keratin-rich corneocytes are indicated by red color in Fig. 5(a). Earlier work has shown that their composition undergoes depth dependent changes, as proved by vibrational spectroscopy [48]. The present results indicate that there is a strong depth dependent variation of local drug concentration, which is unlike an exponential drop in drug concentration, as deduced from tape-stripping studies [19]. The present findings are similar to those obtained from high resolution electron microscopy along with EDX analysis on the penetration of species

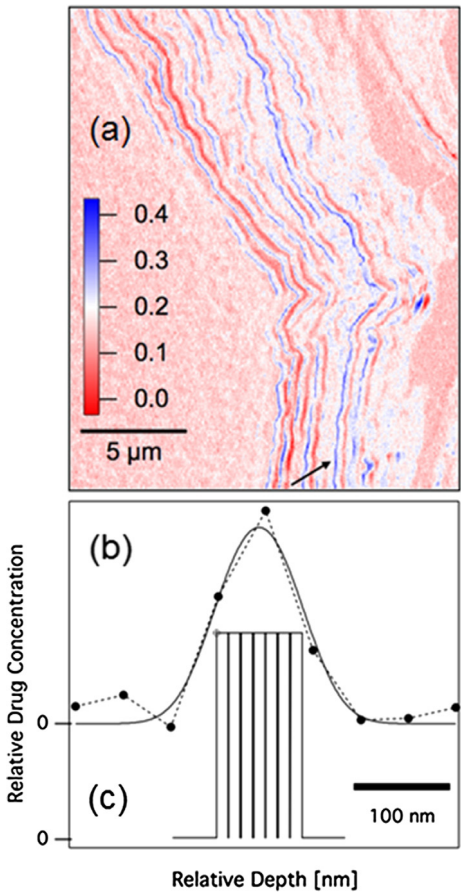

Fig. 5. (a) High-resolution X-ray micrograph of the lower part of the stratum corneum following dexamethasone exposure for 10 min (left: viable epidermis, right: skin surface, cf. Fig. 1)). The false color image shows the optical density due to the local concentration of dexamethasone derived from X-ray micrographs recorded at 530.1 eV and 528.0 eV, respectively. High drug concentration is indicated by blue color, red color corresponds to low drug concentration (see text for details). The arrow marks the position which was used for evaluating (b); (b) detailed view of the relative dexamethasone concentration within a single lipophilic channel. The experimental data points (step width: 50 nm) are linked by a dashed line to guide the eye. The full curve corresponds to a Gaussian of 70 ± 5 nm; (c) result of the spectral de-convolution yielding the spatial drug distribution after having considered the spatial resolution of the X-rays microscope (see text for details). (For interpretation of the references to color in this figure legend, the reader is referred to the web version of this article.)

containing heavy elements [25]. However, drugs containing light elements, such as dexamethasone, cannot be probed by EDX, which highlights the advantage of label-free spectromicroscopy in the soft X-ray regime. The present results also give evidence for the validity of the classical bricks and mortar model [41] and show that the penetration of dexamethasone evidently only proceeds via the lipophilic phase.

We also analyzed the drug distribution within a narrow region of ~1 μm length of a single lipophilic channels in greater detail, as shown in Fig. 5(a) (indicated by an arrow) and Fig. 5(b). In this way it was attempted to find out how the drug is distributed within the lipophilic lamellae structures. Fig. 5(b) shows on a relative scale the local drug concentration for this region, which vertically cuts the lamellae. The experimentally observed drug distribution profile is the result of a convolution of the actual drug distribution within the lipophilic lamellae with a Gaussian profile (FWHM = 70 ± 5 nm). This broadening is due to the limited spatial resolution provided by the zone plate and the X-ray optics. In a subsequent step we de-convoluted the experimentally observed profile shown in Fig. 5(b) in order to derive the drug distribution profile in this skin region, which cannot be observed directly. The

result is depicted in Fig. 5(c). The experimental profile, corresponding to a Gaussian-type broadening, can be transformed into a rectangular structure with a width of 91 nm.

We also indicate in Fig. 5(c) the 13 nm periodicity in the lipophilic phase [1], but these fine details do not affect the result of the de-convolution. The value of 91 nm is rationalized by 7 lipid layers in which the drug is penetrating with the same local concentration. The overall breadth of these structures is comparable to previous electron microscopy studies [42,49]. We also tried to vary the number of lipid layers used for the de-convolution of the experimental drug profile, but this did not yield results resembling the experimental findings. We conclude from these results, that the lipophilic drug dexamethasone penetrates the narrow regions of the extracellular lipid domains of the stratum corneum by all available lamellae and at similar concentration within each layer after 10 min penetration time. There are also regions in Fig. 5(a), in which the drug is wider spread. More systematic work is required to explore the drug penetration process at high spatial resolution and chemical selectivity provided by X-ray microscopy, where different penetration time and different locations need to be considered. This will also shed light on drug penetration into corneocytes, which is not observed after 10 min penetration time. These systematic investigations go beyond the scope of this work, but the present results already highlight the potential of high resolution studies performed by X-ray spectromicroscopy.

4. Conclusions

Label-free detection of dexamethasone in human skin is probed by scanning X-ray microscopy. This approach is suitable to probe quantitatively and with high spatial resolution reaching 70 nm the time-resolved penetration of dexamethasone. Focus of the present study is intact and tape-stripped skin in order to determine the impact of the damage of the stratum corneum regarding drug penetration into the viable epidermis and dermis. Local drug concentrations are determined for the penetration times 10 min, 100 min, and 1000 min with a spatial step width of 1 μm. Furthermore, the total amounts of dexamethasone in the stratum corneum, the viable epidermis, and the top part of the dermis are determined, as well. The spatially resolved distribution of dexamethasone in human skin shows significant minima near the stratum granulosum and the basal layer, which provides evidence for the occurrence of drug penetration barriers.

Furthermore, the potential of X-ray microscopy is explored for studying the drug penetration process with high spatial resolution. It is derived that dexamethasone penetrates the lipophilic intercellular structures of the stratum corneum with the same concentration in each lamella structure, as derived from de-convolutions of the local drug concentration. Further systematic work is proposed to derive a molecular understanding of drug penetration that is based on label-free spectromicroscopy.

Acknowledgments

Financial support by German Research Foundation (DFG) within SFB 1112 is gratefully acknowledged. Support of this work by the Helmholtz-Zentrum Berlin and Freie Universität Berlin is gratefully acknowledged. We thank G. Ulm (Physikalisch-Technische Bundesanstalt, Berlin) for the access to the atomic force microscope as well as P. Patoka and G. Ulrich for determining the thickness of the skin samples.

References

[1] J.A. Bouwstra, P.L. Honeywell-Nguyen, G.S. Gooris, M. Ponec, Structure of the skin barrier and its modulation by vesicular formulations, Prog. Lipid Res. 42 (2003) 1–36.
[2] J.D. Bos, M.M. Meinardi, The 500 Da rule for the skin penetration of chemical compounds and drugs, Exp. Dermatol. 9 (2000) 165–169.
[3] A. Rougier, D. Dupuis, C. Lotte, R. Roguet, H. Schaefer, In vitro correlation between stratum corneum reservoir function and percutaneous absorption, J. Invest. Dermatol. 81 (1983) 275–278.
[4] Y.-K. Lin, S.-H. Yang, C.-C. Chen, H.-C. Kao, J.-Y. Fang, Using imiquimod-induced psoriasis-like skin as a model to measure the skin penetration of anti-psoriatic drugs, PLoS ONE 10 (2015) e0137890, 19 pages.
[5] D.W. Kim, J.Y. Park, G.Y. Na, S.J. Lee, W.J. Lee, Correlation of clinical features and skin barrier function in adolescent and adult patients with atopic dermatitis, Int. J. Dermatol. 45 (2006) 698–701.
[6] T. Oshizaka, H. Todo, K. Sugibayashi, Effect of direction (epidermis-to-dermis and dermis-to-epidermis) on the permeation of several chemical compounds through full-Tfhickness skin and stripped skin, Pharm. Res. 29 (2012) 2477–2488.
[7] A.C. Williams, B.W. Barry, Penetration enhancers, Adv. Drug Del. Rev. 64 (2012) 128–137.
[8] D. Horita, H. Todo, K. Sugibayashi, Effect of ethanol pretreatment on skin permeation of drugs, Biol. Pharm. Bull. 35 (2012) 1343–1348.
[9] OECD, Test No. 428: Skin Absorption, In Vitro Method, OECD Publishing, Paris, 2004.
[10] M. Schäfer-Korting, U. Bock, W. Diembeck, H.J. Duesing, A. Gamer, E. Haltner-Ukomadu, C. Hoffmann, M. Kaca, H. Kamp, S. Kersen, M. Kietzmann, H.C. Korting, H.U. Krachter, C.M. Lehr, M. Liebsch, A. Mehling, C. Mueller-Goymann, F. Netzlaff, F. Niedorf, M.K. Rubbelke, U. Schafer, E. Schmidt, S. Schreiber, H. Spielmann, A. Vuia, M. Weimer, The use of reconstructed human epidermis for skin absorption testing: results of the validation study, ATLA 36 (2008) 161–187.
[11] C. Herkenne, A. Naik, Y.N. Kalia, J. Hadgraft, R.H. Guy, Dermatopharmacokinetic prediction of topical drug bioavailability in vivo, J. Invest. Dermatol. 127 (2007) 887–894.
[12] H. Wagner, K.H. Kostka, C.M. Lehr, U.F. Schaefer, Human skin penetration of flufenamic acid: in vivo/in vitro correlation (deeper skin layers) for skin samples from the same subject, J. Invest. Dermatol. 118 (2002) 540–544.
[13] J.P. Medendorp, K.S. Paudel, R.A. Lodder, A.L. Stinchcomb, Near infrared spectrometry for the quantification of human dermal absorption of econazole nitrate and estradiol, Pharm. Res. 24 (2007) 186–193.
[14] A. Gysler, B. Kleuser, W. Sippl, K. Lange, H.C. Korting, H.D. Höltje, M. Schäfer-Korting, Skin penetration and metabolism of topical glucocorticoids in reconstructed epidermis and in excised human skin, Pharm. Res. 16 (1999) 1386–1391.
[15] M. Lapteva, K. Mondon, M. Möller, R. Gurny, Y.N. Kalia, Polymeric micelle nanocarriers for the cutaneous delivery of tacrolimus: a targeted approach for the treatment of psoriasis, Mol. Pharm. 11 (2014) 2989–3001.
[16] C.S. Maia, W. Mehnert, M. Schaller, H.C. Korting, A. Gysler, A. Haberland, M. Schäfer-Korting, Drug targeting by solid lipid nanoparticles for dermal use, J. Drug Target. 10 (2002) 489–495.
[17] P. Schlupp, T. Blaschke, K.D. Kramer, H.D. Hoeltje, W. Mehnert, M. Schäfer-Korting, Drug release and skin penetration from solid lipid nanoparticles and a base cream: a systematic approach from a comparison of three glucocorticoids, Skin Pharmacol. Physiol. 24 (2011) 199–209.
[18] S. Mitriaikina, C.C. Müller-Goymann, Comparative permeation studies of nondiluted and diluted betamethasone-17-valerate semisolid formulations through isolated human stratum corneum and artificial skin construct, Skin Pharmacol. Physiol. 22 (2009) 142–150.
[19] S. Wiedersberg, A. Naik, C.S. Leopold, R.H. Guy, Pharmacodynamics and dermatopharmacokinetics of betamethasone 17-valerate: assessment of topical bioavailability, Brit. J. Dermatol. 160 (2009) 676–686.
[20] L.M. Russell, R.H. Guy, Measurement and prediction of the rate and extent of drug delivery into and through the skin, Expert Opin. Drug Del. 6 (2009) 355–369.
[21] S. Wiedersberg, C.S. Leopold, R.H. Guy, Dermatopharmacokinetics of betamethasone 17-valerate: Influence of formulation viscosity and skin surface cleaning procedure, Eur. J. Pharm. Biopharm. 71 (2009) 362–366.
[22] H.J. Weigmann, J. Lademann, S. Schanzer, U. Lindemann, R. von Pelchrzim, H. Schaefer, W. Sterry, V. Shah, Correlation of the local distribution of topically applied substances inside the stratum corneum determined by tape-stripping to differences in bioavailability, Skin Pharmacol. Appl. Skin Physiol. 14 (2001) 98–102.
[23] B. Mueller, Y.G. Anissimov, M.S. Roberts, Unexpected clobetasol propionate profile in human stratum corneum after topical application in vitro, Pharm. Res. 20 (2003) 1835–1837.
[24] J.A. Bouwstra, G.S. Gooris, J.A. Vanderspek, W. Bras, Structural investigations of human stratum-corneum by small-angle X-ray scattering, J. Invest. Dermatol. 97 (1991) 1005–1012.
[25] H.E. Boddé, M.A.M. Kruithof, J. Brussee, H.K. Koerten, Visualization of normal and enhanced $HgCl_2$ transport through human skin - in vitro, Int. J. Pharm. 53 (1989) 13–24.
[26] N. Alnasif, C. Zoschke, E. Fleige, R. Brodwolf, A. Boreham, E. Rühl, K.-M. Eckl, H.-F. Merk, H.C. Hennies, U. Alexiev, R. Haag, S. Küchler, M. Schäfer-Korting, Penetration of normal, damaged and diseased skin – an in vitro study on dendritic core-multishell nanotransporters, J. Control. Release 185 (2014) 45–50.
[27] L.P.J. Cruysberg, R. Nuijts, D.H. Geroski, L.H. Koole, F. Hendrikse, H.F. Edelhauser, In vitro human scleral permeability of fluorescein, dexamethasone-fluorescein, methotrexate-fluorescein and rhodamine 6G

and the use of a coated coil as a new drug delivery system, J. Ocular Pharmacol. Therap. 18 (2002) 559–569.
[28] S. Küchler, M.R. Radowski, T. Blaschke, M. Dathe, J. Plendl, R. Haag, M. Schäfer-Korting, K.D. Kramer, Nanoparticles for skin penetration enhancement – a comparison of a dendritic core-multishell-nanotransporter and solid lipid nanoparticles, Eur. J. Pharmaceut. Biopharm. 71 (2009) 243–250.
[29] J. Dreier, J.A. Sorensen, J.R. Brewer, Superresolution and fluorescence dynamics evidence reveal that intact liposomes do not cross the human skin barrier, PLoS ONE 11 (2016) e0146514, 15 pages.
[30] A. Nilsson, R.J.A. Goodwin, M. Shariatgorji, T. Vallianatou, P.J.H. Webborn, P.E. Andren, Mass spectrometry imaging in drug development, Anal. Chem. 87 (2015) 1437–1455.
[31] B.G. Saar, L.R. Contreras-Rojas, X.S. Xie, R.H. Guy, Imaging drug delivery to skin with stimulated Raman scattering microscopy, Mol. Pharm. 8 (2011) 969–975.
[32] L. Franzen, M. Windbergs, Applications of Raman spectroscopy in skin research – from skin physiology and diagnosis up to risk assessment and dermal drug delivery, Adv. Drug Deliv. Rev. 89 (2015) 91–104.
[33] I.W. Schie, C. Krafft, J. Popp, Applications of coherent Raman scattering microscopies to clinical and biological studies, Analyst 140 (2015) 3897–3909.
[34] K. Yamamoto, R. Flesch, T. Ohigashi, S. Hedtrich, A. Klossek, P. Patoka, G. Ulrich, S. Ahlberg, F. Rancan, A. Vogt, U. Blume-Peytavi, P. Schrade, S. Bachmann, M. Schäfer-Korting, N. Kosugi, E. Rühl, Selective probing of the penetration of dexamethasone into human skin by soft X-ray spectromicroscopy, Anal. Chem. 87 (2015) 6173–6179.
[35] K. Yamamoto, A. Klossek, R. Flesch, T. Ohigashi, E. Fleige, F. Rancan, J. Frombach, A. Vogt, U. Blume-Peytavi, P. Schrade, S. Bachmann, R. Haag, S. Hedtrich, M. Schäfer-Korting, N. Kosugi, E. Rühl, Core-multishell nanocarriers: transport and release of dexamethasone probed by soft X-ray spectromicroscopy, J. Control. Release 242 (2016) 64–70.
[36] J. Lademann, H.J. Weigmann, C. Rickmeyer, H. Barthelmes, H. Schaefer, G. Mueller, W. Sterry, Penetration of titanium dioxide microparticles in a sunscreen formulation into the horny layer and the follicular orifice, Pharmacol. Appl. Skin Physiol. 12 (1999) 247–256.
[37] P. Hermann, A. Hoehl, P. Patoka, F. Huth, E. Rühl, G. Ulm, Near-field imaging and nano-Fourier-transform infrared spectroscopy using broadband synchrotron radiation, Opt. Exp. 21 (2013) 2913–2919.
[38] P. Patoka, G. Ulrich, A.E. Nguyen, L. Bartels, P.A. Dowben, V. Turkowski, T.S. Rahman, P. Hermann, B. Kästner, A. Hoehl, G. Ulm, E. Rühl, Nanoscale plasmonic phenomena in CVD-grown MoS_2 monolayer revealed by ultra-broadband synchrotron radiation based nano-FTIR spectroscopy and near-field microscopy, Opt. Exp. 24 (2016) 1154–1164.
[39] D. Nolle, M. Weigand, P. Audehm, E. Goering, U. Wiesemann, C. Wolter, E. Nolle, G. Schütz, Note: unique characterization possibilities in the ultra high vacuum scanning transmission X-ray microscope (UHV-STXM) "MAXYMUS" using a rotatable permanent magnetic field up to 0.22 T, Rev. Sci. Instrum. 83 (2012) 046112, 3 pages.
[40] D. Nolle, M. Weigand, G. Schuetz, E. Goering, High contrast magnetic and nonmagnetic sample current microscopy for bulk and transparent samples using soft X-rays, Microsc. Microanal. 17 (2011) 834–842.
[41] P. Eilas, Epidermal lipids, barrier function, and desquamation, J. Invest. Dermatol. 80 (1983) 44–49.
[42] P.M. Elias, Epiermal barrier function – intercellular lamellar lipid structures, origin, composition and metabolism, J. Control. Release 15 (1991) 199–208.
[43] E.H. Mojumdar, G.S. Gooris, D.J. Barlow, M.J. Lawrence, B. Deme, J.A. Bouwstra, Skin lipids: localization of ceramide and fatty acid in the unit cell of the long periodicity phase, Biophys. J. 108 (2015) 2670–2679.
[44] J.M. Brandner, Importance of tight junctions in relation to skin barrier function, Curr. Probl. Dermatol. 49 (2016) 27–37.
[45] D.W. Ray, C.S. Suen, A. Brass, J. Soden, A. White, Structure/function of the human glucocorticoid receptor: tyrosine 735 is important for transactivation, Mol. Endocrinol. 13 (1999) 1855–1863.
[46] T. Tokushima, Y. Horikawa, O. Takahashi, H. Arai, K. Sadakane, Y. Harada, Y. Takata, S. Shin, Solvation dependence of valence electronic states of water diluted in organic solvents probed by soft X-ray spectroscopy, Phys. Chem. Chem. Phys. 16 (2014) 10753–10761.
[47] J. van Smeden, M. Janssens, G.S. Gooris, J.A. Bouwstra, The important role of stratum corneum lipids for the cutaneous barrier function, Biochim. Biophys. Acta 2014 (1841) 295–313.
[48] G. Zhang, D.J. Moore, R. Mendelsohn, C.R. Flach, Vibrational microspectroscopy and imaging of molecular composition and structure during human corneocyte maturation, J. Invest. Dermatol. 126 (2006) 1088–1094.
[49] S. Daehnhardt-Pfeiffer, C. Surber, K.P. Wilhelm, D. Daehnhardt, G. Springmann, M. Boettcher, R. Foelster-Holst, Noninvasive stratum corneum sampling and electron microscopical examination of skin barrier integrity: pilot study with a topical glycerin formulation for atopic dermatitis, Skin Pharmacol. Physiol. 25 (2012) 155–161.

3.4 Soft X-ray microscopy for probing of topical tacrolimus delivery via micelles

Author:

K. Yamamoto, A. Klossek, K. Fuchs, B. Watts, J. Raabe, R. Flesch, F. Rancan, H. Pischon, M. Radbruch, A.D. Gruber, L. Mundhenk, A. Vogt,U. Blume-Peytavi, P. Schrade, S. Bachmann, R. Gurny, E. Rühl

Publication:

European Journal of Pharmaceutics and Biopharmaceutics

Publisher:

Elsevier

Date:

June 2019

European Journal of Pharmaceutics and Biopharmaceutics, Volume 139, June 2019, Pages 68-75

Online available at: https://doi.org/10.1016/j.ejpb.2019.03.006

Author contribution: In this work the author contributed to planning of the experiment, measurements, evaluating and interpreting the results, and wrote parts of the publication.

European Journal of Pharmaceutics and Biopharmaceutics 139 (2019) 68–75

Contents lists available at ScienceDirect

European Journal of Pharmaceutics and Biopharmaceutics

journal homepage: www.elsevier.com/locate/ejpb

Research paper

Soft X-ray microscopy for probing of topical tacrolimus delivery via micelles

K. Yamamoto[a], A. Klossek[a], K. Fuchs[b], B. Watts[c], J. Raabe[c], R. Flesch[a], F. Rancan[d], H. Pischon[e], M. Radbruch[e], A.D. Gruber[e], L. Mundhenk[e], A. Vogt[d], U. Blume-Peytavi[d], P. Schrade[f], S. Bachmann[f], R. Gurny[b], E. Rühl[a,*]

[a] Physikalische Chemie, Freie Universität Berlin, Arnimallee 22, 14195 Berlin, Germany
[b] Apidel SA, c/o The Business Harbour, 29 Quai du Mont Blanc, 1201 Geneva, Switzerland
[c] Swiss Light Source, Paul Scherrer Institut, Forschungsstraße 111, 5232 Villigen PSI, Switzerland
[d] Clinical Research Center for Hair and Skin Science, Department of Dermatology and Allergy, Charité – Universitätsmedizin Berlin, Corporate Member of Freie Universität Berlin, Humboldt-Universität zu Berlin, and Berlin Institute of Health, 10117 Berlin, Germany
[e] Institute of Veterinary Pathology, Freie Universität Berlin, Robert-von-Ostertag-Str. 15, 14163 Berlin, Germany
[f] Abteilung für Elektronenmikroskopie at CVK, 13353 Berlin, Germany

A B S T R A C T

The penetration of topically applied tacrolimus formulated in micelles into murine skin is reported, measured by X-ray microscopy. Tacrolimus and micelles are probed for the first time by this high spatial resolution technique by element-selective excitation in the C 1s- and O 1s-regimes. This method allows selective detection of the distribution and penetration depth of drugs and carrier molecules into biologic tissues. It is observed that small, but distinct quantities of the drug and micelles, acting as a drug carrier, penetrate the stratum corneum. A comparison is made with the paraffin-based commercial tacrolimus ointment Protopic®, where local drug concentrations show to be low. A slight increase in local drug concentration in the stratum corneum is observed, if tacrolimus is formulated in micelles, as compared to Protopic®. This underscores the importance of the drug formulations for effective drug delivery. Time-resolved penetration shows presence of drug in the stratum corneum 100 min after formulation application, with penetration to deeper skin layers at 1000 min. High resolution micrographs give indications for a penetration pathway along the lipid membranes between corneocytes, but also suggest that the compound may penetrate corneocytes.

1. Introduction

The sensitive detection of topically applied drugs within skin layers is an important issue, which has been addressed in various studies [1,2]. Some drugs easily penetrate into viable skin layers or even beyond via transdermal penetration, whereas others do not penetrate and remain essentially on the skin surface. This has been empirically determined for lipophilic drugs by the 500 Da rule, which implies that above this molecular mass efficient penetration is substantially impeded [3]. The essential barrier for this process is the stratum corneum. It was also shown that in inflammatory skin diseases, such as atopic dermatitis, the barrier function is decreased and the cutoff limit of penetrating substances is shifted to higher molecular weights [3]. Psoriasis-like lesions, epidermal hyperplasia, and hyperkeratosis may also affect the penetration of anti-inflammatory drugs [4].

Probing drugs encapsulated in nanoscopic particles after topical application on skin requires specific detection techniques, which have been reviewed recently [5]. Preferably, label-free approaches are required, by exploiting the inherent properties of the drugs and drug carriers. Several experimental approaches have been employed for label-free detection, which includes Raman-based approaches [6], atomic force microscopy [7], including tip-enhanced Raman scattering [8], photoacoustic nanoscopy [9], photothermal expansion [10], and X-ray microscopy [11].

Recently, the penetration of the lipophilic drug dexamethasone by scanning X-ray microscopy was reported [11–13]. These studies yielded quantitatively systematic findings at different penetration times, so that the amount of drug in different skin layers was determined. The central advantage of X-ray microscopy is that the results can be quantified due to Beer-Lambert law, $\ln(I/I_0) = -\sigma \cdot c \cdot d$, where I is the transmitted radiation, I_0 is the incident radiation, σ is the absorption cross section measured in Mbarn (1 Mbarn corresponds to 10^{-18} cm^2), c is the local concentration, and d is the thickness of the sample that is penetrated by soft X-rays. The quantity $\ln(I/I_0)$ is also called absorbance or optical density, probing the relative change of the transmitted radiation through the sample. Highest concentration of dexamethasone is found in the stratum corneum and there specifically in the lipid lamellae between the corneocytes, as follows from high resolution studies [12]. A characteristic minimum in local drug concentration is found near the stratum granulosum, indicating that tight junctions are a further barrier for drug penetration [14], as was analyzed in detail by a transport model [13]. Beyond the viable skin the drug is only found in the viable

* Corresponding author.

https://doi.org/10.1016/j.ejpb.2019.03.006
Received 24 September 2018; Received in revised form 4 January 2019; Accepted 4 March 2019
Available online 06 March 2019
0939-6411/

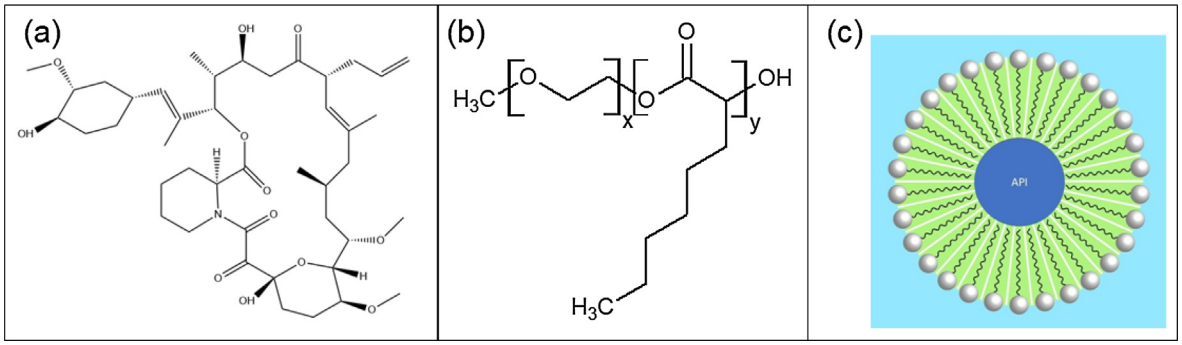

Scheme 1. (a) Structure of tacrolimus (taken from Ref. [26]); (b) structure of the polymer forming micelles for transporting tacrolimus (x ≃ 40–50 units, y ≃ 20–30 units)); (c) structure of a micelle incorporating the active pharmaceutical ingredient (API) tacrolimus (hydrodynamic diameter ~30 nm), where hydrophobic polymer chains point toward the inside and hydrophilic polymer chains toward the outside of the micellar corona.

epidermis, hinting that the basal membrane is another barrier impeding drug permeation to the dermis. In addition, stratum corneum removal by repeated tape stripping yielded an enhanced drug penetration behavior, which is due to the thinned stratum corneum. As a result, the drug penetrated in shorter time into deeper skin layers [12]. In addition, the drug transport was modified by core-multishell nanocarriers, which transport dexamethasone more slowly through the stratum corneum and release the drug in the lower part of this top skin layer [15]. As a result, less drug is contained in the stratum corneum and the drug is transported in larger local concentrations into the viable epidermis. Interestingly, the nanocarriers remained in the stratum corneum and were not able to cross the tight junction zone. Similar findings were reported from labeled nanocarriers, which were probed by fluorescence microscopy [16]. Even in inflamed skin of murine models of psoriasis or atopic dermatitis the nanocarriers remained in the stratum corneum [17,18].

These previous findings provide the motivation for the herein presented work. We have modified the experimental parameters as follows: instead of dexamethasone we chose the higher molecular weight drug tacrolimus ($C_{44}H_{69}NO_{12}$; m = 804.02 g/mol, see Scheme 1(a), which is efficiently used in atopic dermatitis [19] and psoriasis [20] treatment. The strongly hydrophobic compound with a log*P* of 3.96 ± 0.83 [21] is known to be difficult to formulate and penetrates only in small quantities into human skin [22]. For this reason, tacrolimus was formulated in micelles, which considerably increased the aqueous solubility from 2.5 µg/mL to 7 mg/mL, i.e. by a factor of > 3000. Maximum micellar loading was targeted to increase the chances of detecting tacrolimus by X-ray spectroscopy. The dermal penetration of tacrolimus formulated in these micelles has been investigated before, where it was shown that the formulation changes the drug penetration profile at low spatial resolution of 20 µm, as assessed by analytical approaches, such as ultrahigh pressure liquid chromatography with tandem mass spectrometry detection [23]. The result of this study was that a higher amount of tacrolimus was found mainly in the stratum corneum and up to the superficial dermis, if micelles containing the drug were used, as compared to the commercial Protopic® formulation. Subsequent work on skin delivery of a tacrolimus composite containing hydrogel in an imiquimod-induced psoriasis mouse model yielded a twice higher drug concentration than the commercial formulation Protopic®, which was also used as a benchmark in this study [22]. These promising earlier findings of efficient tacrolimus delivery into the skin motivated the present investigation of micellar penetration capacity via soft X-ray microscopy. Alternatively, transferosomes have been employed for efficient delivery of tacrolimus [24]. Most recently, various delivery strategies for tacrolimus have been reviewed [25]. In this work we exposed inflamed murine skin to a formulation containing tacrolimus embedded in micelles for determining the penetration of these species (cf. Scheme 1). This includes the aspect of enhanced drug penetration due to skin inflammation and the novel formulation of this lipophilic drug. It is known that imiquimod-induced psoriasis-like skin lesions lead to enhanced skin permeability and drug penetration for both hydrophilic and hydrophobic drugs [4]. This also includes tacrolimus, which showed an about ten-fold increased flux in psoriatic skin compared to murine healthy skin.

2. Materials and methods

Tacrolimus (TAC) > 99% (cf. Scheme 1(a)) was purchased from LC Laboratories (Woburn, MA, USA). Sodium citrate dihydrate and anhydrous citric acid Ph. Eur. grade were purchased from Haenseler (Herisau, Switzerland). Methoxy poly(ethylene glycol) hexyl-substituted poly(lactic acid) (mPEGhexPLA or methoxy PEG poly(caprylic acid)) (molecular weight: 5.5 kDa) was supplied by Apidel SA, Geneva, Switzerland. Acetonitrile HPLC grade (HPLC: high pressure liquid chromatography), water HPLC grade (Biosolve®), and sterile water (Corning®) were obtained from Brunschwig (Basel, Switzerland). Acetone Ph. Eur., trifluoroacetic acid (TFA, HPLC grade) were purchased from Sigma, Buchs, Switzerland.

Placebo and 0.7% TAC-mPEG hexyl-substituted poly(lactic acid) micellar formulations (cf. Scheme 1(b) and (c)) were prepared in citrate buffer at a 5 mL batch scale. Briefly, tacrolimus and polymers were dissolved in a 1:15 ratio (tacrolimus: polymer, w/w) in 2 mL of acetone. This organic phase was added dropwise (6 mL/h) to the citrate buffer (20 mM, pH 5.5) under sonication (amplitude 20%, SD450, Branson, USA). Acetone was evaporated under reduced pressure (60 °C, 180 mbar, Rotavapor R210, Buechi, Switzerland) and the final volume of the formulation was controlled to ensure the correct tacrolimus dose. Placebo mPEG hexyl-substituted poly(lactic acid) micellar formulations were prepared accordingly, but without tacrolimus. Finally, the micelles were filtered under a laminar flow hood through 0.22 µm polyvinylidene fluoride (PVDF) filters into sterilized vials and kept at 5 °C. The preparation of the micelles was adapted from Gabriel et al. [22].

The formulations were characterized in terms of drug content, micelle size, and pH. The tacrolimus content was quantified by high pressure liquid chromatography (HPLC, Agilent 1100, Basel, Switzerland) with a Kinetex Phenomenex® XB-C18 column (75 × 3 mm I.D., 2.6 µm) heated to 50 °C. The analysis was carried out in gradient mode at a flow rate of 1 mL/min over 7 min. The mobile phase consisted of a mixture of water with 0.1% (v/v) TFA (A) and acetonitrile with 0.1% (v/v) TFA (B). A linear gradient from 45% to 55% B was applied for 4 min, followed by 2 min at 55% B and an equilibration step down to 45% B in 1 min. The injection volume was set to 20 µL and UV detection was performed at 205 nm. The particle size was characterized by dynamic light scattering using back scattering light (173°) with a Zetasizer Nano-ZS (Malvern Instruments, UK). Micelle size and distribution were measured in triplicates and expressed as number weighted (d_n) and intensity weighted (Z-average, Z_{av}) hydrodynamic diameters and polydispersity index (PDI). The Z_{av} of both the

tacrolimus-loaded and neat micelles was around 30 nm and the target load with tacrolimus was 0.7%.

Murine skin with imiquimod-induced psoriasis-like dermatitis gathered in an *in vivo* experiment was used for these *ex vivo* experiments, as described by Pischon et al. [17]. The frozen skin samples were stored at −80 °C and were thawed for these studies and warmed to 37 °C before incubation. Neat and tacrolimus-loaded micelles and 0.1% Protopic® were exposed to murine skin so that all samples were treated topically with a drug concentration of 437 μg/cm^2 at 37 °C, i.e. the following samples were prepared: (i) reference skin treated for 100 min with physiological NaCl solution; (ii) 0.1% Protopic® (100 min penetration time); (iii) neat micelles (100 min, 105 mg polymer per mL citrate buffer 20 mM); (iv) tacrolimus loaded micelles (10 min penetration time); (v) tacrolimus loaded micelles (100 min penetration time); and (vi) tacrolimus loaded micelles (1000 min penetration time). Each skin sample had a size of 0.8 cm × 0.8 cm, then 10 μL of the drug formulations was applied to the skin surface covering an area of ca. 0.4 cm × 0.4 cm. After treatment, the samples were cut into 1 mm × 2 mm pieces and were fixed in 2.5% glutaraldehyde (30 min at room temperature and overnight at 4 °C). Subsequently, the samples were embedded using the standard protocol also applied in previous works [11,12,15]. Briefly, the samples were post-fixed by 1% OsO_4 and 0.8% $K_4[Fe(CN)_6]$ in 0.1 M cacodylate buffer. Dehydration of the samples was done by a sequence of washing steps in water-ethanol mixtures, finally using neat ethanol. Subsequently, the samples were embedded in EPON resin (Serva, Heidelberg, Germany). An ultramicrotome (Ultracut E, Leica, Germany) was used for preparing ca. 350 nm thick skin slices by cutting the skin samples vertically to the surface. The fixed skin slices were prepared in duplicates and were finally deposited on silicon nitride windows (thickness 100 nm, Silson, Northampton, U.K.). All samples were characterized by optical microscopy prior to X-ray microscopy studies (Leica DM4000M, equipped with a Heidenhain linear encoder).

The experiments involving X-ray microscopy were performed at the Swiss Light Source at the PolLux instrument, which is located at a bending magnet providing linearly polarized soft X-rays between 270 eV and 1600 eV [27–29]. The energy scale was calibrated by using dexamethasone, which has been investigated in detail before [11,12,15]. The fixed skin samples were mounted vertically on a high-precision piezoelectric stage and scanned horizontally in the fly scan mode, so that each line scans a depth profile. The vertical direction is step-scanned, yielding two-dimensional xy-raster images. A Fresnel zone plate was used as focusing optics to generate high spatial resolution (~40 nm at the C 1s-edge and ~80 nm at the O 1s-edge) by geometrical demagnification of the exit slit. The transmitted signal was collected by using a small-area detector, consisting of a phosphor screen, which was coupled to a photomultiplier tube (Hamamatsu 647P). The instrument was operated under vacuum (10^{-3} mbar) for minimizing X-ray absorption by residual gas and to avoid sample contamination. Images were recorded at selected photon energies below and in the C 1s regime (270–320 eV) as well as below and in the O 1s regime (500 eV and 550 eV). Image processing was carried out using IgorPro software similar to previous work [12,13,15] as well as aXis2000 [30], and Origin® 2018b.

3. Results and discussion

Fig. 1(a) shows the absorption spectrum of the species under study in the C 1s regime. This is required for gaining the chemical selectivity by X-ray microscopy. These spectra have not been reported before, so that they are briefly discussed. Note that the absorption spectra were left on a relative scale, but these can be easily converted into an absolute cross section scale by using the atomic absorption cross section, if the composition of the species under study is known, i.e. tacrolimus ($C_{44}H_{69}NO_{12}$, m = 804.02 g/mol) and the polymer composing the micelles ($C_{289}H_{454}N_2O_{94}$, M = 5454 g/mol, cf. [23]), e.g. at 310 eV, i.e. a region, in which no resonant transitions occur. This yields for tacrolimus at 310 eV a value of 38.9 ± 0.5 Mbarn (cf. Fig. 1(a)), if the pre-edge value at 280 eV is set to 0 Mbarn. For the micelles one derives at 310 eV a larger value of 337.7 ± 1 Mbarn (cf. Fig. 1(a)). These substantial cross sections, corresponding at the C 1s → π* transition of the micelles to 25 Mbarn and for tacrolimus to 16 Mbarn, are advantageous for the detection of topically applied substances, since these are roughly by a factor of 2.5–4 higher than at the O 1s-edge, as reported in earlier studies [11,12].

This is a clear advantage of the instrument at the Swiss Light Source which barely shows any contamination of the X-ray microscope and the beamline in the C 1s regime (cf. ref. [31]), specifically if compared to other X-ray microscopy installations. The chemical composition of fixed skin is not exactly known, so that the conversion into an absolute vertical scale may lead to substantial errors (cf. Fig. 1(a)). For the tacrolimus-loaded micelles (see Fig. 1(a)) one expects a similar C 1s-spectrum compared to neat micelles, since the drug loading is estimated to be of the order of 0.7% (see above). As a result, tacrolimus will not significantly affect the spectral shape of the tacrolimus-loaded micelles.

The assignment of the spectral features shown in Fig. 1(a) is straightforward according to the molecular structure of the absorbing carbon in all species under study [32,33]. Note that detailed assignments require quantum chemical calculations (cf. Ref. [11]), which go beyond the scope of this work. The distinct resonance located for tacrolimus at 284.58 eV is due to the C 1s → π* resonance of the C═C bonds, of which there are three in tacrolimus (see Scheme 1(a)). The shoulder near 286.6 eV is most likely due to the C 1s → π* resonance of the C═O bonds. The distinct features near 290 eV are likely due to σ*(C−H) excitations [33]. At slightly higher energy, i.e. near 293 eV, one expects the σ*(C−O)- and σ*(C−C)-excitations, whereas the σ*(C−C)-excitations occur as broad and weak features above 300 eV. The C 1s absorption spectrum of the micelles is similar in shape, but there are small differences in absorption energies, such as that the weak C → π*-resonance peaks at slightly higher energy than for tacrolimus, i.e. at 285.0 eV. This weak absorption is unexpected, since the absorption due to the C 1s → π* resonance of the C═O bonds is expected to occur at higher photon energy (see above) and might be a result of radiation damage, which may occur for radiation sensitive carboxylic groups, even at the moderate photon flux of the PolLux beamline. Note that there is no shift in absorption energy compared to fixed murine skin (see Fig. 1(a)), so that we cannot use the same approach that was successfully applied for probing dexamethasone in fixed human skin, where a distinct spectral shift of the O 1s → π* resonances of skin and the drug allowed us to selectively probe the drug [11,12]. However, in the present case it appears to be possible to use two photon energies at which there is a change in differential absorption primarily for the micelles, but not for fixed skin. These photon energies are found at 284.6 eV and 286.7 eV, respectively. There, the micelles gain absorption cross section by 350 ± 5%, whereas for tacrolimus a drop in cross section 23 ± 5% is observed. This implies that changes in absorption cross section due to topically applied micelles can be selectively probed in the C 1s-regime, but not for tacrolimus.

The O 1s absorption regime is shown in Fig. 1(b) for the same samples discussed for the C 1s regime (cf. Fig. 1(a)). The assignments are similar to those given above for the C 1s features with the difference that only oxygen sites are excited. The intense resonances peaking near 531 eV are due to the O 1s → π* transition. The broad feature near 540 eV is assigned to the O 1s → σ* transition. Note that the O 1s absorption cross section is significantly smaller than that at the C 1s-edge, which is only used in this work for supplementary studies, such as probing tacrolimus.

Fig. 2 shows a series of X-ray micrographs from the top skin layers of inflamed murine skin. These were recorded in the C 1s regime in order to detect the presence and penetration of polymeric micelles after exposure of the skin samples to topically applied substances for 100 min. Fig. 2(a)–(d) shows a series of images taken at 286.7 eV. This photon

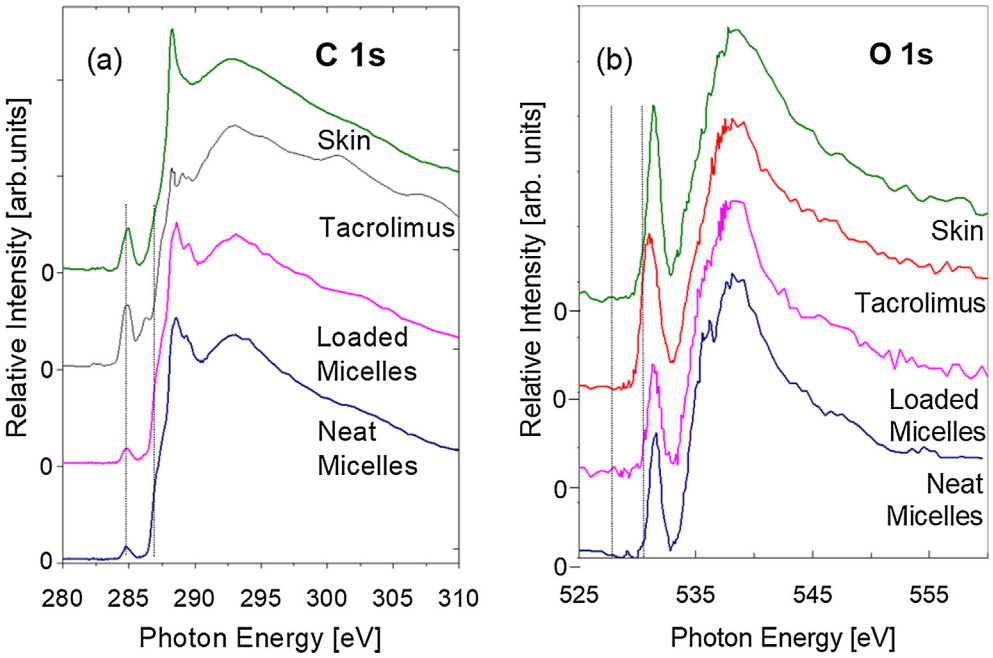

Fig. 1. (a) Carbon 1s absorption cross section of fixed murine inflamed skin; tacrolimus; tacrolimus loaded micelles; and neat micelles. The vertical dashed lines at 284.6 eV and 286.7 eV correspond to the excitation energies used for X-ray microscopy studies; (b) Oxygen 1s absorption cross section of fixed murine inflamed skin; tacrolimus; tacrolimus loaded micelles; and neat micelles. The vertical dashed lines at 528.0 eV and 530.3 eV correspond to the excitation energies used for X-ray microscopy studies.

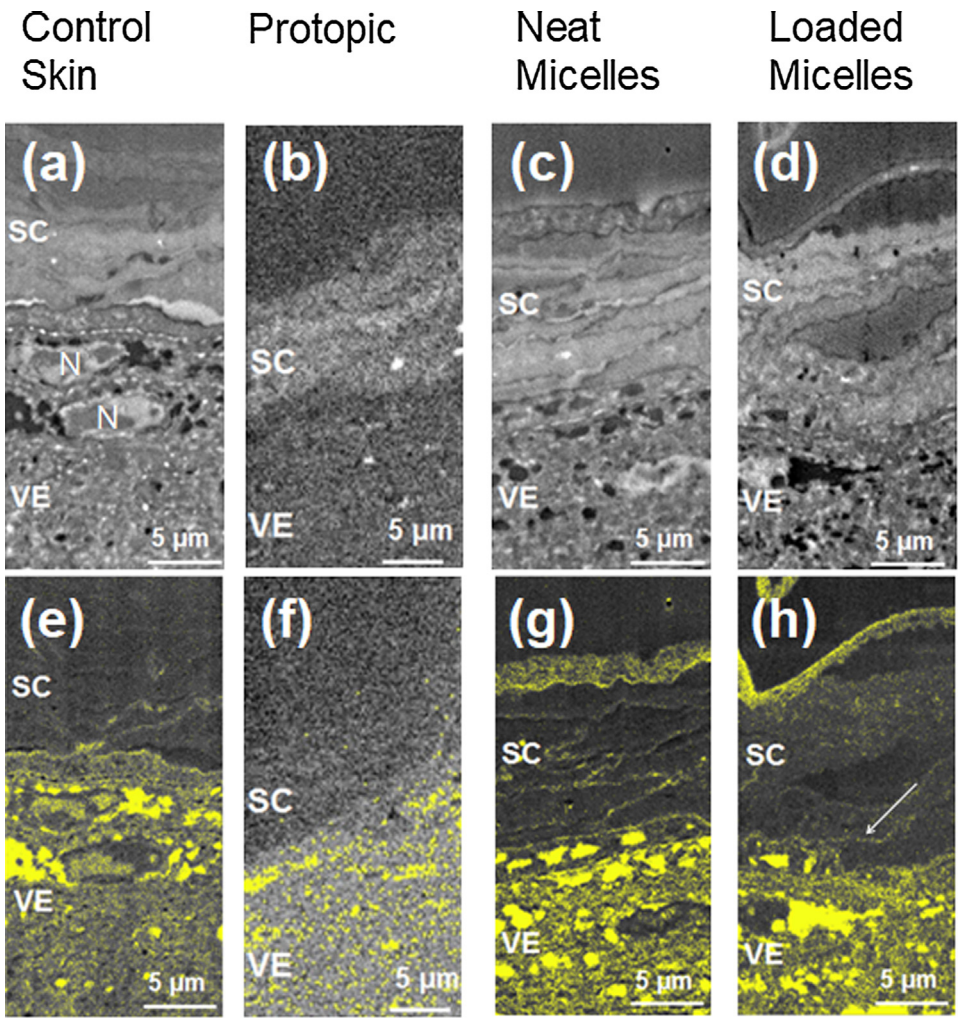

Fig. 2. X-ray micrographs of murine inflamed skin near the skin surface: SC: stratum corneum, VE: viable epidermis, N: nucleus. The micrographs (a)–(d) have been taken at 286.7 eV for determining the structure of the samples: (a) control skin; (b) skin treated with Protopic®; (c) skin treated with neat micelles; (d) skin treated with tacrolimus loaded micelles. The micrographs shown in the lower row (e)–(h) are derived from changes in optical density between 284.6 eV and 286.7 eV for probing efficiently micelles. Changes in optical density above a common threshold value in relative optical density of 0.067 are indicated by yellow color, similar to previous work [15]. The arrow in (h) points toward enhanced concentration of micelles at the border to the viable epidermis. Note that similar features also occur in (e) and (g). The scale bars correspond to 5 µm. Note that all micrographs were taken with 50 nm step widths, except for (b) and (f), where 200 nm were chosen. See text for further details.

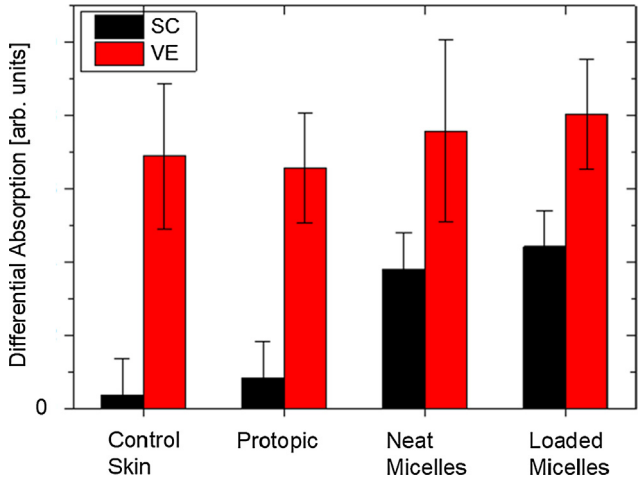

Fig. 3. Changes in differential absorption for probing micelles by X-ray microscopy in different skin layers and differently treated skin samples for 100 min as indicated. The error bars correspond to the variance of the corresponding signal levels, where a quarter of the respective region was evaluated. Stratum corneum (SC) and viable epidermis (VE) – see text for further details.

energy corresponds to the onset of the C 1s continuum (cf. Fig. 1(a)) for all topically applied substances as well as fixed murine skin.

Each micrograph shows the stratum corneum with distinct layers of corneocytes besides the top part of the viable epidermis. Specifically, Fig. 2(a)–(d) shows the structural properties of the skin samples. In contrast, the images in Fig. 2(e)–(h) indicate the presence of micelles at detectable levels. The distinct layers in the stratum corneum have typically a thickness of 1.6 µm and appear to be swollen due to the topical application of NaCl solution (Fig. 2(a)), Protopic® (Fig. 2(b), neat micelles (Fig. 2(c)), and tacrolimus loaded micelles (Figure (2d)). Below these structures lies the viable epidermis, showing sections of keratinocytes with nuclei (partially indicated by N, e.g. in Fig. 2(a) – see also Fig. 2(e)–(h)) and provides the chemical contrast due to selective excitation at 284.6 eV and 286.7 eV, respectively. These energies were chosen in order to have the same absorption contrast for fixed skin, while for the other samples, i.e. micelles and tacrolimus-loaded micelles, an increase in absorption cross section leads to an enhancement of the differential absorption. We have chosen a presentation for these Figures that is similar to previous work (cf. Ref. [15]) in order to visualize the topically applied species under study. This means that a common threshold value of 0.067, as derived from the relative optical density scale, is used at which the gray scale image turns into yellow color of increased differential absorption. This shows a constant background in the viable epidermis for all micrographs (see Fig. 2(e)–(h)), which is not considered for the present analysis. We assume that these highlighted structures are due to carbon-rich moieties in the upper part of the viable epidermis, which can be assigned to granular and lamellar patterns according to electron microscopy studies [34,35]. Note that these occur only in the stratum granulosum and below, but not in the stratum corneum, yielding a chemical contrast, which is similar to the topically applied substances under study. Caprylic acid, which is a chemical building block of the micelles' polymer, is a fatty acid. High prevalence of lipids, which are endogenously present in the skin, might be the reason for signal interference in the viable epidermis. For example, lipid species that have been detected particularly in the epidermis, but not in the stratum corneum, are phosphatidylcholins [36].

In Fig. 2(a) and (e) it is also evident that cell nuclei in the stratum granulosum, indicated by N, are barely affected by this cross sensitivity. Despite this cross sensitivity in the viable epidermis, it is possible to probe topically applied drug formulations in the stratum corneum. This means that the stratum corneum of the reference skin sample does not show any enhanced absorption contrast in the top of this skin layer. Furthermore, Protopic® (cf. Fig. 2(b) and (f)) does not show any hint for tacrolimus penetration, implying that only small quantities can penetrate, which are evidently below the detection limit, if probed in the C 1s-regime. However, the skin samples exposed to micelles display much higher signals in the stratum corneum. As noted above, the sensitivity is significantly higher for probing micelles as compared to tacrolimus. Neat micelles show evidence of their penetration most intensely in a narrow range at the top of the stratum corneum (see Fig. 2(c) and (g)). Here, the entire corneocytes in the top layer appear to have taken up the formulation. The corneocytes show a thickness of 1.8 ± 0.2 µm, which is thicker than in untreated murine skin [37]. Thus, it is assumed that the corneocytes are swollen due to topical treatment. In the lower layers of the stratum corneum one observes, as indicated by yellow color, the micelles preferably at the edges of corneocytes. This hints that their penetration is mostly due to transport in the lipophilic lamellae [38], as is known to occur for hydrophobic low molecular weight drugs [12]. Swelling of corneocytes is known for topical application of polymeric nanogel formulations, e.g. from thermoresponsive nanogels [39]. When exposed to micelles loaded with tacrolimus, the following changes are observed: The top layer of the stratum corneum contains also most of the topically applied species, but the load in lower parts of the stratum corneum shows a different signature compared to the neat micelles. In the case of the drug-loaded micelles one observes a more delocalized signal distribution with lower relative concentration (see Fig. 2(d) and (h)). Localized structures at the edges of corneocytes only occur in deeper layers of the stratum corneum, as indicated by the white arrow in Fig. 2(h). The delocalized signal in the stratum corneum shown in Fig. 2(h) may indicate the disintegration of some micelles in superficial skin layers and their ability to diffuse down and accumulate in the stratum granulosum. At the same time, the micelles might be able to carry with them the drug into layers below the superficial stratum corneum, as previously reported [23].

Fig. 3 summarizes the findings after 100 min penetration time as follows: Integrated intensities of the different layers, i.e. stratum corneum (SC) and viable epidermis (VE) are added, yielding an averaged response due to changes in differential absorption between 286.7 eV and 284.6 eV, respectively, where the differential absorption of fixed murine skin cancels out. The control skin and the Protopic® treated samples show a minor response in terms of differential absorption in the stratum corneum. In contrast, the response is significantly higher for neat micelles and tacrolimus loaded micelles, indicating the feasibility to show the presence of micelles in the stratum corneum. In contrast, differential absorption is almost the same for control and viable epidermis treated with Protopic®, neat micelles, and tacrolimus loaded micelles. This implies that penetration of micelles into the viable epidermis cannot be evidenced by this technique. However, it is assumed in accordance with previous studies that they will not penetrate into this skin layer [15]. Additionally, the role of tacrolimus cannot be fully derived from these experiments, since the drug shows at the chosen photon energies even a drop in differential absorption, as displayed in Fig. 1(a).

In comparison to previous work on polymeric micellar nanocarriers transporting tacrolimus these results are fully compatible [23]. Core-multishell nanocarriers were found to remain in the stratum corneum and there was no or minimal penetration into deeper layers observed. This was also the case for topically applied thermoresponsive nanogels [39], indicating the necessity of small sized nanocarriers and specific physicochemical properties in order to cross the skin barriers. As a result, this type of drug delivery is ideally expected to minimize the systemic exposure to the drug.

Fig. 4 shows the temporal skin penetration behavior in samples treated with loaded micelles, as probed by an increase in differential absorption in the stratum corneum. We have taken X-ray micrographs for three penetration times, i.e. at 10 min, 100 min, and 1000 min.

The presence of micelles was evidenced in the stratum corneum at 100 min and 1000 min. Clearly, only a minor signal from the micelles is

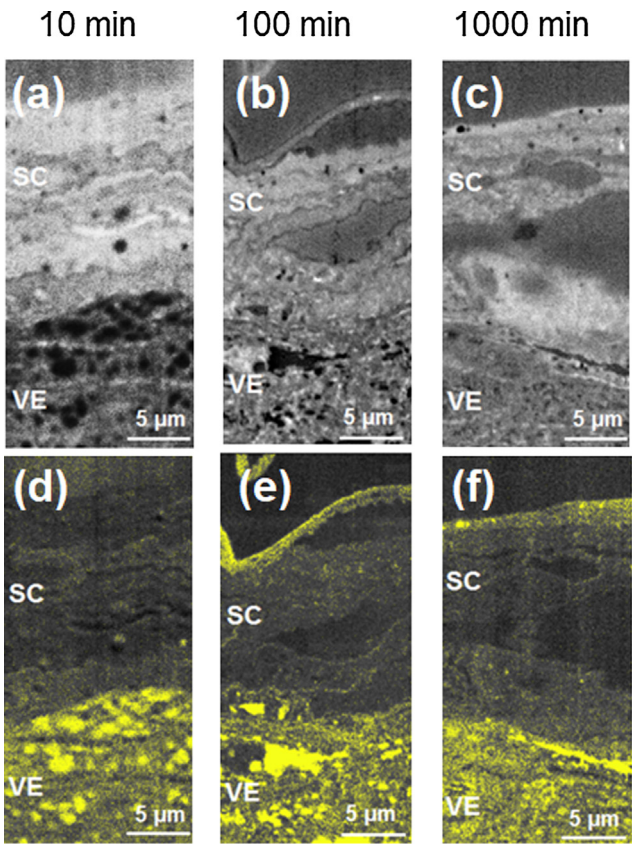

Fig. 4. X-ray micrographs of inflamed murine skin near the skin surface: SC: stratum corneum, VE: viable epidermis. The micrographs (a)–(c) have been taken at 286.7 eV for determining the structure of the samples: (a) skin treated for 10 min. penetration time with tacrolimus loaded micelles; (b) 100 min penetration time; (c) 1000 min penetration time. The micrographs shown in the lower row (d)–(f) are derived from changes in optical density, i.e. at 284.6 eV and 286.7 eV, probing mostly micelles. Changes in optical density above a common threshold value are indicated by yellow color. Note that all micrographs were taken with 50 nm step widths. See text for further details.

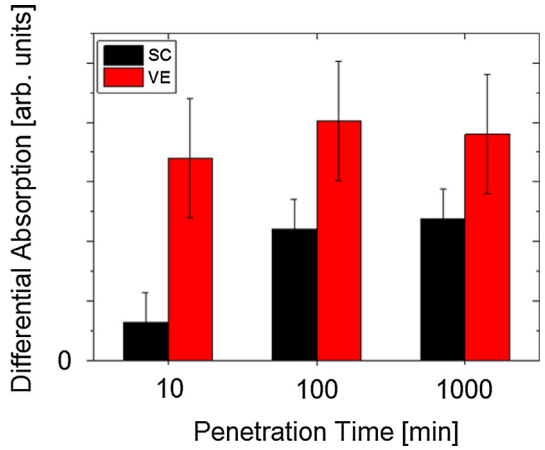

Fig. 5. Changes in differential absorption in the top skin layers of tacrolimus loaded micelles as a function of penetration time. The error bars correspond to the variance of the corresponding signal levels, where a quarter of the respective region was evaluated. Stratum corneum (SC) and viable epidermis (VE) – see text for further details.

detected in the stratum corneum after 10 min penetration time. This is indicated by light yellow color in Fig. 4(d). Most of the intensity is observed even above the stratum corneum in the top part of this image (not shown in Fig. 4(d)). The measurements taken at 100 min are identical to those shown in Fig. 2(d) and (h). As the penetration time is increased to 100 min, an intense signal is observed in the entire top layer of corneocytes, implying that this layer has absorbed the drug formulation (cf. Fig. 4(e)). This situation is similar, but more delocalized after 1000 min. penetration time, as displayed in Fig. 4(f). This might indicate the disintegration of the micelles and release of tacrolimus into the tissue. A quantification of these results cannot be done from the micrographs, which is due to the low signal strength. Therefore, the relative intensities of the micelles in the stratum corneum have been derived from the results shown in Fig. 4, where cross sensitivities in the viable epidermis impede the analysis below the stratum corneum. The results are shown in Fig. 5. The differential absorption due to micelles increases in the stratum corneum (black bars) with time, whereas the intensity in the viable epidermis (red bars) remains almost constant. This leads to the conclusion that the temporally resolved loading of the stratum corneum appears to go into saturation for penetration times above 100 min. Such penetration behavior will ensure safety due to a rate-limited drug uptake by the skin.

A limitation of these results is that one cannot distinguish between neat micelles, tacrolimus loaded micelles, and tacrolimus on the X-ray micrographs shown in Figs. 2 and 4 with the C 1s probing technique. As pointed out above, there is an increase in absorption for the micelles, providing the chemical contrast in the X-ray micrographs, whereas for tacrolimus there is even a slight drop in absorption, if the photon energies at 284.6 eV and 286.7 eV are used. This is, however, not suitable for detecting tacrolimus via resonant excitation in the C 1s-regime and requires probing the drug in the O 1s-regime (cf. Fig. 1(b)). There, tacrolimus shows an O 1s $\rightarrow \pi^*$ resonance, which is positioned at slightly lower energy than the other species under study. This allows us to selectively probe the drug in fixed murine skin. The differential absorption is adjusted at 528.0 eV (pre-edge regime) and at 530.3 eV (slope of the O 1s $\rightarrow \pi^*$ transition (cf. vertical lines in Fig. 1(b)). There, the cross sensitivity is as small as possible, while the absorption cross section is appreciably high, corresponding to 12.0 ± 0.5 Mbarn, if the atomic absorption cross section in the O 1s-continuum is used (see above). This results from a chemical shift in the different species under study near the carbonyl groups. It is rationalized as follows: A careful examination of the O 1s absorption spectra shown in Fig. 1(b) indicates the O 1s $\rightarrow \pi^*$(C═O) peak of tacrolimus is shifted to lower energy by ~0.5 eV relative to the π^* peak in the other systems under study. This is consistent with the carbonyl groups (C═O) being attached to two neighboring carbon atoms in the drug (see Scheme 1), whereas in the head group of micelles the C═O is attached to a C and an O, while in skin protein the C═O is attached to C and N. The use of 530.3 eV photon energy probes selectively tacrolimus by exploiting this chemical shift. Then, one can derive for the samples under study the differential absorption, which also shows a background due to cross sensitivities of the majority species in the skin samples.

Fig. 6 clearly indicates that there is a distinct difference in differential absorption in the stratum corneum, providing evidence that tacrolimus is probed with weak intensity. Skin areas were selected, where the thickness of the stratum corneum is similar. Local differences in structure of stratum corneum were not dominant in these areas, so that defects, e.g. holes, cracks etc. were not included in the analysis. In these selected areas, single images were split into three small longitudinal sub-sections (sub-images) that were evaluated individually. The total mean value (column height) of the total sample was derived from the three mean values of the individual sub-images. The limits of the error bars correspond to the minimum/maximum of all three sub-images. In addition, selected areas of the skin were analyzed for evaluating the robustness of the analysis with respect to large defects, e.g. the longitudinal section containing the area of the two large holes shown in Fig. 2(d) and (h). There, no significant difference compared to the area left of these holes is observed. Evidently, the analysis does not respond to the holes containing primarily EPON resin. It can therefore be

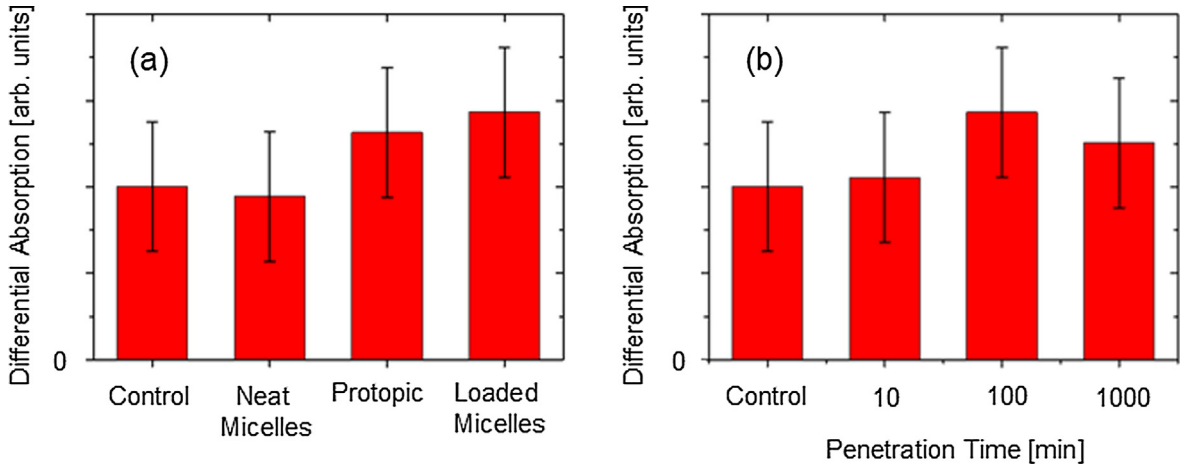

Fig. 6. Changes in differential absorption in the stratum corneum due to tacrolimus probed at the O 1s-edge relative to a untreated control sample (cf. Fig. 1(b)): (a) Changes in differential absorption for samples exposed for 100 min to neat micelles, Protopic®, and tacrolimus loaded micelles; (b) temporal evolution of the tacrolimus load in the stratum corneum after delivery with tacrolimus loaded micelles – see text for further details. The error bars correspond to the variance of the corresponding signal levels, where a quarter of the respective region was evaluated.

concluded that the chosen approach yields realistic results. A lower level of differential absorption is obtained from the control sample and the skin sample containing neat micelles (see Fig. 6(a)), whereas an enhanced level is obtained from the Protopic® sample, which is at least similar, likely even slightly higher for the tacrolimus loaded micelles. This underscores the previously noticed favorable penetration of tacrolimus, if formulated in micelles rather than in Protopic® [22,23]. We note that the drug load is lower in the viable epidermis, so that this analysis is not extended to this skin region. We have rather evaluated the time-resolved measurements, as shown in Fig. 6(b).

The O 1s probing technique allowed for following tacrolimus levels in the stratum corneum as a function of penetration time. The same level of differential absorption is observed for the control sample and 10 min penetration time. This means that tacrolimus has not yet penetrated into the stratum corneum. There is an increase of tacrolimus levels at 100 min penetration time, with slightly decreasing levels at 1000 min. The local concentration of tacrolimus might have dropped in superficial layers due to transport into deeper skin layers, but this remains speculative at this point. Due to rate-limited drug uptake by the skin, drug concentrations might remain at safe, but active levels in a considered volume.

4. Summary and conclusions

X-ray microscopy has been applied for the first time to follow the penetration of tacrolimus in inflamed murine skin *ex vivo*. Element selective excitation allowed us to probe the penetration of the drug and micelles in the top skin layers, where C 1s-excitation is preferable for probing the micelles and O 1s-excitation is more suitable for probing tacrolimus. The local concentration of the drug and micelles is weak in the stratum corneum, but at least on the same level compared to Protopic®, a commercial formulation. The present results indicate that the corneocytes are swollen and penetrated by the drug formulation, but there is also minor evidence for enhanced concentration near the lipid lamellae between the corneocytes. Additional time-resolved studies indicate that the local concentration of micelles and tacrolimus in the stratum corneum is increasing with time and reaching finally saturation.

Note that earlier studies with the same tacrolimus loaded micelles showed efficient, significantly superior tacrolimus delivery compared to Protopic® into murine, porcine, and human skin [22,23]. The micelles were therefore considered a suitable delivery system for tacrolimus, which was able to significantly increase the cutaneous drug levels, and for this reason merited further investigation. There are noticeable differences, if X-ray microscopy is used for high spatial resolution analysis with chemical selectivity. These can be due to the efficiency for selective probing of the drug and micelles by tunable X-rays as well as the local deposition of the topically applied species, which were investigated for the first time in this study. Thus, subsequent studies are suggested for explaining the evident differences between these experimental approaches.

Acknowledgements

We gratefully acknowledge financial support by DFG within SFB 1112 (projects B02, C03, C04) and project RU420/12-1. The PolLux end station was financed by the German Bundesministerium für Bildung und Forschung (BMBF) through contracts 05KS4WE1/6 and 05KS7WE1.

References

[1] A. Gysler, B. Kleuser, W. Sippl, K. Lange, H.C. Korting, H.D. Höltje, M. Schäfer-Korting, Skin penetration and metabolism of topical glucocorticoids in reconstructed epidermis and in excised human skin, Pharm. Res. 16 (1999) 1386–1391.
[2] D. Selzer, M.M.A. Abdel-Mottaleb, T. Hahn, U.F. Schaefer, D. Neumann, Finite and infinite dosing: difficulties in measurements, evaluations and predictions, Adv. Drug. Del. Rev. 65 (2013) 278–294.
[3] J.D. Bos, M.M.H.M. Meinardi, The 500 Dalton rule for the skin penetration of chemical compounds and drugs, Exp. Dermatol. 9 (2000) 165–169.
[4] Y.K. Lin, S.H. Yang, C.C. Chen, H.C. Kao, J.Y. Fang, Using imiquimod-induced psoriasis-like skin as a model to measure the skin penetration of anti-psoriatic drugs, Plos One 10 (2015) e0137890.
[5] E. Rühl, Probing functionalized nanoparticles in biological media, in: K. Wandelt (Ed.), Encyclopedia of Interfacial Chemistry, Elsevier, Oxford, 2018, pp. 795–802.
[6] C.W. Freudiger, W. Min, B.G. Saar, S. Lu, G.R. Holtom, C. He, J.C. Tsai, J.X. Kang, X.S. Xie, Label-free biomedical imaging with high sensitivity by stimulated raman scattering microscopy, Science 322 (2008) 1857–1861.
[7] Q. Li, T. Zhang, Y. Pan, L.C. Ciacchi, B. Xu, G. Wei, AFM-based force spectroscopy for bioimaging and biosensing, RSC Adv. 6 (2016) 12893–12912.
[8] P. Verma, Tip-enhanced Raman spectroscopy: technique and recent advances, Chem. Rev. 117 (2017) 6447–6466.
[9] A. Danielli, K.I. Maslov, A. Garcia-Uribe, A.M. Winkler, C. Li, L. Wang, Y. Chen, G.W. Dorn, L.V. Wang, Label-free photoacoustic nanoscopy, J. Biomed. Opt. 19 (2014) 086006.
[10] A. Dazzi, C.B. Prater, AFM-IR: technology and applications in nanoscale infrared spectroscopy and chemical imaging, Chem. Rev. 117 (2017) 5146–5173.
[11] K. Yamamoto, R. Flesch, T. Ohigashi, S. Hedtrich, A. Klossek, P. Patoka, G. Ulrich, S. Ahlberg, F. Rancan, A. Vogt, U. Blume-Peytavi, P. Schrade, S. Bachmann, M. Schäfer-Korting, N. Kosugi, E. Rühl, Selective probing of the penetration of dexamethasone into human skin by soft X-ray spectromicroscopy, Anal. Chem. 87 (2015) 6173–6179.
[12] K. Yamamoto, A. Klossek, A. Flesch, F. Rancan, M. Weigand, I. Bykova, M. Bechtel, S. Ahlberg, A. Vogt, U. Blume-Peytavi, P. Schrade, S. Bachmann, S. Hedtrich,

M. Schäfer-Korting, E. Rühl, Influence of the skin barrier on the penetration of topically-applied dexamethasone probed by soft X-ray spectromicroscopy, Eur. J. Pharm. Biopharm. 118 (2017) 30–37.
[13] R. Schulz, K. Yamamoto, A. Klossek, R. Flesch, S. Hönzke, F. Rancan, A. Vogt, U. Blume-Peytavi, S. Hedtrich, M. Schäfer-Korting, E. Rühl, R.R. Netz, Data-based modeling of drug penetration relates human skin barrier function to the interplay of diffusivity and free-energy profiles, Proc. Nat. Acad. Sci. U.S.A. 114 (2017) 3631–3636.
[14] J.M. Brandner, Importance of tight junctions in relation to skin barrier function, Curr. Probl. Dermatol. 49 (2016) 27–37.
[15] K. Yamamoto, A. Klossek, R. Flesch, T. Ohigashi, E. Fleige, F. Rancan, J. Frombach, A. Vogt, U. Blume-Peytavi, P. Schrade, S. Bachmann, R. Haag, S. Hedtrich, M. Schäfer-Korting, N. Kosugi, E. Rühl, Core-multishell nanocarriers: Transport and release of dexamethasone probed by soft X-ray spectromicroscopy, J. Control. Release 242 (2016) 64–70.
[16] U. Alexiev, P. Volz, A. Boreham, R. Brodwolf, Time-resolved fluorescence microscopy (FLIM) as an analytical tool in skin nanomedicine, Eur. J. Pharm. Biopharm. 116 (2017) 111–124.
[17] H. Pischon, M. Radbruch, A. Ostrowski, P. Volz, C. Gerecke, M. Unbehauen, S. Hönzke, S. Hedtrich, J.W. Fluhr, R. Haag, B. Kleuser, U. Alexiev, A.D. Gruber, L. Mundhenk, Stratum corneum targeting by dendritic core-multishell-nanocarriers in a mouse model of psoriasis, Nanomed. Nanotechnol. 13 (2017) 317–327.
[18] M. Radbruch, H. Pischon, A. Ostrowski, P. Volz, R. Brodwolf, F. Neumann, M. Unbehauen, B. Kleuser, R. Haag, N. Ma, U. Alexiev, L. Mundhenk, A.D. Gruber, Dendritic core-multishell nanocarriers in murine models of healthy and atopic skin, Nanoscale Res. Lett. 12 (2017) 64.
[19] T. Ruzicka, T. Bieber, E. Schopf, A. Rubins, A. Dobozy, J.D. Bos, S. Jablonska, I. Ahmed, K. ThestrupPedersen, F. Daniel, A. Finzi, S. Reitamo, A short-term trial of tacrolimus ointment for atopic dermatitis, New Engl. J. Med. 337 (1997) 816–821.
[20] A. Menter, N.J. Korman, C.A. Elmets, S.R. Feldman, J.M. Gelfand, K.B. Gordon, A. Gottlieb, J.Y.M. Koo, M. Lebwohl, H.W. Lim, A.S. Van Voorhees, K.R. Beutner, R. Bhushan, Guidelines of care for the management of psoriasis and psoriatic arthritis Section 3. Guidelines of care for the management and treatment of psoriasis with topical therapies, J. Am. Acad. Dermatol. 60 (2009) 643–659.
[21] A.S.B. Goebel, R.H.H. Neubert, J. Wohlrab, Dermal targeting of tacrolimus using colloidal carrier systems, Int. J. Pharm. 404 (2011) 159–168.
[22] D. Gabriel, T. Mugnier, H. Courthion, K. Kranidioti, N. Karagianni, M.C. Denis, M. Lapteva, Y. Kalia, M. Möller, R. Gurny, Improved topical delivery of tacrolimus: a novel composite hydrogel formulation for the treatment of psoriasis, J. Control. Release 242 (2016) 16–24.
[23] M. Lapteva, K. Mondon, M. Möller, R. Gurny, Y.N. Kalia, Polymeric micelle nanocarriers for the cutaneous delivery of tacrolimus: a targeted approach for the treatment of psoriasis, Mol. Pharm. 11 (2014) 2989–3001.
[24] W. Lei, C. Yu, H. Lin, X. Zhou, Development of tacrolimus-loaded transfersomes for deeper skin penetration enhancement and therapeutic effect improvement in vivo, Asian J. Pharm. Sci. 8 (2013) 336–345.
[25] D. Dheer, Jyoti, P.N. Gupta, R. Shankar, Tacrolimus: an updated review on delivering strategies for multifarious diseases, Eur. J. Pharm. Sci. 114 (2018) 217–227.
[26] Drug Bank, in, https://www.drugbank.ca/drugs/DB00864, 2018.
[27] J. Raabe, G. Tzvetkov, U. Flechsig, M. Böge, A. Jaggi, B. Sarafimov, M.G.C. Vernooij, T. Huthwelker, H. Ade, D. Kilcoyne, T. Tyliszczak, R.H. Fink, C. Quitmann, PolLux: a new facility for soft X-ray spectromicroscopy at the Swiss light source, Rev. Sci. Instrum. 79 (2008) 113704.
[28] U. Flechsig, C. Quitmann, J. Raabe, M. Böge, R. Fink, H. Ade, The PolLux microspectroscopy beam line at the Swiss light source, AIP Conf. Proc. 879 (2007) 505–508.
[29] U. Frommherz, J. Raabe, B. Watts, R. Stefani, U. Ellenberger, Higher Order Suppressor (HOS) for the PolLux microspectroscope beamline at the swiss light source SLS, AIP Conf. Proc. 1234 (2010) 429–432.
[30] A.P. Hitchock, aXis 2000 – Analysis of X-ray Images and Spectra, McMaster University, Hamilton, Ont. Canada, 2018http://unicorn.mcmaster.ca/axis/aXis2000-windows-pre-IDL8.3.html.
[31] B. Watts, N. Pilet, B. Sarafimov, K. Witte, J. Raabe, Controlling optics contamination at the PolLux STXM, J. Instrum. 13 (2018) C04001.
[32] A.P. Hitchcock, D.C. Mancini, Bibliography and database of inner-shell excitation-spectra of gas phase atoms and molecules, J. Elem. Spectrosc. Relat. Phenom. 67 (1994) 1–132.
[33] J. Stöhr, NEXAFS Sepctroscopy, Springer, Berlin, 1992.
[34] A. Al-Amoudi, J. Dubochet, L. Norlén, Nanostructure of the epidermal extracellular space as observed by cryo-electron microscopy of vitreous sections of human skin, J. Invest. Dermatol. 124 (2005) 764–777.
[35] A. Narangifard, L. den Hollander, C.L. Wennberg, M. Lundborg, E. Lindahl, I. Iwai, H. Han, S. Masich, B. Daneholt, L. Norlén, Human skin barrier formation takes place via a cubic to lamellar lipid phase transition as analyzed by cryo-electron microscopy and EM-simulation, Exp. Cell Res. 366 (2018) 139–151.
[36] C.A. Mitchell, H. Long, M. Donaldson, S. Francese, M.R. Clench, Lipid changes within the epidermis of living skin equivalents observed across a time-course by MALDI-MS imaging and profiling, Lipids Health Dis. 14 (2015) 84.
[37] S.Y.E. Hou, A.K. Mitra, S.H. White, G.K. Menon, R. Ghadially, P.M. Elias, Membrane structures in normal and essential fatty acid-deficient stratum corneum: characterization by ruthenium tetroxide staining and X-ray diffraction, J. Invest. Dermatol. 96 (1991) 215–223.
[38] J.A. Bouwstra, P.L. Honeywell-Nguyen, G.S. Gooris, M. Ponec, Structure of the skin barrier and its modulation by vesicular formulations, Prog. Lipid Res. 42 (2003) 1–36.
[39] M. Giulbudagian, F. Rancan, A. Klossek, K. Yamamoto, J. Jurisch, V.C. Neto, P. Schrade, S. Bachmann, E. Rühl, U. Blume-Peytavi, A. Vogt, M. Calderon, Correlation between the chemical composition of thermoresponsive nanogels and their interaction with the skin barrier, J. Control. Release 243 (2016) 323–332.

3.5 Soft X-Ray Microsopy on Thermoresponsive Nanogels for Topical Application in Skin

Often, topical drug delivery is challenging when fighting inflammatory skin diseases. Drug penetration into the viable skin is successfully prevented by the stratum corneum. To enhance the drug penetration characteristics in skin, nanoscopic drug delivery systems can be used.[132,133] The available nanoscopic drug delivery systems for topical treatments are versatile.[7,9,89,93] Apart from micelles and core-multishell nanocarriers, thermoresponsive nanogels are considered for topical treatment of inflammatory skin diseases.[94,134] Thereby, important characteristics such as drug loading and the drug delivery towards the site of action are of high interest. In this Chapter scanning transmission X-ray microscopy was used to selectively probe the penetration characteristics of pNIPAM nanogel (see Chapter 2.3) and dexamethasone in skin.

Therefore, human abdominal skin was treated with 120 µL of the nanogel suspension per cm². The nanogel suspension was provided by our collaboration partners from the Freie Universität Berlin, Institute for Chemistry and Biochemistry, AG Calderón. The total amount of dexamethasone within the 120 µL nanogel suspension was 400 µg.

The skin samples were prepared and received from our collaboration partners at the Charité Universitätsmedizin, Dermatology, AG Vogt / Blume-Peytavi. Prior to treatment the barrier was disrupted by tape stripping (30 times). The samples were prepared with and without thermal triggering of the nanogel. Treatment for the triggered thermoresponsive nanogel was conducted as follows: after 10 min of incubation time at 30 °C samples were irradiated by IR radiation (Philips Infrared RI 1521, 30 s, 116.8 mW, 3.9 mJ/cm²). The measured sample temperature reaches then a range between 40 °C to 42 °C and exceeds the cloud point T_{CP} of 34 °C. Subsequently, the reported samples were incubated for further 100 min at 30 °C. After incubation, the non-penetrated nanogel suspension was removed by using cotton swabs. Samples were cut into 1 mm² pieces and fixed in 2.5% glutaraldehyde. For un-triggered thermoresponsive nanogel the procedure was similar, except for the triggering process. The samples were incubated for 10 min at 30 °C, the irradiation by IR radiation was skipped, and subsequently the samples were incubated for further 100 min at 30 °C. Thus, the temperature of the sample and skin was always kept below the cloud point T_{CP}.

The experiments were carried out at the Scanning Transmission X-ray Microscope setup located at the electron storage ring UVSOR III (Okazaki, Japan) as described in Chapter 2.4.

Measurements were conducted within the O 1s excitation regime ranging from approximately 525 eV to 560 eV.

To determine photon energies at which a selective excitation can be used to separate the drug from the thermoresponsive nanogel an X-ray absorption spectrum of the species at the oxygen 1s regime was measured. X-ray absorption spectrum of dexamethasone compared to the X-ray absorption spectrum of the nanogel and dexamethasone loaded nanogel is shown in Figure 3.5.1.

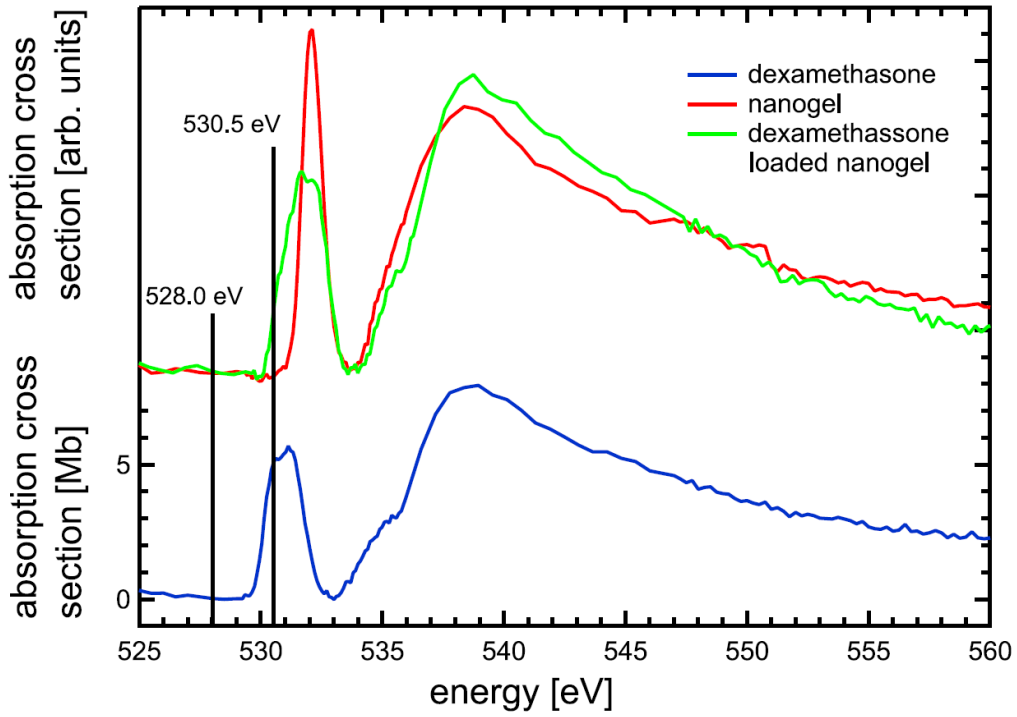

Fig 3.5.1: X-ray absorption spectrum of dexamethasone (blue) compared to the X-ray absorption of pNIPAM nanogel (red) and dexamethasone loaded nanogel (green). Excitation energies, chosen for the detection of dexamethasone, are highlighted by a black bar.

In previous work it was shown, that dexamethasone in human skin can be detected by X-ray microscopy when exciting the sample at 528.0 eV and between 530.1 eV to 530.6 eV photon energy.[13,36] From Figure 3.5.1 it is concluded that excitation energies of 528.0 eV and 530.5 eV are suitable to detect dexamethasone within the skin sample treated with dexamethasone loaded thermoresponsive nanogel. At 530.5 eV an increased absorption cross section for thermoresponsive nanogel itself is not observed, when compared to an excitation energy of 528.0 eV. Therefore, the impact of the nanogel to the optical density of human skin treated with the dexamethasone loaded nanogel, is avoided when exciting at 528.0 eV and 530.5

eV. The absorption spectrum of dexamethasone loaded nanogel shows a broadening of the O $1s \rightarrow \pi^*$ transition compared to the neat nanogel. From Figure 3.5.1 it is concluded that the broadening at 530.5 eV is due to loading by dexamethasone (loading 10%) within the nanogel. The loading was determined by isotope-dilution liquid chromatography tandem-mass spectrometry (LC-MS/MS).[135] By using LC-MS/MS, usually, the error limit is less than 0.1%.

The observed differences of the O $1s \rightarrow \pi^*$ transition between dexamethasone and the pNIPAM nanogel is again reasoned by the chemical surrounding of the pNIPAM and dexamethasone carbonyl groups. In contrast to dexamethasone, the carbonyl site of pNIPAM nanogel is neighbored by a nitrogen atom making it an amide group, see Figure 3.5.2. This chemical difference is resulting in the observed difference of the O 1s absorption spectra, highlighting the chemical sensitivity of X-ray spectromicroscopy.

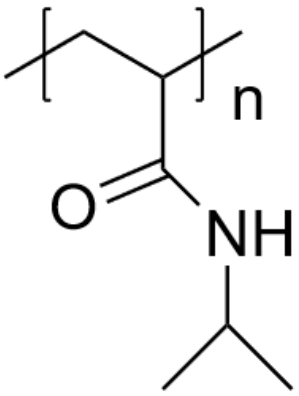

Fig. 3.5.2: Structure of pNIPAM nanogel.

The purpose of these experiments was to determine the effect of triggered thermoresponsive nanogels on drug penetration, after topical application, on human skin. The focus of the studies was set on qualitative probing the impact of nanogels on dermal dexamethasone penetration. In Figure 3.5.3 transmission and optical density images of human skin treated with a dexamethasone loaded thermoresponsive nanogel, both triggered and untriggered, are shown.

To determine the dexamethasone penetration, samples were excited at 528.0 eV and 530.5 eV photon energy, respectively. The drug penetration time was 100 min. In addition, the optical density at 528.0 eV and 538.0 eV excitation energy was investigated to make possible effects of the nanogel on the human skin visible. Both, human skin, and the dexamethasone

loaded thermoresponsive nanogel show an increased absorption at 538.0 eV. Thus, observed changes in optical density are discussed in terms of possible assignments of the spectroscopic results.

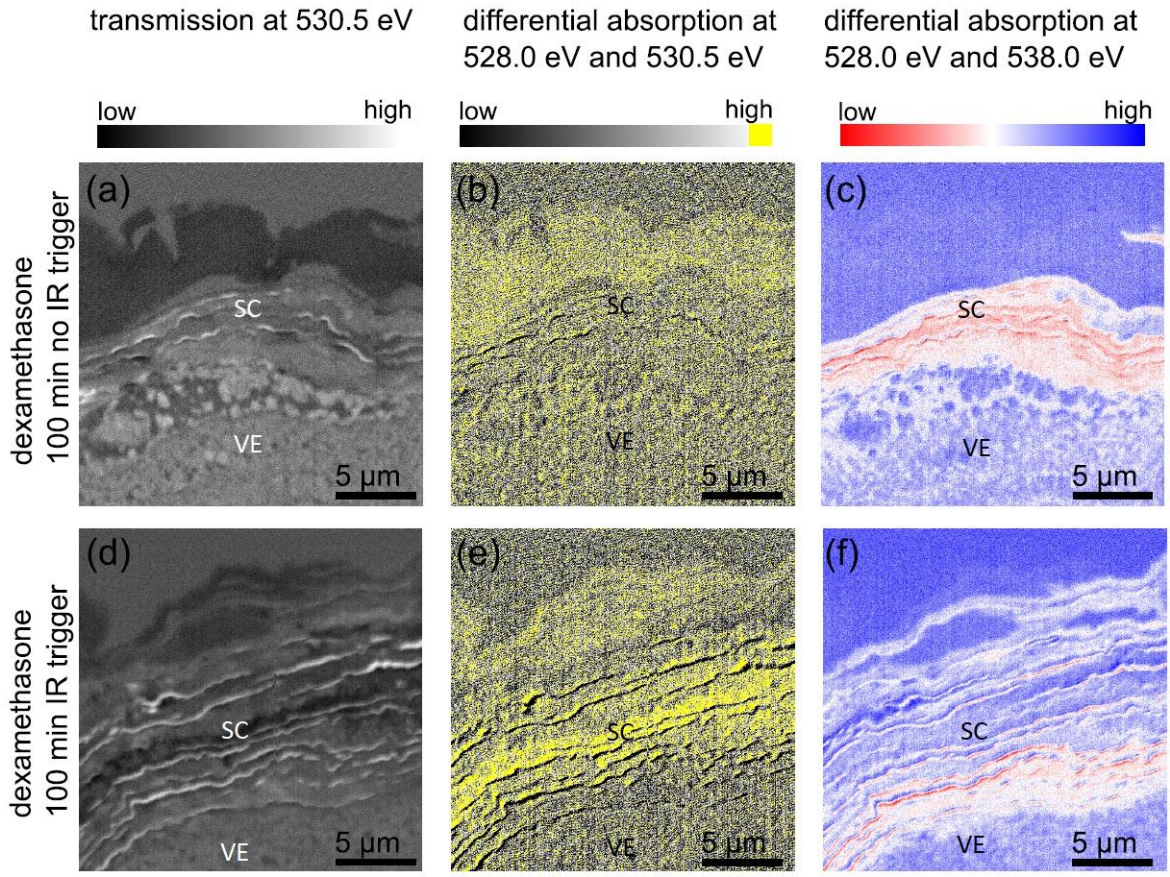

Fig. 3.5.3: Human skin treated with dexamethasone loaded thermoresponsive nanogel, for 100 min penetration time. Image (a), (b), and (c) refer to the untriggered sample, whereas (d), (e), and (f) show images of IR triggered sample. (a) and (d) are showing transmission images at 530.5 eV, (b) and (e) are showing the optical density at 528.0 eV and 530.5 eV, respectively, for probing dexamethasone. The optical density images (c) and (f) were gathered by exciting the sample at 528.0 eV and 538.0 eV probing the nanogel. The stratum corneum (SC) and the viable epidermis (VE) are indicated.

In Figure 3.5.3 (a) and (d) transmission images of both samples, triggered and untriggered, are shown. The corresponding optical density images are shown in Figure 3.5.3 (b) and (e). The optical density was calculated from the images recorded at 528.0 eV and 530.5 eV photon energy, respectively. For both samples, residuals of dexamethasone are found on top of the stratum corneum (yellow). Differences for the drug penetration between untriggered and triggered thermoresponsive nanogels are found in the stratum corneum. A significantly

stronger optical density is observed for the triggered nanogel (yellow regions). Here, more drug penetrated deeply into the stratum corneum. However, the optical density drops towards the viable epidermis after reaching its maximum approximately at the mid of the stratum corneum. Furthermore, looking at the optical density images taken at 528.0 eV and 538.0 eV photon energy, in Figure 3.5.3 (c) and (f), the following observation is made: The same low intensity in optical density (red regions) is observed between (f) the lower part of the stratum corneum, for skin treated with triggered nanogel, and (c) the whole stratum corneum for skin treated with untriggered nanogel. The thermoresponsive nanogel seems to alter the structure of the stratum corneum, by causing a swelling of the corneocytes, and enhance drug penetration over time, especially when thermally triggered. Both effects go hand in hand. 100 min drug penetration time is enough for affecting almost the entire stratum corneum. However, the lowest part of the stratum corneum, the border to the viable epidermis, was not affected and drug penetration was only observed above this region.

Thermoresponsive nanogel having an effect on the stratum corneum structure was reported recently by using TEM, fluorescence microscopy, and Stimulated Raman microscopy.[134] It was found that thermoresponsive nanogels modify the hydration of the stratum corneum leading to a swelling of the corneocytes and a subsequent formation of larger gaps between lipid layers. It is assumed that the visible swelling of the corneocytes is accompanied by a perturbation of the lipid and protein supramolecular organization.[134] Thus, an enhanced skin penetration can occur by creating penetration channels through the hydrated corneocytes.[134] Those effects were already reported by Warner et al. after incubation of the SC with water for 24 h.[136] The observed changes can be reasoned by an induced hydration effect caused by thermally triggered nanogel, leading to a swelling of the corneocytes

While the labeled drug penetration as well as the structural changes within the stratum corneum were reported, the exact penetration route was only hypothesized.[134] The hypothesis was strengthened by TEM and Stimulated Raman Microscopy, however, a direct observation of the drug within the skin sub-structure was not possible due to the lack in spatial resolution in Raman Microscopy and the missing ability to probe selectively the drug, respectively, as well as the replacement drug, fluorescein, by TEM. By using X-ray microscopy, the drug dexamethasone was localized within the SC, compare Figure 3.5.3 (d) and (e). The white structures within the stratum corneum, Figure 3.5.3 (a, d), are due to the lipid layers between the corneocytes, whereas the darker structures are due to corneocytes. Now, comparing Figure 3.5.3 (d) to Figure 3.5.3 (e) one observes that high optical density due to dexamethasone is observed within the corneocytes but not within the lipid layers. This

appears to be significantly different compared to the other dexamethasone formulations, since dexamethasone, as a lipophilic drug, which favors the penetration through the lipid matrix and penetration of the corneocytes was not observed.[13] The hypothesis that thermoresponsive nanogels increase drug penetration by hydration of the stratum corneum, leading to an perturbated lipid and protein supramolecular organization, made by Giulbudagian et al. seems to be correct.[134] The drug penetration is enhanced by the hydration of corneocytes creating drug penetration channels. Also, for high molecular-weight-drugs, above 500 Da, the condition of the stratum corneum is of importance for drug penetration. To transport the drug towards the site of action, also other procedures than using a nanocarrier formulation, such as a pretreatment of the skin can be conducted. Recently, it was shown that a pretreatment with serine protease trypsin can enhance drug penetration of rapamycin by affecting the skin barrier via enzymatic disruption of the stratum corneum.[137]

Triggering of the thermoresponsive nanogel has a significant role in distributing the drug. Without initial thermal triggering no swelling of the corneocytes is observed. The thermoresponsive nanogel will not release its water content leading to the previously described alteration of the stratum corneum. Thus, no enhanced drug penetration can occur. In fact, without triggering also the drug will not be released from the nanogel and therefore cannot penetrate the skin. Thermoresponsive nanogels, or triggerable nanogels have in common that they have the advantage that the drug release can be controlled and confined to a certain area of interest. Thus, unnecessary drug exposure to non-target regions can be avoided by minimizing adverse effects of the drug.

Thermoresponsive nanogels offer an alternative way to deliver drugs when topically applied. Especially for hydrophilic drugs, which have problems in overcoming the stratum corneum barrier, thermoresponsive nanogels seem to be an excellent choice for enhanced drug penetration.

3.6 Combining Stimulated Raman Microscopy and Life Science Microscopy in a New Setup: Measurements on Human Skin and a technical review.

Stimulated Raman microscopy is used in life sciences as a label-free approach to analyze biological samples.[123,138–140] Recently, advances in Stimulated Raman microscopy were reported, including video rate imaging, and femtosecond time-resolved impulsive Stimulated Raman spectroscopy.[125,141] This Chapter reports on the use of a unique Stimulated Raman microscope, combining Stimulated Raman microscopy with bright field microscopy, phase contrast, fluorescence microscopy and hyper-spectral imaging at different wavelength in one setup. By combining different spectromicroscopy methods a deeper understanding of species under investigation can achieved. As part of this thesis the setup was used to deepen the knowledge of drug and nanocarrier penetration in skin by investigating the structural changes. A schematic overview and the technical specifications of the microscope are reported in Chapter 2.4.

Combining Stimulated Raman microscopy and life science microscopy has several advantages. Information gathered from various types of microscopy methods can be combined to reveal new information on the sample under investigation. Furthermore, real time process-control of the Stimulated Raman scanned samples can be obtained. Thus, sample damage, due to intense laser irradiation, can be observed in real time and therefore, one can adapt the measurements to the unique characteristics of the sample e.g., by reducing the laser power or dwell time. This is of great advantage when analyzing biological samples. Also drifts of the laser focus, mechanically or thermally caused, can be compensated fastly. Especially, for measurements where a single image takes up to or above one hour, this feature is useful. In Figure 3.6.1 real time process-control during Stimulated Raman measurements is demonstrated. Real time in this content means that the optical image, the reflected laser radiation, and the transmitted laser radiation can be compared at each acquisition time during the measurement. Measurements were conducted on human skin, cryo-sliced (-20 °C) into roughly 6 µm cross sections after embedding in Tissue-Tek®. The embedding medium consists of water-soluble glycols and resin (Tissue-Tec®).[142]

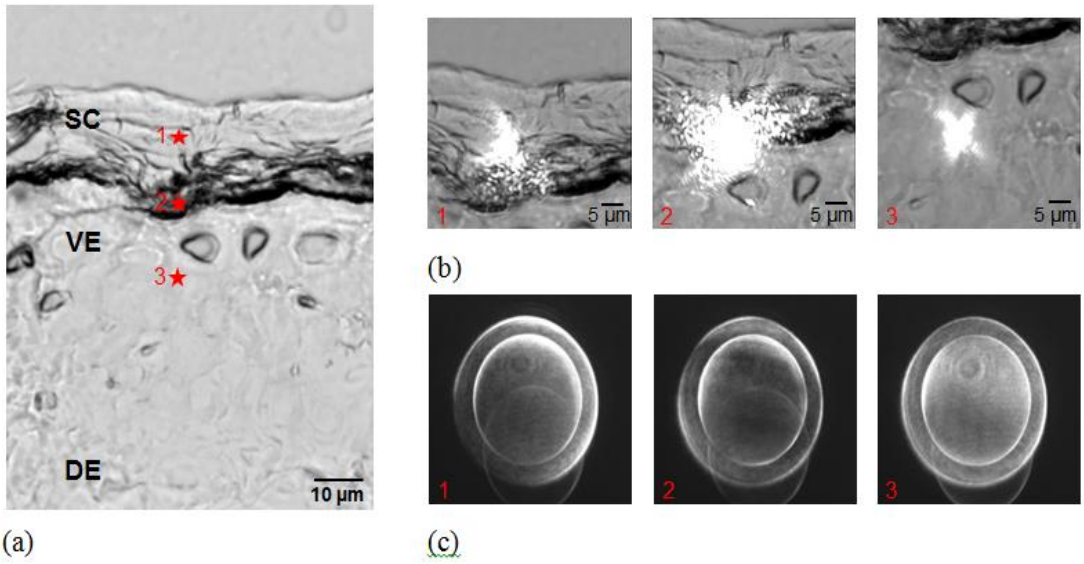

Fig. 3.6.1: Real time images of the sample-laser interaction during Stimulated Raman measurements. (a) cross section of human skin including the stratum corneum (SC), the viable epidermis (VE) and the dermis (DE). (b) the reflected and (c) the transmitted laser radiation is shown for different positions within the human skin sample. The different positions for process-control are indicated by the red numbers 1, 2, and 3.

An optical microscopy image of a human skin cross section is shown in Figure 3.6.1 (a), the skin layers are indicated. The skin was treated with the fluorescent dye, fluorescein (2 µg/cm²), which is relevant for subsequent measurements. The optical microscopy images are used to observe sample damage during measurement. Positions for real-time process control are indicated by red stars and numbers. The positions were chosen so that two different structures, with different reflection characteristics, within the stratum corneum as well as one position within the viable epidermis can be evaluated. The reflected laser light during imaging is shown in Figure 3.6.1 (b). The spatial dimension of the reflection pattern exceeds by far the spot size of the laser beam, which is around 0.7 µm. This is caused by the properties of the biological sample. Here, sample thickness and the inhomogeneous structure of the skin can be found as the reason. The light is reflected and scattered multiple times within the sample resulting in the observed reflection pattern. The reflected laser light therefore includes information on the morphology, especially of the thickness of the sample. Different reflection patterns for different process-control positions are observed. Within the stratum corneum the reflected laser spot is showing an increased size, see Figure 3.6.1 (b) images 1 and 2. This is due to the increased thickness of the stratum corneum compared to the viable epidermis. In Figure 3.6.2 it will be shown that the stratum corneum is 2 to 3-fold thicker

than the viable epidermis. Different structures within the skin will also have an impact on the reflected laser light. One can distinguish thick but loose from thick and dense skin material. The transmitted laser light is shown in Figure 3.6.1 (c). The observed multiple circular structures are caused by back and front side reflection at dielectric mirrors used for laser beam guidance. The image corresponds to a projection of the transmitted laser light through the entire skin sample. Therefore, the image scale varies with the local skin thickness and can only be estimated. The lateral resolution is described by the Rayleigh criterion as:

$$d_{Ray} = \frac{0.61 \cdot \lambda}{NA} \tag{E3.6.1}$$

where the lateral resolution and therefore, the diameter of the laser spot is given by d_{Ray}, λ is the wavelength of the incident light, and NA is the numerical aperture. Parameters used in common for this study are $\lambda = 811.2\ nm$ and $NA = 0.65$ (LCPLN50XIR, Olympus). As a result, the spot diameter is estimated to 761 nm. Spot diameters displaced from the focal point, for example at the skin surface, can then be calculated by using the two equations for the Rayleigh length:

$$z_R = \frac{\omega_0^2 \pi}{\lambda} \tag{E3.6.2}$$

$$\omega(z)^2 = \omega_0^2 \left[1 + \left(\frac{z}{z_R}\right)^2\right] \tag{E3.6.3}$$

Here, ω_0 is the beam waist, the radial size of the beam at its narrowest position, while $\omega(z)$ is the radial size of the beam at distance z from the beam waist. The Rayleigh length z_R describes the distance along the propagation of a Gaussian beam from the waist at which the area of the cross section is doubled. The wavelength of the beam is given by λ. Values for z are set to the half of the skin thickness, when the focal point is set to be in the middle of the skin sample, since the divergence of the laser beam from the focal point is symmetric. Assuming a thickness of 6 µm (cryo-sliced-sections) and making use of $d_{Ray}/2$ estimated from equation E3.6.1, a diameter of the laser spot at the skin surface of $(4 \pm 1)\mu m$ is estimated. Of course, with varying skin thickness this diameter also varies. For example, at the stratum corneum the observed spot diameter is roughly $(8 \pm 2)\mu m$. By this, the thickness of the dark horizontally aligned structures in Figure 3.6.1 (c) image 2 can be estimated. The width of these structures is between $0.8\ \mu m$ and $1.6\ \mu m$. This width corresponds to the average spatial extent, in vertical direction, of corneocytes.

By combining Stimulated Raman microscopy, bright field microscopy, phase contrast, fluorescence microscopy and hyper-spectral imaging at different wavelength, Stimulated

Raman measurements on human skin were conducted. Samples were measured in the Stimulated Raman loss mode, described in Chapter 2.4. The local distributions of proteins ($\nu_S CH_3$) at $2934\ cm^{-1}$, lipids ($\nu_S CH_2$) at $2850\ cm^{-1}$, and water at $3420\ cm^{-1}$ within human skin sample, introduced in Figure 3.6.1, are shown in Figure 3.6.2. The focus of the laser was set to 4 µm above the specimen holder's glass side.

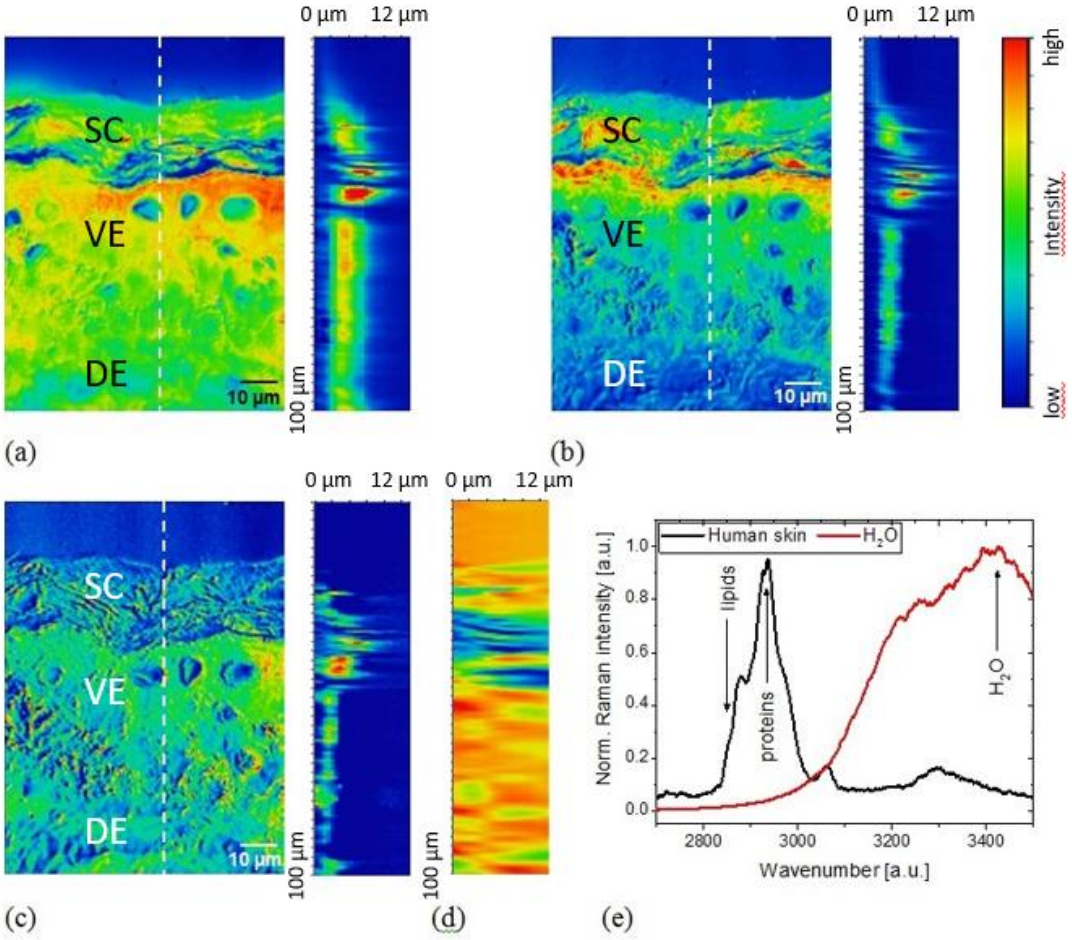

Fig. 3.6.2: The distribution of (a) proteins, (b) lipids, and (c) water in human skin investigated by Stimulated Raman microscopy. Depth profiles along the white dashed line are shown together with the protein, lipid, and water distribution. The (d) depth profile of optical transmission at 811.2 nm and (e) normalized Raman spectra are included. The stratum corneum (SC), the viable epidermis (VE), and the dermis (DE) are indicated.

The dashed white lines indicate the origin of the thickness profiles shown in Figure 3.6.2 (a), (b), and (c). The thickness profile describes the relative amount of the species of interest in dependence of the skin depths. A depth profile at 811.2 nm of the optical transmission is shown in Figure 3.6.2 (d) which can be compared to the thickness profiles of the species of

interest. The normalized Raman spectra of the species of interest are shown in Figure 3.6.2 (e). It should be noted that all images were taken using the same objective. Therefore, the time delay, between different measurements is within the range of 100 ms to seconds. This points out a clear advantage of the system; measurements using different techniques can be conducted in a time saving way. Thus, more samples or a larger region of interest can be analyzed. Also, it reduces the time the sample is exposed to the environmental conditions within the laboratory between the measurements, which is important especially for fresh biological samples. As part of the technical review, those measurements were used to verify the use of Stimulated Raman microscopy for analyzing human skin. Measurements confirmed the known histological properties of skin. Proteins are homogeneously distributed within the skin layers, see Figure 3.6.2 (a). Except for small region between the stratum corneum and the viable epidermis, where an increased amount (red) of proteins is found, the protein amount is similar (green to yellow). However, it slightly decreases toward the dermis. This is different for lipids. In Figure 3.6.2 (b) an increased amount of lipids (red) is found within the stratum corneum. The amount of lipids rapidly decreases towards the dermis. The decreasing local lipid concentration, even within the stratum corneum, and the uniform protein distribution was reported in former articles.[138,142–145] The weak signal of proteins and lipids outside of the skin, on top of the glass surface, has its origin in the used media for embedding the skin. In contrast to lipids, water can be found in the deeper layers of the skin rather than inside the stratum corneum. This distribution explains quite well the function of the skin as the protective layer, especially in terms of avoiding water loss of the human body. The high lipid concentration within the stratum corneum prevents the body from unwanted water loss.[28,146] Results shown in Figure 3.6.2 are consistent with literature from former studies using other techniques like CARS and IR microscopy.[147,148]

By comparing the depth profiles of Stimulated Raman microscopy to the depth profile of the transmission image at 811.2 nm another difference between both imaging methods is observed. For Stimulated Raman microscopy the surface of the skin cross section can be determined by a sharp intensity drop to zero. However, the transmission profile is showing varying signal intensities up to thickness of 12 µm, see Figure 3.6.2 (depth profiles).

The depth resolution for optical and Stimulated Raman microscopy is approximated according to the Rayleigh criterion:

$$FWHM_{axial} = \frac{0.88 \cdot \lambda}{n - \sqrt{n^2 - NA^2}} \qquad \text{(E3.6.4)}$$

Here, full width half maximum ($FWHM_{axial}$) is the axial resolution, n is the refractive index, λ the wavelength of the incident laser beam and NA the numerical aperture. Using the specifications of this setup an axial resolution is approximated to (3 ± 0.2) µm. Having the same axial resolution, the difference of the depth profiles for both imaging methods (transmission and Stimulated Raman scattering) arises from the interaction of the detected radiation. In transmission imaging, information on all skin structures outside the focal plane within the light cone is gathered. Therefore, even when the focus is far away from the sample surface, information from the sample is still gathered in transmission mode. This is not true for Stimulated Raman microscopy. Stimulated Raman scattering occurs only within the common focal plane of the pump- and Stokes-beam. Therefore, Stimulated Raman microscopy profiles are more suited to describe the shape of a sample at the focal plane.

Another effect observed within the sample is an alternating transmission intensity within the depth profile of the optical transmission, shown in Figure 3.6.2 (d). This effect is caused by the refractive-index mismatch between the biological sample and the air surrounding the sample under study.[149,150] It can be considered as a depth induced spherical aberration. This is not observed within the depth profile of Stimulated Raman microscopy measurements and is a good example how misinterpretation of results is avoided when Stimulated Raman microscopy is combined with life science microscopy.

While Stimulated Raman microscopy proves to be an excellent technique for combination with optical transmission microscopy, especially for biological samples, also other life science-based microscopy techniques can take advantage of being combined with Stimulated Raman microscopy. Stimulated Raman microscopy imaging of human skin together with bright field microscopy, variations in thickness and refraction index by phase contrast, and localization of the applied fluorescence dye as label-based microscopy are shown in Figure 3.6.3. All images were obtained from the same region within the skin sample introduced in Figure 3.6.1. Hyper-spectral images from near UV to NIR were included. The spectral region of the hyper-spectral imaging was chosen as (e) 350 nm – 495 nm, (f) 495 nm – 610 nm, (g) 610 nm – 715 nm and (h) 715 nm – 1000 nm.

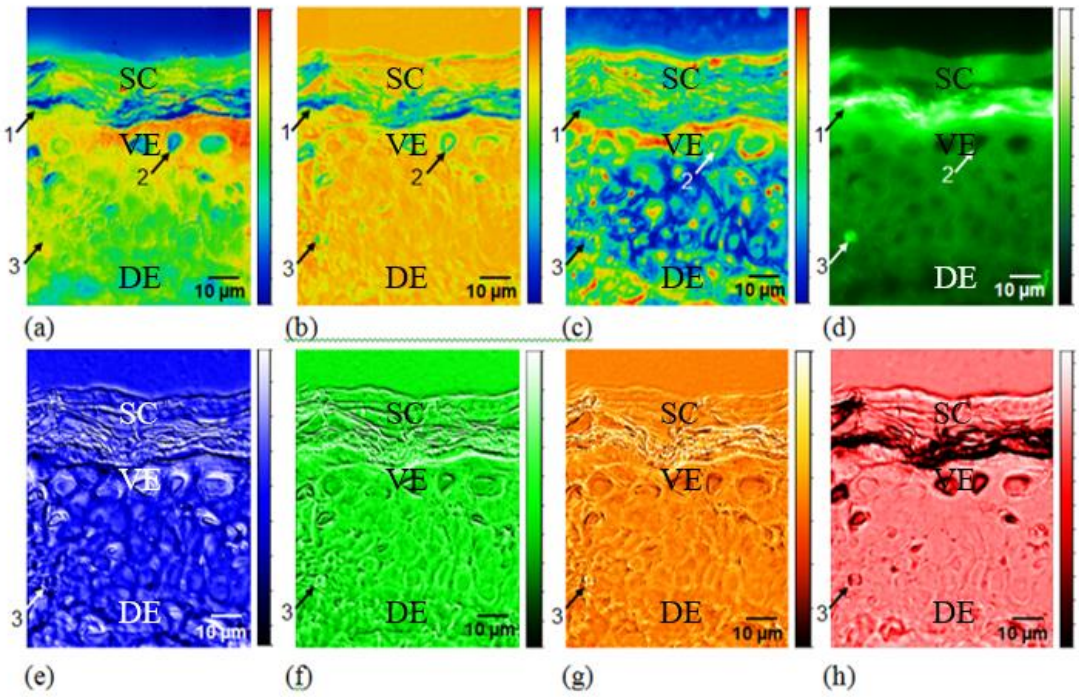

Fig. 3.6.3: (a) Protein distribution measured by Stimulated Raman microscopy, (b) bright field microscopy, (c) phase contrast, (d) fluorescence microscopy, and hyper-spectral imaging at the wavelength of (e) 350 nm – 495 nm, (f) 495 nm – 610 nm, (g) 610 nm – 715 nm, and (h) 715 nm – 1000 nm of human skin. Regions discussed in the following text are marked by black arrows and numbers. The colored intensity bar next to each image has the lowest intensity at its bottom and the highest intensity at the top. The stratum corneum (SC), the viable epidermis (VE), and the dermis (DE) are indicated.

Three positions within the skin section were selected to demonstrate the benefit of combining Stimulated Raman microscopy with life science microscopy techniques, see Figure 3.6.3. Thereby, the first position (1) corresponds to the bands of low transmission and high concentration of fluorescein within the stratum corneum, not visible in optical transmission and Stimulated Raman microscopy, but visible when using phase contrast. This region consists of fine laminar sub-structures. In this region low intensities for lipids, proteins, and water are observed by Stimulated Raman microscopy. These findings correspond to holes and therefore to a loosen structure of the stratum corneum, see Figure 3.6.2. This contrasts with fluorescence microscopy which shows a highly dense, fluorescent dye loaded, and structured stratum corneum, see Figure 3.6.3 (d). While the entire stratum corneum is indeed highly structured, dense, and filled with fluorescent dye, the stratum corneum is also locally loosely attached to the viable epidermis and contains free spaces like holes. This is most

likely a side effect of cryo-slicing. However, it clearly highlights the advantage of combining life science microscopy with Stimulated Raman Microscopy.

Position (2) corresponds to three holes within the skin caused by ripped-out keratinocyte nuclei during cutting of the sample. The skin within this region is thin. Transmission and fluorescence imaging indicate that this region contains no skin, since the intensities are similar to those outside the skin. However, in Stimulated Raman microscopy medium intensities within the region of the holes are observed. Transmission microscopy is insensitive to thin layers according to the Beer-Lambert law, especially for transparent samples. Fluorescence microscopy is label based, therefore without fluorescent dyes inside the thin skin section no signal is found. Due to the high chemical sensitivity of Stimulated Raman microscopy thin layers of the skin can be detected and identified.

Position (3) indicates high intensities found by fluorescence microscopy. Within those regions no specific intensity change can be observed by Stimulated Raman microscopy. Therefore, an increased content of proteins, lipids and water can be excluded. However, within the images of the other microscopy techniques a circular structure can be observed. A wavelength dependent diffraction patterns can be observed by comparing the different hyper-spectral images. This could indicate an accumulation point of fluorescent dye. While no cellular dependency of this structure is found by Stimulated Raman microscopy, hyper-spectral imaging may be more sensitive to such structures. Thereby, the contrast is a result of different absorption properties of this skin component for different incident wavelengths.

By combining the high chemical and local selectivity of Stimulated Raman microscopy with life science microscopy techniques, in an all-in-one solution, advantages to deepen the knowledge on skin's structural information, when comparing to a single method, is reported. Due to complement information gathered from different microscopy techniques a more complex understanding of the sample properties is obtained. Also, a real time process-control has been included to avoid laser-induced sample damage and thermally and mechanically induced drifts in focus. This is important, especially for biological samples. The all-in-one setup also reduces the data acquisition time by the possibility to simply switch between different experimental techniques during a measurement. Further work, using this setup, highlights the possibility to observe and investigate structural changes in skin when treated with drugs and nanocarrier.[134,151]

4. Summary

Label free spectromicroscopy on drug and nanocarrier penetration into human and murine skin was conducted by scanning X-ray microscopy. Thereby, the anti-inflammatory drugs dexamethasone and tacrolimus were investigated. With focus on different drug formulations the penetration characteristics in skin, after topical application, was investigated for core multishell nanocarriers, thermoresponsive nanogels, and micellar nanocarriers. Stimulated Raman microscopy was conducted on fluorescent dye treated human skin to investigate the benefit when combining stimulated Raman microscopy with other life science imaging techniques.

Scanning X-ray microscopy measurements on human skin revealed that label-free detection of dexamethasone in human skin can be accomplished by oxygen 1s spectromicroscopy.[13] The chemical contrast was gained by selective probing of the oxygen $1s \rightarrow \pi^*$ transition of the π bonded oxygen. An advantage of scanning X-ray microscopy, besides of being label free, is found in the high spatial resolution and sensitivity. Measurements using a pixel size of down to 50 nm were conducted, e.g. for localization of core multishell nanocarriers within the stratum corneum of skin.

It was found that dexamethasone penetrates the stratum corneum via the lipid layers between the corneocytes. Thereby, the penetration of dexamethasone depends on the condition of the stratum corneum.[36] For healthy skin it was found that dexamethasone penetration into the viable skin, after topical application, occurs for a penetration time of more than 10 min. However, if the stratum corneum was tape-stripped prior to the topical drug application, dexamethasone penetration into the viable epidermis occurs in less than 10 min of drug penetration time. In numbers, after 10 min dexamethasone penetration time for skin with a tape stripped stratum corneum an amount of $110 \pm 50\ \mu g$, of the totally applied 600 µg dexamethasone, was found within the viable epidermis. Furthermore, topical exposure of the skin samples for 100 min and 1000 min dexamethasone penetration time for healthy and tape-stripped human skin were conducted and compared to each other. Consistent with measurements for 10 min drug penetration time it was found that dexamethasone penetration occurs faster into the viable epidermis for tape-stripped skin, also for 100 min drug penetration time. However, for 1000 min drug penetration time the dexamethasone concentration within the viable epidermis reached similar values. Thus, a saturation or equilibrium drug flow within or through the viable epidermis is assumed to be observed.

Based on the experimental data, a model for the dexamethasone penetration into human skin was developed by collaboration partners within the SFB 1112.[152] This model can lead to further understanding of drug penetration mechanism and could be also adapted to other drugs.

For core multishell nanocarriers, nanogels and micellar nanocarriers it is reported that nanocarrier penetration only occurs within the stratum corneum but not into the viable skin after topical application. It was found that core multishell nanocarriers penetrate into the lipid layer of the stratum corneum and enhance the penetration of dexamethasone into the viable epidermis.[89] Compared to a HEC gel dexamethasone formulation, when using core multishell nanocarriers, the local drug concentration within the epidermis, after 16 h penetration time, is increased by up to 50% for core multishell nanocarriers. In contrast to the core multishell nanocarrier penetration, thermoresponsive nanogels create drug penetration channels by hydration of the corneocytes of the stratum corneum.[97] A subsequent penetration of dexamethasone into the corneocytes is observed. The effect is significantly enhanced when the thermoresponsive nanogel was triggered by IR-radiation. Tacrolimus loaded micellar nanocarriers are reported to penetrate via the lipid layer, similar to core multishell nanocarriers and dexamethasone, into the stratum corneum. The investigated micellar nanocarriers are known to enhance the penetration of tacrolimus into the viable epidermis, as compared to standard drug formulation Protopic, where the drug is formulated in petroleum jelly.[93] Except for measurements on micellar nanocarriers, all reported measurements were conducted using the oxygen 1s regime. For measurements on micellar nanocarriers the carbon 1s excitation was utilized. This is a consequence of the chemical selectivity of the species of interest. The excitation energies were carefully selected by determining differences within the absorption spectra of the species of interest and the surrounding tissue.

Apart from scanning X-ray microscopy it was successfully shown that combining Stimulated Raman microscopy with life science microscopy techniques can be used to enhance the understanding of the properties of skin resulting from topical application of drug and nanocarrier penetration.[97] For this purpose, contribution to an unique Stimulated Raman microscope and the Raman mapping software SRSLab, were made. The setup is capable of conducting the following modes of investigation: Stimulated Raman microscopy, bright field microscopy, phase contrast microscopy, fluorescence microscopy, and hyper-spectral imaging from UV to NIR light (350 nm – 495 nm, 495 nm – 610 nm, 610 nm – 715 nm, and 715 nm – 1000 nm).

Conducting Stimulated Raman microscopy, the protein, the lipid, and the water distribution in skin was analyzed by use of the corresponding Raman shifts. Results from Stimulated Raman microscopy were compared and combined with other life science techniques to deepen the insight into skin treated with fluorescent dye. In a first step the fluorescent dye fluorescein was used instead of a drug or nanocarrier. Specific features, such as the fluorescein localization within the stratum corneum, holes within the skin due to ripped-out keratinocytes, and unexpected accumulation points of fluorescein, deep within the viable epidermis, were discussed. Future work could link the drug and nanocarrier penetration to structural changes, e.g. the protein and lipid distribution, within the skin.[134,151]

X-ray microscopy and Stimulated Raman microscopy, as label free approaches with high chemical sensitivity, were successfully used to investigate the drug and nanocarrier penetration in skin. By using advanced drug formulations enhanced drug delivery characteristics were unraveled. The results may contribute to an improved future use of topical treatment for curing inflammatory skin diseases.

Subsequent work could include investigation on nanoscopic drug delivery systems with triggered drug release, optimized for the specific use for treating inflammatory skin diseases. For example, drug release can be triggered by the changed pH value of inflamed skin.[153]

5. References

1. Palmer, C. N. A. *et al.* Common loss-of-function variants of the epidermal barrier protein filaggrin are a major predisposing factor for atopic dermatitis. *Nat. Genet.* **38**, 441–446 (2006).
2. Cookson, W. O. C. M. & Moffatt, M. F. The genetics of atopic dermatitis. *Curr. Opin. Allergy Clin. Immunol.* **2**, 383–387 (2002).
3. Evers, A. W. M. *et al.* Common burden of chronic skin diseases? Contributors to psychological distress in adults with psoriasis and atopic dermatitis. *Br. J. Dermatol.* **152**, 1275–1281 (2005).
4. Wittkowski, A., Richards, H. L., Griffiths, C. E. M. & Main, C. J. The impact of psychological and clinical factors on quality of life in individuals with atopic dermatitis. *J. Psychosom. Res.* **57**, 195–200 (2004).
5. Akdis, C. A. *et al.* Diagnosis and treatment of atopic dermatitis in children and adults: European Academy of Allergology and Clinical Immunology/American Academy of Allergy, Asthma and Immunology/PRACTALL Consensus Report. *Allergy* **61**, 969–987 (2006).
6. Carroll, C. L., Clarke, J., Camacho, F., Balkrishnan, R. & Feldman, S. R. Topical Tacrolimus Ointment Combined With 6% Salicylic Acid Gel for Plaque Psoriasis Treatment. *Arch. Dermatol.* **141**, (2005).
7. Küchler, S. *et al.* Influence of nanocarrier type and size on skin delivery of hydrophilic agents. *Int. J. Pharm.* **377**, 169–172 (2009).
8. Lademann, J. *et al.* Drug Delivery with Topically Applied Nanoparticles: Science Fiction or Reality? *Skin Pharmacol. Physiol.* **26**, 227–233 (2013).
9. Gupta, M., Agrawal, U. & Vyas, S. P. Nanocarrier-based topical drug delivery for the treatment of skin diseases. *Expert Opin. Drug Deliv.* **9**, 783–804 (2012).

10. Vega-Villa, K. R. *et al.* Clinical toxicities of nanocarrier systems. *Adv. Drug Deliv. Rev.* **60**, 929–938 (2008).

11. Rancan, F. *et al.* Drug delivery across intact and disrupted skin barrier: Identification of cell populations interacting with penetrated thermoresponsive nanogels. *Eur. J. Pharm. Biopharm.* **116**, 4–11 (2017).

12. Küchler, S. *et al.* Nanoparticles for skin penetration enhancement – A comparison of a dendritic core-multishell-nanotransporter and solid lipid nanoparticles. *Eur. J. Pharm. Biopharm.* **71**, 243–250 (2009).

13. Yamamoto, K. *et al.* Selective Probing of the Penetration of Dexamethasone into Human Skin by Soft X-ray Spectromicroscopy. *Anal. Chem.* **87**, 6173–6179 (2015).

14. Saar, B. G., Contreras-Rojas, L. R., Xie, X. S. & Guy, R. H. Imaging Drug Delivery to Skin with Stimulated Raman Scattering Microscopy. *Mol. Pharm.* **8**, 969–975 (2011).

15. Jacobsen, C. *et al.* Diffraction-limited imaging in a scanning transmission x-ray microscope. *Opt. Commun.* **86**, 351–364 (1991).

16. Vila-Comamala, J. *et al.* Advanced thin film technology for ultrahigh resolution X-ray microscopy. *Ultramicroscopy* **109**, 1360–1364 (2009).

17. Chao, W. *et al.* Real space soft x-ray imaging at 10 nm spatial resolution. *Opt. Express* **20**, 9777 (2012).

18. Proksch, E., Brandner, J. M. & Jensen, J.-M. The skin: an indispensable barrier. *Exp. Dermatol.* **17**, 1063–1072 (2008).

19. Rawlings, A. V. & Harding, C. R. Moisturization and skin barrier function. *Dermatol. Ther.* **17**, 43–48 (2004).

20. Trémezaygues, L. & Reichrath, J. Zur Bedeutung des Vitamin-D-Stoffwechsels in der humanen Haut: Eine aktuelle Standortbestimmung. *Hautarzt* **61**, 478–486 (2010).

21. Hengge, U. R., Ruzicka, T., Schwartz, R. A. & Cork, M. J. Adverse effects of topical glucocorticosteroids. *J. Am. Acad. Dermatol.* **54**, 1–15 (2006).

22. Schaefer, H., Zesch, A. & Stüttgen, G. *Skin Permeability*. (Springer Berlin Heidelberg, 1982).

23. Rajesh, A., Wise, L. & Hibma, M. The role of Langerhans cells in pathologies of the skin. *Immunol. Cell Biol.* **97**, 700–713 (2019).

24. Fuchs, E. Epidermal differentiation: the bare essentials. *J. Cell Biol.* **111**, 2807–2814 (1990).

25. Iizuka, H. Epidermal turnover time. *J. Dermatol. Sci.* **8**, 215–217 (1994).

26. Elias, P. M. Epidermal barrier function: intercellular lamellar lipid structures, origin, composition and metabolism. *J. Controlled Release* **15**, 199–208 (1991).

27. Elias, P. M. Structure and function of the stratum corneum permeability barrier. *Drug Dev. Res.* **13**, 97–105 (1988).

28. Werner, Y. & Lindberg, M. Transepidermal water loss in dry and clinically normal skin in patients with atopic dermatitis. *Acta Derm. Venereol.* **65**, 102–105 (1985).

29. Pinnagoda, J., Tupkek, R. A., Agner, T. & Serup, J. Guidelines for transepidermal water loss (TEWL) measurement: A Report from the Standardization Group of the European Society of Contact Dermatitis. *Contact Dermatitis* **22**, 164–178 (1990).

30. Christophers, E. & Laurence, E. B. Kinetics and Structural Organisation of the Epidermis. in *Current Problems in Dermatology* (ed. Mali, J. W. H.) vol. 6 87–106 (S. Karger AG, 1976).

31. Warner, R. R., Myers, M. C. & Taylor, D. A. Electron Probe Analysis of Human Skin: Determination of the Water Concentration Profile. *J. Invest. Dermatol.* **90**, 218–224 (1988).

32. Bos, J. D. & Meinardi, M. M. The 500 Dalton rule for the skin penetration of chemical compounds and drugs. *Exp. Dermatol.* **9**, 165–169 (2000).

33. Lademann, J. *et al.* Hair Follicles - An Efficient Storage and Penetration Pathway for Topically Applied Substances. *Skin Pharmacol. Physiol.* **21**, 150–155 (2008).

34. Brandner, J. M. Tight junctions and tight junction proteins in mammalian epidermis. *Eur. J. Pharm. Biopharm.* **72**, 289–294 (2009).

35. Leyvraz, C. *et al.* The epidermal barrier function is dependent on the serine protease CAP1/ *Prss8*. *J. Cell Biol.* **170**, 487–496 (2005).

36. Yamamoto, K. *et al.* Influence of the skin barrier on the penetration of topically-applied dexamethasone probed by soft X-ray spectromicroscopy. *Eur. J. Pharm. Biopharm.* **118**, 30–37 (2017).

37. Arends, F. & Lieleg, O. Biophysical Properties of the Basal Lamina: A Highly Selective Extracellular Matrix. in *Composition and Function of the Extracellular Matrix in the Human Body* (ed. Travascio, F.) (InTech, 2016). doi:10.5772/62519.

38. Wang, X.-N. *et al.* A Three-Dimensional Atlas of Human Dermal Leukocytes, Lymphatics, and Blood Vessels. *J. Invest. Dermatol.* **134**, 965–974 (2014).

39. Mirrashed, F., Sharp, J. C., Krause, V., Morgan, J. & Tomanek, B. Pilot study of dermal and subcutaneous fat structures by MRI in individuals who differ in gender, BMI, and cellulite grading. *Skin Res. Technol.* **10**, 161–168 (2004).

40. *Vorträge der XII. Fortbildungswoche der Dermatologischen Klinik und Poliklinik der Ludwig-Maximilians-Universität München in Verbindung mit dem Berufsverband der Deutschen Dermatologen e.V. vom 23.- 28. Juli 1989*. (Springer, 1990).

41. Nestle, F. O., Di Meglio, P., Qin, J.-Z. & Nickoloff, B. J. Skin immune sentinels in health and disease. *Nat. Rev. Immunol.* **9**, 679–691 (2009).

42. Höfer, T. *et al.* Animal testing and alternative approaches for the human health risk assessment under the proposed new European chemicals regulation. *Arch. Toxicol.* **78**, 549–564 (2004).

43. Basketter, D. A., Whittle, E. & Chamberlain, M. Identification of irritation and corrosion hazards to skin: an alternative strategy to animal testing. *Food Chem. Toxicol.* **32**, 539–542 (1994).

44. Woodland, R. European Regulatory Requirements for Veterinary Vaccine Safety and Potency Testing and Recent Progress Towards Reducing Animal Use. *Procedia Vaccinol.* **5**, 151–155 (2011).

45. Daneshian, M. A framework program for the teaching of alternative methods (replacement, reduction, refinement) to animal experimentation. *ALTEX* **28**, 341–352 (2011).

46. MacArthur Clark, J. The 3Rs in research: a contemporary approach to replacement, reduction and refinement. *Br. J. Nutr.* **120**, S1–S7 (2018).

47. Benavides, F., Oberyszyn, T. M., VanBuskirk, A. M., Reeve, V. E. & Kusewitt, D. F. The hairless mouse in skin research. *J. Dermatol. Sci.* **53**, 10–18 (2009).

48. Gudjonsson, J. E., Johnston, A., Dyson, M., Valdimarsson, H. & Elder, J. T. Mouse Models of Psoriasis. *J. Invest. Dermatol.* **127**, 1292–1308 (2007).

49. van der Fits, L. *et al.* Imiquimod-Induced Psoriasis-Like Skin Inflammation in Mice Is Mediated via the IL-23/IL-17 Axis. *J. Immunol.* **182**, 5836–5845 (2009).

50. Man, M.-Q. *et al.* Characterization of a Hapten-Induced, Murine Model with Multiple Features of Atopic Dermatitis: Structural, Immunologic, and Biochemical Changes following Single Versus Multiple Oxazolone Challenges. *J. Invest. Dermatol.* **128**, 79–86 (2008).

51. Kiebert, G. *et al.* Atopic dermatitis is associated with a decrement in health-related quality of life. *Int. J. Dermatol.* **41**, 151–158 (2002).

52. Lewis-Jones, S. Quality of life and childhood atopic dermatitis: the misery of living with childhood eczema: ATOPIC ECZEMA/QUALITY OF LIFE. *Int. J. Clin. Pract.* **60**, 984–992 (2006).

53. Krueger, G. *et al.* The impact of psoriasis on quality of life: results of a 1998 National Psoriasis Foundation patient-membership survey. *Arch. Dermatol.* **137**, 280–284 (2001).

54. Langley, R. G. B. Psoriasis: epidemiology, clinical features, and quality of life. *Ann. Rheum. Dis.* **64**, ii18–ii23 (2005).

55. Leung, D. Y. M., Boguniewicz, M., Howell, M. D., Nomura, I. & Hamid, Q. A. New insights into atopic dermatitis. *J. Clin. Invest.* **113**, 651–657 (2004).

56. Jungersted, J. M. *et al.* Stratum corneum lipids, skin barrier function and filaggrin mutations in patients with atopic eczema: Filaggrin mutations, skin barrier and lipids. *Allergy* **65**, 911–918 (2010).

57. Proksch, E., Fölster-Holst, R. & Jensen, J.-M. Skin barrier function, epidermal proliferation and differentiation in eczema. *J. Dermatol. Sci.* **43**, 159–169 (2006).

58. Hudson, T. J. Skin barrier function and allergic risk. *Nat. Genet.* **38**, 399–400 (2006).

59. Pastore, S., Mascia, F., Giustizieri, M. L., Giannetti, A. & Girolomoni, G. Pathogenetic mechanisms of atopic dermatitis. *Arch. Immunol. Ther. Exp. (Warsz.)* **48**, 497–504 (2000).

60. Kay, A. B. Allergy and Allergic Diseases. *N. Engl. J. Med.* **344**, 30–37 (2001).

61. Dold, S., Wjst, M., von Mutius, E., Reitmeir, P. & Stiepel, E. Genetic risk for asthma, allergic rhinitis, and atopic dermatitis. *Arch. Dis. Child.* **67**, 1018–1022 (1992).

62. Weidinger, S. *et al.* Loss-of-function variations within the filaggrin gene predispose for atopic dermatitis with allergic sensitizations. *J. Allergy Clin. Immunol.* **118**, 214–219 (2006).

63. *Management of Atopic Dermatitis*. vol. 1027 (Springer International Publishing, 2017).

64. Novak, N. Immune mechanisms leading to atopic dermatitis. *J. Allergy Clin. Immunol.* **112**, S128–S139 (2003).

65. Novak, N. & Bieber, T. Allergic and nonallergic forms of atopic diseases. *J. Allergy Clin. Immunol.* **112**, 252–262 (2003).

66. Akdis, C. A. & Akdis, M. Immunological differences between intrinsic and extrinsic types of atopic dermatitis. *Clin. Htmlent Glyphamp Asciiamp Exp. Allergy* **33**, 1618–1621 (2003).

67. Raychaudhuri, S. & Farber, E. The prevalence of psoriasis in the world. *J. Eur. Acad. Dermatol. Venereol.* **15**, 16–17 (2001).

68. Lima, X. T., Minnillo, R., Spencer, J. M. & Kimball, A. B. Psoriasis prevalence among the 2009 AAD National Melanoma/Skin Cancer Screening Program participants: An approach to assessing the epidemiology of skin diseases. *J. Eur. Acad. Dermatol. Venereol.* **27**, 680–685 (2013).

69. Bowcock, A. M. & Krueger, J. G. Erratum: Getting under the skin: the immunogenetics of psoriasis. *Nat. Rev. Immunol.* **5**, 699–711 (2005).

70. Enamandram, M. & Kimball, A. B. Psoriasis Epidemiology: The Interplay of Genes and the Environment. *J. Invest. Dermatol.* **133**, 287–289 (2013).

71. Liu, Y., Krueger, J. G. & Bowcock, A. M. Psoriasis: genetic associations and immune system changes. *Genes Immun.* **8**, 1–12 (2007).

72. Christophers, E. Psoriasis - epidemiology and clinical spectrum. *Clin. Exp. Dermatol.* **26**, 314–320 (2001).

73. Lowes, M. A., Bowcock, A. M. & Krueger, J. G. Pathogenesis and therapy of psoriasis. *Nature* **445**, 866–873 (2007).

74. Lebwohl, M. & Ali, S. Treatment of psoriasis. Part 1. Topical therapy and phototherapy. *J. Am. Acad. Dermatol.* **45**, 487–502 (2001).

75. Koo, J., Nguyen & Koo, J. Etanercept in the treatment of plaque psoriasis. *Clin. Cosmet. Investig. Dermatol.* 77 (2009) doi:10.2147/CCID.S3412.

76. Krueger, J. G. Successful ultraviolet B treatment of psoriasis is accompanied by a reversal of keratinocyte pathology and by selective depletion of intraepidermal T cells. *J. Exp. Med.* **182**, 2057–2068 (1995).

77. Marchiori, M. L. *et al.* Hydrogel containing dexamethasone-loaded nanocapsules for cutaneous administration: preparation, characterization, and in vitro drug release study. *Drug Dev. Ind. Pharm.* **36**, 962–971 (2010).

78. Yoder, M. C., Chua, R. & Tepper, R. Effect of Dexamethasone on Pulmonary Inflammation and Pulmonary Function of Ventilator-dependent Infants with Bronchopulmonary Dysplasia. *Am. Rev. Respir. Dis.* **143**, 1044–1048 (1991).

79. Loftsson, T., Hreinsdóttir, D. & Stefánsson, E. Cyclodextrin microparticles for drug delivery to the posterior segment of the eye: aqueous dexamethasone eye drops. *J. Pharm. Pharmacol.* **59**, 629–635 (2007).

80. PubChem [Internet]. Bethesda (MD): National Library of Medicine (US), National Center for Biotechnology Information; 2004-. PubChem Annotation Record for DEXAMETHASONE, Source: Hazardous Substances Data Bank (HSDB); [cited 2021 June 28]. Available from: https://pubchem.ncbi.nlm.nih.gov/source/hsdb/3053.

81. Dexamethasone. *PubChem Compd. Database* doi:CID=5743.

82. Ruzicka, T. *et al.* A Short-Term Trial of Tacrolimus Ointment for Atopic Dermatitis. *N. Engl. J. Med.* **337**, 816–821 (1997).

83. Paller, A., Eichenfield, L. F., Leung, D. Y. M., Stewart, D. & Appell, M. A 12-week study of tacrolimus ointment for the treatment of atopic dermatitis in pediatric patients. *J. Am. Acad. Dermatol.* **44**, S47–S57 (2001).

84. Wallemacq, P. E. & Reding, R. FK506 (tacrolimus), a novel immunosuppressant in organ transplantation: clinical, biomedical, and analytical aspects. *Clin. Chem.* **39**, 2219–2228 (1993).

85. Tacrolimus. *PubChem Compd. Database* doi:CID=5282315.

86. PubChem [Internet]. Bethesda (MD): National Library of Medicine (US), National Center for Biotechnology Information; 2004-. PubChem Annotation Record for

Tacrolimus, Source: Hazardous Substances Data Bank (HSDB); [cited 2021 June 28]. Available from: https://pubchem.ncbi.nlm.nih.gov/source/hsdb/8195.

87. PerkinElmer. ChemDraw Professional.

88. Mura, S., Nicolas, J. & Couvreur, P. Stimuli-responsive nanocarriers for drug delivery. *Nat. Mater.* **12**, 991–1003 (2013).

89. Yamamoto, K. *et al.* Core-multishell nanocarriers: Transport and release of dexamethasone probed by soft X-ray spectromicroscopy. *J. Controlled Release* **242**, 64–70 (2016).

90. Haag, R. Supramolecular Drug-Delivery Systems Based on Polymeric Core–Shell Architectures. *Angew. Chem. Int. Ed.* **43**, 278–282 (2004).

91. Hönzke, S. *et al.* Tailored dendritic core-multishell nanocarriers for efficient dermal drug delivery: A systematic top-down approach from synthesis to preclinical testing. *J. Controlled Release* **242**, 50–63 (2016).

92. Stefani, S. *et al.* Triglycerol-based hyperbranched polyesters with an amphiphilic branched shell as novel biodegradable drug delivery systems. *Polym. Chem.* **7**, 887–898 (2016).

93. Lapteva, M., Mondon, K., Möller, M., Gurny, R. & Kalia, Y. N. Polymeric Micelle Nanocarriers for the Cutaneous Delivery of Tacrolimus: A Targeted Approach for the Treatment of Psoriasis. *Mol. Pharm.* **11**, 2989–3001 (2014).

94. Kabanov, A. V. & Vinogradov, S. V. Nanogels as Pharmaceutical Carriers: Finite Networks of Infinite Capabilities. *Angew. Chem. Int. Ed.* **48**, 5418–5429 (2009).

95. Williams, A. C. & Barry, B. W. Penetration enhancers. *Adv. Drug Deliv. Rev.* **56**, 603–618 (2004).

96. Behl, C. R. *et al.* Hydration and Percutaneous Absorption: I. Influence of Hydration on Alkanol Permeation Through Hairless Mouse Skin. *J. Invest. Dermatol.* **75**, 346–352 (1980).

97. Giulbudagian, M. *et al.* Correlation between the chemical composition of thermoresponsive nanogels and their interaction with the skin barrier. *J. Controlled Release* **243**, 323–332 (2016).

98. Stöhr, J. *NEXAFS Spectroscopy*. (Springer Berlin Heidelberg, 1992).

99. Henke, B. L., Lee, P., Tanaka, T. J., Shimabukuro, R. L. & Fujikawa, B. K. Low-energy x-ray interaction coefficients: Photoabsorption, scattering, and reflection. *At. Data Nucl. Data Tables* **27**, 1–144 (1982).

100. Coulson, C. A. & Longuet-Higgins, H. C. The Electronic Structure of Conjugated Systems. I. General Theory. *Proc. R. Soc. Math. Phys. Eng. Sci.* **191**, 39–60 (1947).

101. Longuet-Higgins, H. C. Some Studies in Molecular Orbital Theory III. Substitution in Aromatic and Heteroaromatic Systems. *J. Chem. Phys.* **18**, 283–291 (1950).

102. Glen, G. L. & Dodd, C. G. Use of Molecular Orbital Theory to Interpret X-Ray *K* -Absorption Spectral Data. *J. Appl. Phys.* **39**, 5372–5377 (1968).

103. Ade, H. & Hitchcock, A. P. NEXAFS microscopy and resonant scattering: Composition and orientation probed in real and reciprocal space. *Polymer* **49**, 643–675 (2008).

104. Hitchcock, A. P. & Brion, C. E. Inner-shell excitation of formaldehyde, acetaldehyde and acetone studied by electron impact. *J. Electron Spectrosc. Relat. Phenom.* **19**, 231–250 (1980).

105. Wight, G. R. & Brion, C. E. K-shell excitation of CH4, NH3, H2O, CH3OH, CH3OCH3 and CH3NH2 by 2.5 keV electron impact. *J. Electron Spectrosc. Relat. Phenom.* **4**, 25–42 (1974).

106. Francis, J. T. & Hitchcock, A. P. Inner-shell spectroscopy of p-benzoquinone, hydroquinone, and phenol: distinguishing quinoid and benzenoid structures. *J. Phys. Chem.* **96**, 6598–6610 (1992).

107. Ohigashi, T. *et al.* Construction of the Scanning Transmission X-ray Microscope Beamline at UVSOR. *J. Phys. Conf. Ser.* **463**, 012006 (2013).

108. Raabe, J. *et al.* PolLux: A new facility for soft x-ray spectromicroscopy at the Swiss Light Source. *Rev. Sci. Instrum.* **79**, 113704 (2008).

109. Kilcoyne, A. L. D. *et al.* Interferometer-controlled scanning transmission X-ray microscopes at the Advanced Light Source. *J. Synchrotron Radiat.* **10**, 125–136 (2003).

110. Fakra, S. Scintillator Detectors for Scanning Transmission X-ray Microscopes at the Advanced Light Source. in vol. 705 973–976 (AIP, 2004).

111. https://stanfordcomputeroptics.com/technology/image-intensifier/phosphor-screen.html, 28.06.2021, P43 decay time.

112. Storm, L. & Israel, H. I. Photon cross sections from 1 keV to 100 MeV for elements Z=1 to Z=100. *At. Data Nucl. Data Tables* **7**, 565–681 (1970).

113. Williams, S. *et al.* Measurements of wet metaphase chromosomes in the scanning transmission X-ray microscope. *J. Microsc.* **170**, 155–165 (1993).

114. Beetz, T. & Jacobsen, C. Soft X-ray radiation-damage studies in PMMA using a cryo-STXM. *J. Synchrotron Radiat.* **10**, 280–283 (2003).

115. *http://www.chemspider.com/Chemical-Structure.5541.html (accessed 15:34, Jul 26, 2017).*

116. Schuster, K. C., Urlaub, E. & Gapes, J. R. Single-cell analysis of bacteria by Raman microscopy: spectral information on the chemical composition of cells and on the heterogeneity in a culture. *J. Microbiol. Methods* **42**, 29–38 (2000).

117. J. Qin, K. Chao, & M. S. Kim. Raman Chemical Imaging System for Food Safety and Quality Inspection. *Trans. ASABE* **53**, 1873–1882 (2010).

118. Lohumi, S., Kim, M. S., Qin, J. & Cho, B.-K. Raman imaging from microscopy to macroscopy: Quality and safety control of biological materials. *TrAC Trends Anal. Chem.* **93**, 183–198 (2017).

119. Marigheto, N. A., Kemsley, E. K., Potter, J., Belton, P. S. & Wilson, R. H. Effects of sample heating in FT-Raman spectra of biological materials. *Spectrochim. Acta. A. Mol. Biomol. Spectrosc.* **52**, 1571–1579 (1996).

120. Evans, C. L. & Xie, X. S. Coherent Anti-Stokes Raman Scattering Microscopy: Chemical Imaging for Biology and Medicine. *Annu. Rev. Anal. Chem.* **1**, 883–909 (2008).

121. Huff, T. B. & Cheng, J.-X. In vivo coherent anti-Stokes Raman scattering imaging of sciatic nerve tissue. *J. Microsc.* **225**, 175–182 (2007).

122. Li, L., Wang, H. & Cheng, J.-X. Quantitative Coherent Anti-Stokes Raman Scattering Imaging of Lipid Distribution in Coexisting Domains. *Biophys. J.* **89**, 3480–3490 (2005).

123. Freudiger, C. W. *et al.* Label-Free Biomedical Imaging with High Sensitivity by Stimulated Raman Scattering Microscopy. *Science* **322**, 1857–1861 (2008).

124. G.J. Woodbury & W.R. Ng. Stimulated Raman emission in a normal ruby laser. *Proc IRE* **50**, 2367 (1962).

125. Saar, B. G. *et al.* Video-Rate Molecular Imaging in Vivo with Stimulated Raman Scattering. *Science* **330**, 1368–1370 (2010).

126. Wayne, R. O. *Light and Video Microscopy*. (Elsevier Science & Technology, 2019).

127. Burch, C. R. & Stock, J. P. P. Phase-Contrast Microscopy. *J. Sci. Instrum.* **19**, 71–75 (1942).

128. Lichtman, J. W. & Conchello, J.-A. Fluorescence microscopy. *Nat. Methods* **2**, 910–919 (2005).

129. Schultz, R. A. *et al.* Hyperspectral imaging: a novel approach for microscopic analysis. *Cytometry* **43**, 239–247 (2001).

130. World Medical Association Declaration of Helsinki: Ethical Principles for Medical Research Involving Human Subjects. *JAMA* **310**, 2191 (2013).

131. van der Molen, R. G. *et al.* Tape stripping of human stratum corneum yields cell layers that originate from various depths because of furrows in the skin. *Arch. Dermatol. Res.* **289**, 514–518 (1997).

132. Pegoraro, C., MacNeil, S. & Battaglia, G. Transdermal drug delivery: from micro to nano. *Nanoscale* **4**, 1881 (2012).

133. Hoffman, A. S. The origins and evolution of "controlled" drug delivery systems. *J. Controlled Release* **132**, 153–163 (2008).

134. Giulbudagian, M. *et al.* Correlation between the chemical composition of thermoresponsive nanogels and their interaction with the skin barrier. *J. Controlled Release* **243**, 323–332 (2016).

135. Gerecke, C. *et al.* Biocompatibility and characterization of polyglycerol-based thermoresponsive nanogels designed as novel drug-delivery systems and their intracellular localization in keratinocytes. *Nanotoxicology* **11**, 267–277 (2017).

136. Warner, R. R., Stone, K. J. & Boissy, Y. L. Hydration Disrupts Human Stratum Corneum Ultrastructure. *J. Invest. Dermatol.* **120**, 275–284 (2003).

137. Germer, G. *et al.* Improved Skin Permeability after Topical Treatment with Serine Protease: Probing the Penetration of Rapamycin by Scanning Transmission X-ray Microscopy. *ACS Omega* **6**, 12213–12222 (2021).

138. Lu, F.-K. *et al.* Label-free DNA imaging in vivo with stimulated Raman scattering microscopy. *Proc. Natl. Acad. Sci.* **112**, 11624–11629 (2015).

139. Ji, M. *et al.* Detection of human brain tumor infiltration with quantitative stimulated Raman scattering microscopy. *Sci. Transl. Med.* **7**, 309ra163-309ra163 (2015).

140. Nandakumar, P., Kovalev, A. & Volkmer, A. Vibrational imaging based on stimulated Raman scattering microscopy. *New J. Phys.* **11**, 033026 (2009).

141. Femtosecond time-resolved impulsive stimulated Raman spectroscopy using sub-7-fs pulses: Apparatus and applications. *Rev. Sci. Instrum.* **87**, 043107 (2016).

142. Klossek, A. *et al.* Studies for improved understanding of lipid distributions in human skin by combining stimulated and spontaneous Raman microscopy. *Eur. J. Pharm. Biopharm.* **116**, 76–84 (2017).

143. Elias, P. M. Epidermal Lipids, Barrier Function, and Desquamation. *J. Invest. Dermatol.* **80**, S44–S49 (1983).

144. Downing, D. T. *et al.* Skin Lipids: An Update. *J. Invest. Dermatol.* **88**, 2–6 (1987).

145. Bonté, F., Saunois, A., Pinguet, P. & Meybeck, A. Existence of a lipid gradient in the upper stratum corneum and its possible biological significance. *Arch. Dermatol. Res.* **289**, 78–82 (1997).

146. Elias, P. M. Lipids and the epidermal permeability barrier. *Arch. Dermatol. Res.* **270**, 95–117 (1981).

147. Kazarian, S. G. & Chan, K. L. A. Applications of ATR-FTIR spectroscopic imaging to biomedical samples. *Biochim. Biophys. Acta BBA - Biomembr.* **1758**, 858–867 (2006).

148. Benalcazar, W. A. & Boppart, S. A. Nonlinear interferometric vibrational imaging for fast label-free visualization of molecular domains in skin. *Anal. Bioanal. Chem.* **400**, 2817–2825 (2011).

149. Sherman, L., Ye, J. Y., Albert, O. & Norris, T. B. Adaptive correction of depth-induced aberrations in multiphoton scanning microscopy using a deformable mirror. *J. Microsc.* **206**, 65–71 (2002).

150. Matsumoto, N., Inoue, T., Matsumoto, A. & Okazaki, S. Correction of depth-induced spherical aberration for deep observation using two-photon excitation fluorescence microscopy with spatial light modulator. *Biomed. Opt. Express* **6**, 2575 (2015).

151. Wanjiku, B. *et al.* Qualifying X-ray and Stimulated Raman Spectromicroscopy for Mapping Cutaneous Drug Penetration. *Anal. Chem.* **91**, 7208–7214 (2019).

152. Schulz, R. *et al.* Data-based modeling of drug penetration relates human skin barrier function to the interplay of diffusivity and free-energy profiles. *Proc. Natl. Acad. Sci.* **114**, 3631–3636 (2017).

153. Rizi, K., Green, R. J., Donaldson, M. X. & Williams, A. C. Using pH Abnormalities in Diseased Skin to Trigger and Target Topical Therapy. *Pharm. Res.* **28**, 2589–2598 (2011).

Freie Universität Berlin

SELBSTSTÄNDIGKEITSERKLÄRUNG

gem. § 7 Abs. 4 der Promotionsordnung des Fachbereiches Biologie, Chemie, Pharmazie
basierend auf den Mitteilungen im Amtsblatt der Freien Universität Berlin
Nr. 52/2007 vom 04.09.2007, Nr. 04/2008 vom 07.02.2008 und Nr. 02/2012 vom 18.02.2012

Yamamoto	Kenji
Nachname Promovend*in	Vorname Promovend*in

Hierdurch versichere ich, dass ich meine Dissertation mit dem Titel

Label Free Spectromicroscopy on Drug and Drug Loaded Nanocarriers in Skin

selbstständig und ohne unerlaubte Hilfe angefertigt habe.

☒ Hierdurch versichere ich, dass meine Dissertation nicht auf meiner Diplom- oder Masterarbeit aufbaut bzw. nicht daraus erwachsen ist.

☐ Hierdurch versichere ich, dass meine Dissertation auf meiner Diplom- oder Masterarbeit mit folgendem Titel aufbaut bzw. daraus erwachsen ist:

☐ Hierdurch versichere ich, dass ich meine Dissertation (ganz oder in Teilen) nicht veröffentlicht habe.

☒ Hierdurch versichere ich, dass ich meine Dissertation im Einvernehmen mit meinem/meiner Betreuer*in Prof. Dr. Eckart Rühl (Name Betreuer*in) ganz oder in Teilen veröffentlicht habe.

↳Die 4 (Anzahl eintragen) Publikation/en

☒ sind Betandteil meiner kumulativen Dissertation.

☐ werden jedem Exemplar meiner Monographie als Ausdruck beigelegt.

Hierdurch versichere ich, dass ich meine Dissertation nicht schon einmal in einem anderen Promotionsverfahren eingereicht habe.

Datum

Unterschrift Promovend*in